JETP Letters, Vol. 77, No. 8, 2003, pp. 397–400. Translated from Pis'ma v Zhurnal Éksperimental'noĭ i Teoreticheskoĭ Fiziki, Vol. 77, No. 8, 2003, pp. 471–474.

Four-Wave Mixing in Hollow Photonic-Crystal Fibers

S. O. Konorov, A. B. Fedotov, and A. M. Zheltikov*

Physics Department, Moscow State University, Vorob'evy gory, Moscow, 119899, Russia

**e-mail: zheltikov@top.phys.msu.su*

Received March 11, 2003

A radical enhancement of four-wave mixing in hollow-core photonic-crystal fibers is experimentally demonstrated. An enhancement ratio of about 800 relative to the regime of tight focusing is achieved for the four-wave mixing process $3\omega = 2\omega + 2\omega - \omega$, where ω and 2ω are the frequencies of fundamental radiation and the second harmonic of picosecond Nd:YAG laser pulses. *© 2003 MAIK "Nauka/Interperiodica".*

PACS numbers: 42.65.Hw; 42.65.Wi; 42.81.Qb

Four-wave mixing (FWM) is one of the main classes of nonlinear-optical processes [1]. Interactions of this type are widely used for frequency conversion, control of ultrashort pulses, and spectroscopic applications. Waveguide regimes of laser-pulse propagation allow the efficiency of FWM processes to be substantially enhanced due to the radical increase in the length of nonlinear-optical interaction [2]. In particular, planar waveguides provide an unprecedented sensitivity level of coherent anti-Stokes Raman scattering (CARS), allowing the detection of the CARS signal from single molecules [3]. The sensitivity of FWM spectroscopy of the gas phase can be substantially improved through the use of hollow waveguides [4–6]. The magnitude of optical losses in air-guided modes of hollow fibers rapidly (as a^{-3}) increases with a decrease in the inner radius of the fiber a [7]. The FWM waveguide enhancement factor in hollow fibers (shown by curve *1* in Fig. 1) is thus physically limited, with its limiting value being determined by the fiber core radius.

Hollow-core fibers with a microstructure or photonic-crystal (two-dimensionally periodic) cladding [8] allow the level of optical losses to be radically reduced with respect to conventional hollow fibers. Air-guided modes in such fibers are supported due to the high reflectivity of the periodic structure in the fiber cladding within the spectral ranges corresponding to photonic band gaps [8, 9]. Hollow photonic-crystal fibers thus offer a unique opportunity of implementing highly efficient nonlinear-optical interactions of air-guided modes with transverse sizes of several microns (curves *2* and *3* in Fig. 1). Pioneering experimental studies into the nonlinear optics of microstructure fibers, carried out by Philip Russell's group at the University of Bath [10], have shown that such fibers allow the threshold of stimulated Raman scattering to be reduced to unprecedentedly low levels.

In this paper, we will experimentally demonstrate the radical enhancement of FWM in hollow photonic-crystal fibers. Using picosecond pulses of a Nd:YAG laser, we will investigate the FWM process $3\omega = 2\omega + 2\omega - \omega$, where ω and 2ω are the frequencies of fundamental radiation and the second harmonic of Nd:YAG laser radiation, and show that hollow photonic-crystal fibers provide an 800-fold enhancement of this nonlinear-optical process relative to the regime of tight focusing.

Our FWM experiments were performed with hollow-core photonic-crystal fibers having an inner diameter of about 14 μm and a period of the photonic-crystal cladding equal to 5 μm (insets in Fig. 2). These fibers were fabricated with the use of technology described in detail elsewhere [11]. Transmission spectra of our hol-

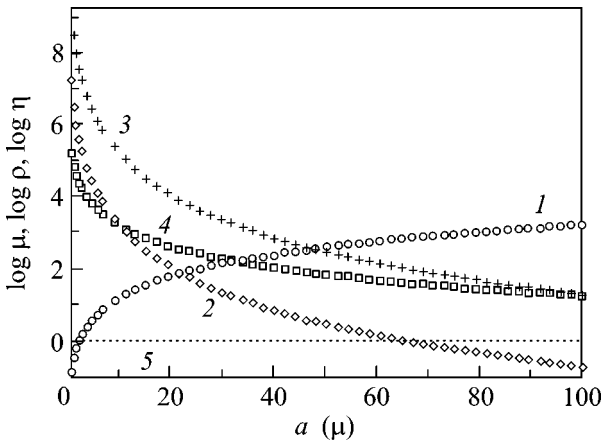

Fig. 1. Waveguide enhancement factors for four-wave mixing in (*1*) a standard hollow fiber with a solid cladding (ρ) and (*2*, *3*) a hollow microstructure fiber (μ) with an attenuation coefficient $\alpha = 0.1$ (*2*) and 0.01 cm^{-1} (*3*) as functions of the inner radius of the fiber a. (*4*) The figure of merit η for stimulated Raman scattering in a hollow microstructure fiber with an attenuation coefficient $\alpha = 0.01$ cm^{-1} as a function of the inner radius of the fiber a. Dotted line *5* corresponds to the efficiency of FWM in the regime of tight focusing. The radiation wavelength is 0.5 μm.

0021-3640/03/7708-0397$24.00

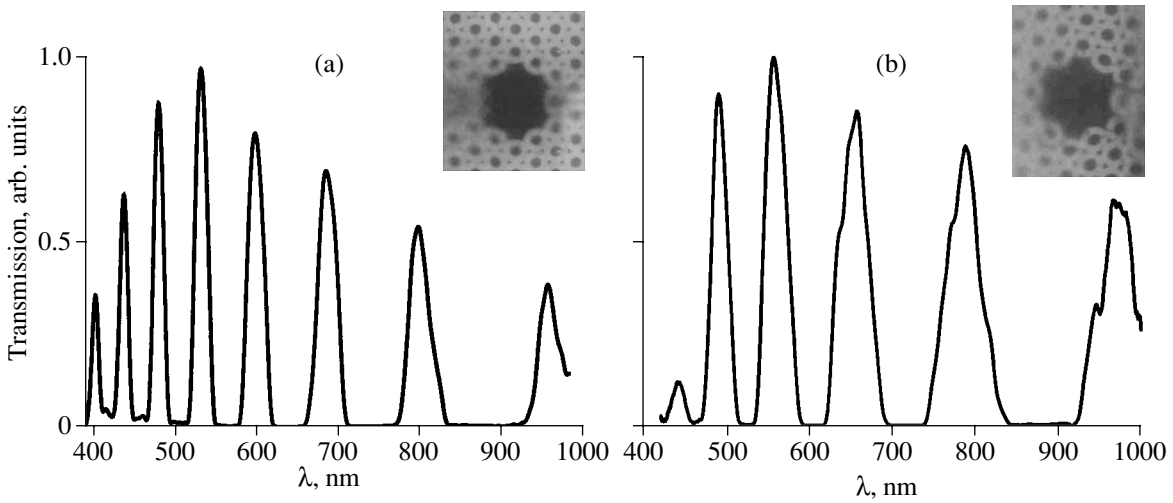

Fig. 2. Transmission spectra measured for hollow-core photonic-crystal fibers with different cross-section geometries (shown in the insets). The period of the structure in the cladding is about 5 μm.

low-core photonic crystal fibers displayed characteristic well-pronounced isolated peaks (Fig. 2). The origin of these peaks is associated with the high reflectivity of a periodically structured fiber cladding within photonic band gaps, which substantially reduces radiation losses in guided modes within narrow spectral ranges [8, 9]. Radiation with wavelengths lying away from photonic band gaps of the cladding leaks from the hollow core. Such leaky radiation modes are characterized by high losses, giving virtually no contribution to the signal at the output of the fiber. Since the peaks in transmission spectra of hollow-core photonic-crystal fibers are, in fact, maps of photonic band gaps of their two-dimensionally periodic cladding, the spectra of air-guided modes in such fibers can be tuned by changing the fiber cladding structure (Fig. 2). Hollow-core photonic-crystal fibers employed in our FWM experiments were designed in such a way as to provide maximum transmission simultaneously for the fundamental radiation of a Nd:YAG laser and for its second and third harmonics (the diagram of the FWM process, resulting in the generation of a signal at the frequency of the third harmonic, and the transmission spectrum of the fiber are shown in Fig. 3). The magnitude of optical losses was estimated as 0.09 cm^{-1} at a wavelength of 1.06 μm and 0.08 cm^{-1} at 0.532 μm for these fibers. The length of the fiber was chosen equal to 9 cm, slightly less than the length optimal for the FWM process, $l_{FWM} = \ln 3/\alpha$, where α is the coefficient of optical losses, which is assumed to be approximately the same for all the frequencies involved in the FWM process. The expected FWM waveguide enhancement ratio, as can be seen from Fig. 1, may be as high as 800–1000 under these conditions.

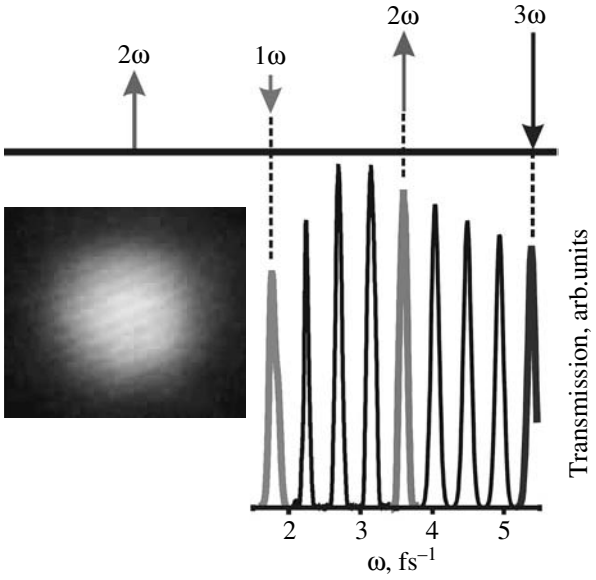

Fig. 3. Diagram of the four-wave mixing process $3\omega = 2\omega + 2\omega - \omega$ (top) and the transmission spectrum of a hollow-core photonic-crystal fiber designed to simultaneously transmit the two-color pump (at 1.06 and 0.53 μm) and the FWM signal (bottom). The inset shows the transverse intensity distribution of second-harmonic pump radiation in the air-guided mode of the hollow-core photonic-crystal fiber.

Our experimental setup was based on a picosecond laser system, which generated two-color pump radiation for the FWM process at wavelengths of 1.06 μm (pump radiation with frequency ω) and 0.53 μm (pump radiation with frequency 2ω). The picosecond laser included a passively mode-locked Nd:YAG master oscillator with negative-feedback-controlled cavity *Q* factor, a single-pulse selection unit, and amplifying stages [12]. Passive mode locking in the master oscilla-

tor was implemented with the use of a saturable absorber film, which was placed in front of the rear cavity mirror. Negative feedback was introduced by inserting an electro-optical switch controlled by a fast-response photomultiplier inside the cavity. A similar electro-optical switch was used to select a single pulse from the train of pulses produced by the master oscillator. The energy of a single 30-ps laser pulse thus selected ranged from 30 to 40 μJ. The single-pulse selection unit also served as an optical decoupler, suppressing the parasitic feedback between the amplifying stages and the master oscillator and preventing radiation reflected from optical elements of the amplification system from influencing the build-up of laser pulse trains in the master oscillator.

An amplified single pulse of 1.06-μm radiation is then used to generate the second harmonic in a DKDP crystal (Fig. 4). The second-harmonic signal is separated from the fundamental beam with a dichroic mirror. The optical path lengths of the fundamental and second-harmonic pulses were matched with the use of an optical delay line. These beams were then brought together on a dichroic mirror and were coupled into a hollow-core photonic-crystal fiber placed on a three-dimensional translation stage (Fig. 4). The signal at the frequency of the third harmonic of fundamental radiation, 3ω, can be produced in a hollow-core photonic-crystal fiber through both the $3\omega = 2\omega + 2\omega - \omega$ FWM process and direct third-harmonic generation $3\omega = \omega + \omega + \omega$. Experiments performed with only the fundamental beam used as a pump have shown, however, that direct third-harmonic generation is much less efficient than two-color FWM.

Linearly polarized fundamental and second-harmonic pulses of Nd:YAG laser radiation coupled into a hollow photonic-crystal fiber excited the fundamental waveguide modes. The inset to Fig. 3 shows a typical intensity distribution of second-harmonic pump radiation at the output of the fiber. The power of the FWM signal produced in a hollow photonic-crystal fiber was compared with the power of the FWM signal generated by tightly focused pump beams with the same wavelengths and the same energies. The FWM waveguide enhancement factor under the above-specified experimental conditions was estimated at approximately 800. This result qualitatively agrees with our theoretical analysis (cf. curves *2* and *5* in Fig. 1). The FWM waveguide enhancement factor is limited by optical losses of photonic-crystal fibers. We can expect, based on our calculations, that hollow-core photonic-crystal fibers with the magnitude of optical losses reduced down to 0.01 cm^{-1} could enhance FWM processes by more than four orders of magnitude relative to the regime of tightly focused pump beams (curve *3* in Fig. 1).

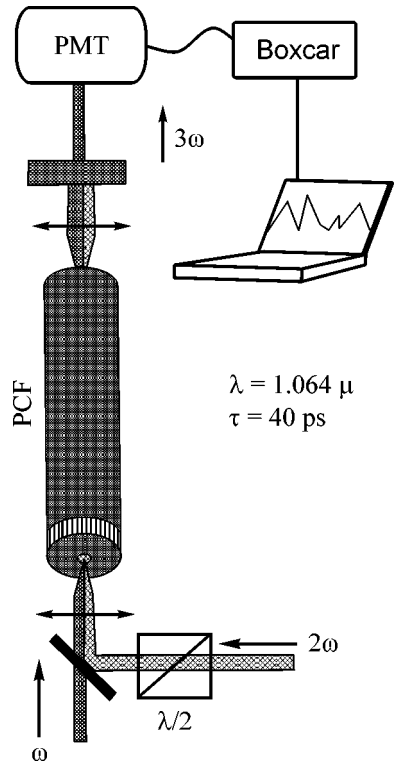

Fig. 4. Experimental setup for the investigation of four-wave mixing in a hollow-core photonic-crystal fiber.

The table compares the waveguide enhancement factor of the FWM process $3\omega = 2\omega + 2\omega - \omega$ attainable with a hollow-core photonic-crystal fiber with the waveguide enhancement achieved for the same FWM process in experiments with conventional, solid-cladding hollow fibers [13] using Nd:YAG laser pulses with the same durations (30 ps) and frequencies. This comparison shows that hollow-core photonic-crystal fibers employed in this work allow the FWM waveguide enhancement factor to be increased by a factor of more than 50 as compared with solid-cladding hollow fibers.

Waveguide enhancement of four-wave mixing

	a, μm	L, cm	μ	E_ω, μJ	$E_{2\omega}$, μJ
Solid-cladding hollow fiber [13]	100	10	15	10	10
Hollow fiber with a photonic-crystal cladding	13	9	800	2	2

Note: a is the inner diameter of a hollow fiber; L is the fiber length; μ is the waveguide FWM enhancement relative to the regime of tight focusing; E_ω and $E_{2\omega}$ are typical energies of the pump pulses with frequencies ω and 2ω generating a reliably detectable FWM signal.

The FWM signal can be reliably detected under conditions of experiments described in this paper with microjoule picosecond pump pulses, i.e., at the level of pump energies unprecedentedly low for off-resonance FWM in the gas phase.

The radical enhancement of FWM processes in hollow-core photonic-crystal fibers demonstrated by our experiments suggests new approaches for the nonlinear optics of high-power ultrashort laser pulses, high-field physics, and nonlinear spectroscopy. Hollow-core photonic-crystal fibers allow waveguide regimes of nonlinear-optical interactions to be implemented for high-power laser pulses that cannot be transmitted through standard fibers without irreversibly damaging these fibers. The group-velocity dispersion of gases filling the hollow core of photonic-crystal fibers is much lower than the group-velocity dispersion characteristic of waveguide modes in conventional fibers. Hollow photonic-crystal fibers with a small core radius thus hold much promise for the nonlinear-optical frequency conversion of ultrashort laser pulses and nonlinear spectroscopy with the use of such pulses. Due to their capability to substantially enhance nonlinear-optical processes and the possibility to tailor the dispersion of guided modes by changing the fiber structure, hollow photonic-crystal fibers are an attractive way to improve the efficiency of ultrashort-pulse synthesis through multiple Raman sideband generation, which was demonstrated recently with the use of solid-cladding hollow fibers [14]. Finally, the enhancement of FWM processes in hollow photonic-crystal fibers makes it possible to radically improve the sensitivity of nonlinear-optical spectroscopy of the gas phase and to loosen the requirements on the energies of laser pulses in nonlinear spectroscopy.

We are grateful to V.I. Beloglazov, N.B. Skibina, and A.V. Shcherbakov for fabricating microstructure fibers. Illuminating discussions with J.C. Knight, P.St.J. Russell, and D.A. Sidorov-Biryukov are gratefully acknowledged. This study was supported in part by the President of Russian Federation Grant no. 00-15-99304, the Russian Foundation for Basic Research (project nos. 03-02-16929 and 02-02-17098), the Volkswagen Foundation (project I/76 869), and the European Research Office of the US Army (Contract No. N62558-02-M-6023).

REFERENCES

1. Y. R. Shen, *The Principles of Nonlinear Optics* (Wiley, New York, 1984; Nauka, Moscow, 1989).
2. G. P. Agrawal, *Nonlinear Fiber Optics* (Academic, Boston, 1989; Mir, Moscow, 1996).
3. J. S. Kanger, C. Otto, and J. Greve, Appl. Spectrosc. **49**, 1326 (1995).
4. R. B. Miles, G. Laufer, and G. C. Bjorklund, Appl. Phys. Lett. **30**, 417 (1977).
5. A. B. Fedotov, F. Giammanco, A. N. Naumov, *et al.*, Appl. Phys. B **72**, 575 (2001).
6. A. M. Zheltikov, Usp. Fiz. Nauk **172**, 743 (2002) [Phys. Usp. **45**, 687 (2002)].
7. E. A. J. Marcatili and R. A. Schmeltzer, Bell Syst. Tech. J. **43**, 1783 (1964).
8. R. F. Cregan, B. J. Mangan, J. C. Knight, *et al.*, Science **285**, 1537 (1999).
9. S. O. Konorov, A. B. Fedotov, O. A. Kolevatova, *et al.*, Pis'ma Zh. Éksp. Teor. Fiz. **76**, 401 (2002) [JETP Lett. **76**, 341 (2002)].
10. F. Benabid, J. C. Knight, G. Antonopoulos, and P. St. J. Russell, Science **298**, 399 (2002).
11. S. O. Konorov, O. A. Kolevatova, A. B. Fedotov, *et al.*, Zh. Éksp. Teor. Fiz. **123**, 975 (2003) [JETP **96** (2003)] (in press).
12. A. M. Zheltikov, N. I. Koroteev, and A. B. Fedotov, Laser Phys. **4**, 569 (1994).
13. A. B. Fedotov, F. Giammanco, A. N. Naumov, *et al.*, Laser Phys. **11**, 515 (2001).
14. N. Zhavoronkov and G. Korn, Phys. Rev. Lett. **88**, 203901 (2002).

Translated by A. Zheltikov

JETP Letters, Vol. 77, No. 8, 2003, pp. 401–404. Translated from Pis'ma v Zhurnal Éksperimental'noĭ i Teoreticheskoĭ Fiziki, Vol. 77, No. 8, 2003, pp. 475–478.

Short-Range Magnetic Order in $LaMn(O_{1-x}F_x)_3$ from ^{139}La and ^{19}F NMR Data

K. N. Mikhalev[1], S. A. Lekomtsev[1], A. P. Gerashchenko[1], A. Yu. Yakubovskiĭ[2], and A. R. Kaul'[3]

[1] *Institute of Metal Physics, Ural Division, Russian Academy of Sciences, ul. S. Kovalevskoĭ 18, Yekaterinburg, 620219 Russia*

[2] *Russian Research Centre Kurchatov Institute, pl. Kurchatova 1, Moscow, 123182 Russia*

[3] *Moscow State University, Vorob'evy gory, Moscow, 119899 Russia*

Received March 3, 2003

The temperature behavior of the ^{139}La and ^{19}F NMR spectra was studied for polycrystalline $LaMn(O_{1-x}F_x)_3$ with a partial substitution of fluorine for oxygen. The temperature dependences of the ^{139}La and ^{19}F NMR line shapes were found to be substantially different. An appreciable broadening of the ^{19}F NMR spectrum and a fixed position of line maximum with lowering temperature is indicative of the presence of a short-range magnetic order in the paramagnetic temperature region ($T > T_N$). © *2003 MAIK "Nauka/Interperiodica".*

PACS numbers: 75.30.-m; 76.60.Lz

At present, $La_{1-x}A_xMnO_3$ manganites (A is a bivalent alkali-earth element) are being extensively studied in connection with the colossal magnetoresistance effect. The undoped $LaMnO_3$ compound is an A-type antiferromagnet with the orthorhombic P_{bnm} structure [1], in which, due to the presence of Mn^{3+} ions, the orbital ordering coexists with the Jahn–Teller distortions of MnO_6 octahedra [2]. It has recently been demonstrated [3] that the orbital order disappears at temperatures above 750 K, but the paramagnetic state is retained. This is not quite understood within the framework of the model suggested in [4], where it was assumed that ferromagnetic ordering is possible in weakly doped manganites in the absence of orbital ordering.

The strong interaction between the orbital, lattice, and spin degrees of freedom in manganites is the subject of wide discussion. One can expect that short-range magnetic order exists in the undoped manganite in the orbital-ordering region (140 K < T < 750 K). Indeed, an analysis of the ^{139}La NMR spectra of the ordered state indicates that the induced hyperfine field at the site of the lanthanum nucleus is H_{int} = 3.5 kOe [5], while H_{int} = 3.2 kOe in the paramagnetic region [6]. These values are very close to each other, strongly arguing for the short-range magnetic order in the undoped manganite in the paramagnetic region; otherwise, the hyperfine fields would differ by a value corresponding to the dipolar contribution (~0.7 kOe). The NMR probe at the oxygen sites is highly attractive for studying the local features of this phenomenon. In this work, we report the results of ^{19}F and ^{139}La NMR studies of a sample of fluorinated $LaMn(O_{1-x}F_x)_3$ manganite with $x \sim 0.06$.

To synthesize a ceramic sample of $LaMnO_3$, solutions of $La(NO_3)_3$ and $Mn(NO_3)_2$ nitrates were mixed in a given proportion, ashless filters were impregnated with the resulting solution, dried, and burned out. The residue was calcined for 2 h at 700°C, then ground to powder and pressed into pellets. Samples were sintered first at 1200°C for 12 h and then at 1400°C for 14 h. The oxygen concentration was determined by the iodometric method [7]. The fluorination of $LaMnO_3$ was performed at 250° for 15 h in a nitrogen atmosphere in a copper vial with a fixed amount of XeF_2. X-ray certification showed that the sample was single-phase. The fluorine concentration was determined by the potentiometric method with a LaF_3 electrode [8]. The resulting fluorine concentration in $LaMn(O_{1-x}F_x)_3$ was found to be $x = 0.06(1)$.

The EPR data indicate the presence of Mn^{2+} ions in the fluorinated sample. NMR measurements of the transverse relaxation times for the ^{19}F and ^{139}La nuclei showed that the temperature behavior of this quantity is similar for both of them in the paramagnetic region. These measurements unambiguously evidence the presence of fluorine ions in the oxygen sublattice of the fluorinated manganite.

The ^{139}La and ^{19}F NMR spectra were recorded in fields of 9.123 and 2.1139 T, respectively, on a pulsed phase-coherence NMR spectrometer using a $\pi/2$–τ–$\pi/2$-echo pulse sequence and the Fourier transform of a half of echo signal. The common spectrum was obtained by tuning the transceiving line with a discrete frequency step and summation of the individual Fourier subspectra.

A typical ^{139}La NMR spectrum of the sample studied is shown in Fig. 1. Taking into account the interac-

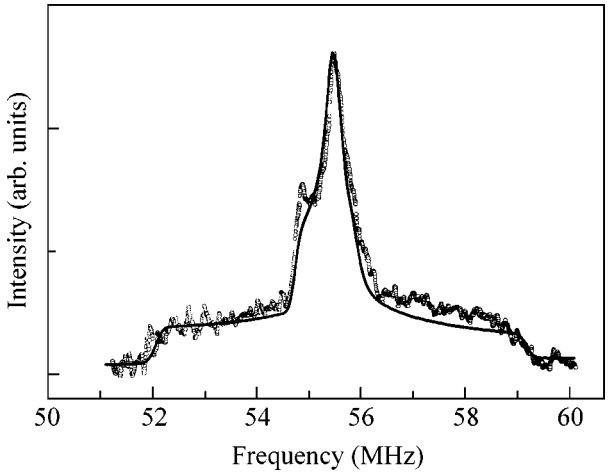

Fig. 1. ^{139}La NMR spectra recorded for $LaMn(O_{1-x}F_x)_3$ at room temperature in the magnetic field H_0 = 9.123 T. The calculated line shape is shown by the solid curve.

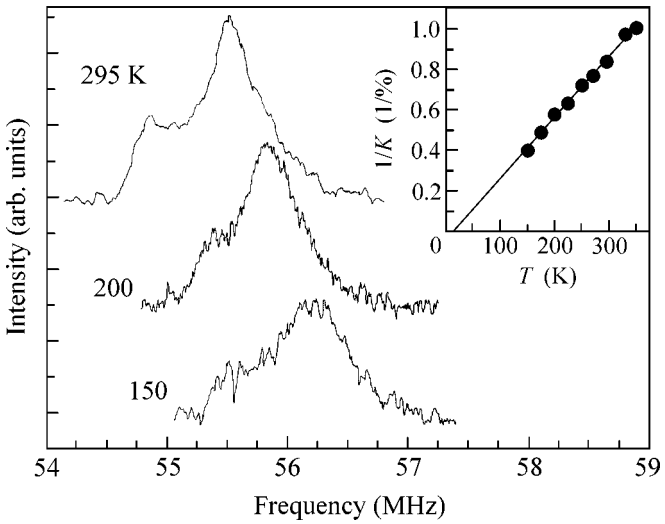

Fig. 2. Typical ^{139}La NMR spectra (central 1/2 ⟷ –1/2 transition) in an external field of 9.123 T for various temperatures. The temperature dependence of the inverse of isotropic NMR line shift 1/*K* is shown in the inset.

tion of the ^{139}La (I = 7/2) quadrupole moment with the electric field gradient (EFG) [9], one can expect seven lines in the NMR spectrum. Three of them—the central transition (1/2 ⟷ –1/2) and two satellite lines (3/2 ⟷ 1/2 and –3/2 ⟷ –1/2)—are shown in Fig. 1. The characteristic flat shape of the satellite lines (without well-defined sharp maxima) is evidence that the EFG asymmetry parameter $\eta = (V_{XX} - V_{YY})/V_{ZZ}$ is large (V_{XX}, V_{YY}, and V_{ZZ} are the EFG tensor components). The calculation of the ^{139}La line shape with allowance for the interaction between the nuclear quadrupole moment and the EFG in the second order of the perturbation theory and for the magnetic hyperfine interaction in the first order of the perturbation theory showed (Fig. 1) that the quadrupole frequency ν_Q = 3.7(4) and the asymmetry parameter η = 0.92(4) are very close to the data obtained for the undoped $LaMnO_3$ [5, 6, 10]. The line shift is isotropic ($K_X = K_Y = K_Z = K$), and its value at room temperature is close to the shift for $LaMnO_3$ [6].

It follows from these data that the fluorinated manganite is structurally and magnetically close to the undoped manganite and that the introduced fluorine atoms can be considered in the low-concentration approximation.

With lowering temperature, the maximum of the central ^{139}La NMR line undergoes a shift to higher frequencies (Fig. 2), while its width, which is mainly determined by the second-order quadrupolar effects, increases only slightly. An unusual decrease in the signal-to-noise ratio with lowering temperature is caused by a sizable shortening of the spin–spin relaxation time as the ordering temperature T_N = 140 K is approached. With lowering temperature, the line shift increases following the Curie–Weiss law and reproduces the behavior of the static magnetic susceptibility χ, $K = (\chi H_{\text{int}})/\mu_B$, similarly to the behavior described previously for $LaMnO_3$ [6, 11].

The ^{19}F NMR spectra are shown in Fig. 3. The line width strongly increases with lowering temperature, but the line maximum does not change its position (inset in Fig. 3), although one would expect that the

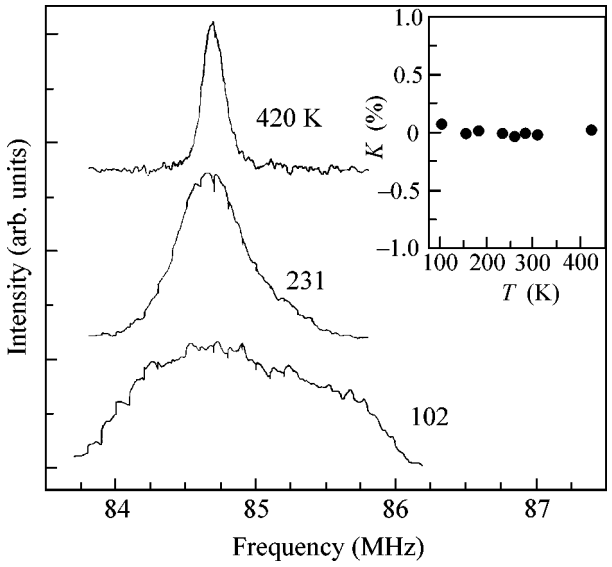

Fig. 3. ^{19}F NMR spectra recorded for $LaMn(O_{1-x}F_x)_3$ at various temperatures in the magnetic field H_0 = 2.1139 T. The temperature dependence of the shift of line maximum *K* is shown in the inset.

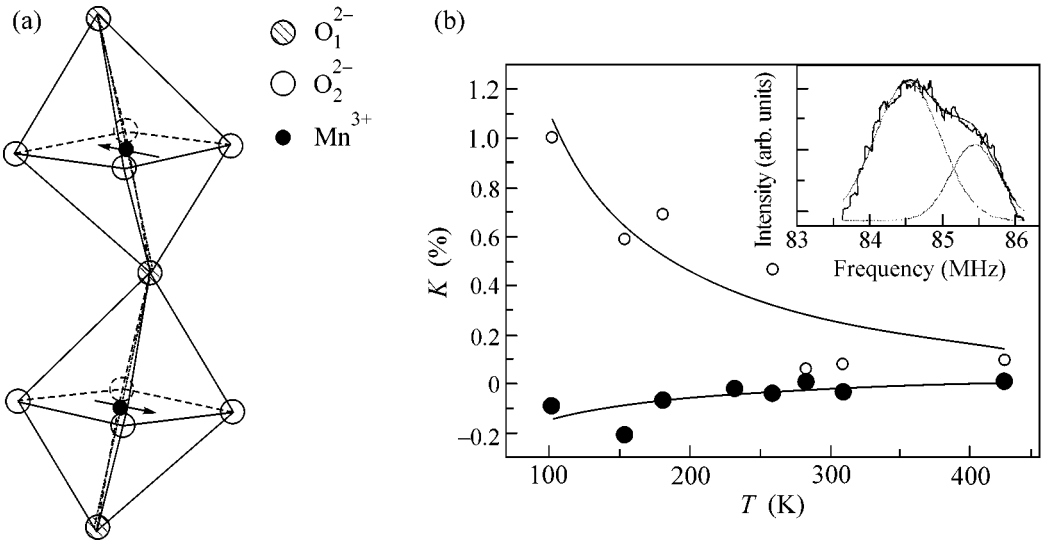

Fig. 4. (a) Schematic fragment of the $LaMnO_3$ structure. (b) Temperature dependences of the line shifts for the nonequivalent fluorine positions. A ^{19}F NMR spectrum (T = 102 K) obtained by the superposition of two Gaussian lines is shown in the inset.

temperature behavior in the paramagnetic temperature range is the same as for ^{139}La.

Such a sharp distinction between the behaviors of the lanthanum and fluorine lines can be explained in the following way. In the ordered state, one can expect the presence of two nonequivalent oxygen positions in $LaMnO_3$: two atoms occupy the vertices of the MnO_6 octahedron (O_1 in Fig. 4a) and are situated approximately mid between the planes with the oppositely directed spins, and four are situated almost in the *ab* plane (O_2 in Fig. 4a). Assume that fluorine occupies all oxygen positions with equal probability. At high temperatures (T > ~500 K), the exchange interaction is small compared to k_BT and the magnetic moments of two sublattices are aligned with an external magnetic field. As the temperature goes down, the exchange interaction becomes comparable to k_BT, as a result of which the ferromagnetic interaction between spins in the *ab* plane and the antiferromagnetic interaction along the *c* axis may establish short-range order in microclusters with sizes on the order of several lattice parameters. In this case, two lines would appear in the ^{19}F spectrum above the Néel temperature. Their maxima may shift in opposite directions as the temperature lowers, thereby broadening the overall NMR spectrum.

Similar behavior of the ^{19}F NMR spectrum was observed in an $RbNiF_3$ single crystal [12, 13], whose magnetic structure—the presence of two magnetic sublattices with the oppositely directed spins—is very close to our case. The fluorine NMR spectrum in that single crystal showed two lines, which shifted in opposite directions upon lowering temperature in the paramagnetic region, reflecting the behavior of local magnetizations for each of the magnetically nonequivalent fluorine positions.

In our case, the situation is more complicated; the MnO_6 octahedron is distorted, so that one can expect the presence of even three crystallographically nonequivalent oxygen positions. Moreover, the octahedron is turned about the (110) axis, and the atoms of O_2 oxygen are offset from the *ab* plane. At the same time, we deal with a polycrystalline sample, in which the crystallographic axes are randomly distributed. For these reasons, one should expect a much more complicated ^{19}F spectrum, rather than the two separate lines, as in [12, 13].

Nevertheless, we attempted to represent our experimental ^{19}F spectra as a superposition of two Gaussian lines (Fig. 4b). It turned out that the intensity ratio of these lines is close to two, in compliance with the previously suggested simple model. Moreover, the shift of the less intense line (O_1 position) exhibits exactly the same temperature dependence as the lanthanum shift in the same sample. This is in agreement with the fact that the lanthanum atoms in our manganite are situated between two planes with the oppositely directed spins, as also are the O_1 oxygen atoms.

Thus, it has been shown in this work that the anomalous evolution of the ^{19}F NMR line shape in the paramagnetic temperature range of the manganite sample considered can be due to the presence of a short-range order that coexists with the orbital ordering in this temperature range and precedes the transition to the antiferromagnetic state with long-range order.

We are grateful to S.V. Verkhovskiĭ for helpful discussion of results. This work was supported by the Russian Foundation for Basic Research, project nos. 99-02-16975 and 02-02-16357a.

REFERENCES

1. E. O. Wollan and W. C. Kochler, Phys. Rev. **100**, 545 (1955).
2. S. Ishihara, J. Inoue, and S. Maekawa, Phys. Rev. B **55**, 8280 (1997).
3. J. S. Zhou and J. B. Goodenough, Phys. Rev. B **60**, R15002 (1999).
4. L. P. Gor'kov and V. R. Kresin, Pis'ma Zh. Éksp. Teor. Fiz. **67**, 934 (1998) [JETP Lett. **67**, 985 (1998)].
5. A. Iwai, K. Kumagai, Y. Tomioka, *et al.*, Phys. Rev. B **59**, 97 (1999).
6. K. N. Mikhalev, A. P. Gerashchenko, S. A. Lekomtsev, *et al.*, Fiz. Met. Metalloved. **93**, 32 (2002).
7. I. G. Krogh Andersen, E. Krogh Andersen, P. Norby, *et al.*, J. Solid State Chem. **113**, 320 (1994).
8. M. S. Frant and J. W. Ross, Science **154**, 1553 (1966).
9. R. B. Creel, S. L. Segel, R. J. Schoenberger, *et al.*, J. Chem. Phys. **60**, 2310 (1974).
10. G. Allodi, M. Cesteli Guidi, R. De Renzi, *et al.*, Phys. Rev. Lett. **87**, 127206 (2001).
11. K. N. Mikhalev, S. A. Lekomtsev, A. P. Gerashchenko, *et al.*, Pis'ma Zh. Éksp. Teor. Fiz. **72**, 867 (2000) [JETP Lett. **72**, 599 (2000)].
12. G. A. Smolenskii, M. P. Petrov, V. V. Moskalev, *et al.*, Phys. Lett. A **25**, 519 (1967).
13. M. N. Petrov, V. V. Moskalev, and V. S. Kasperovich, Fiz. Tverd. Tela (Leningrad) **12**, 2063 (1970) [Sov. Phys. Solid State **12**, 1637 (1970)].

Translated by V. Sakun

JETP Letters, Vol. 77, No. 8, 2003, pp. 405–410. Translated from Pis'ma v Zhurnal Éksperimental'noĭ i Teoreticheskoĭ Fiziki, Vol. 77, No. 8, 2003, pp. 479–484.

Modeling of Electronic Density of States for Single-Wall Carbon and Boron Nitride Nanotubes

A. V. Osadchy*, E. D. Obraztsova, S. V. Terekhov, and V. Yu. Yurov

Research Center for Natural Sciences, General Physics Institute, Russian Academy of Sciences, Moscow, 119991 Russia

**e-mail: aosadchy@kapella.gpi.ru*

Received March 3, 2002

The electronic density of states is calculated for all possible geometric configurations of single-wall carbon and boron nitride nanotubes. The calculation is based on the numerical differentiation of the two-dimensional dispersion relations for graphite and hexagonal boron nitride. The differentiation is performed for all allowed values of the wave vector using the π-electron approximation. For the particular carbon nanotubes chosen as examples, a good agreement is demonstrated between the calculated values of energy spacing of the symmetric van Hove singularities in the density of states and the experimental data obtained from the resonance Raman scattering study. © *2003 MAIK "Nauka/Interperiodica".*

PACS numbers: 71.20.Tx; 78.30.Na

INTRODUCTION

The new nanostructured material called single-wall carbon nanotubes possesses many unique properties that attract the attention of researchers. A nanotube is a graphite monolayer rolled up so as to form a cylinder with a diameter of 10–20 Å [1]. The appearance of circular periodicity, which is a multiple of the cylinder circumference, gives rise to additional boundary conditions for the quantum dimension of the electronic states. As a result, the electronic density of states of single-wall carbon nanotubes radically differs from that of most other materials [2]. The electronic states in nanotubes have a pronounced peak structure, which can be experimentally observed by the methods of tunneling spectroscopy [3], optical absorption [4], and resonance Raman scattering [5–7]. The latter method allows one to obtain the data on the electronic structure of the material by observing the shift of the resonance response from one nanotube to another when the wavelength (energy) of the exciting laser radiation is varied. In this case, the diameters of the nanotubes involved in the resonance Raman scattering process are estimated from the frequencies of the corresponding "breathing" modes [5–7]. Each nanotube is characterized by one breathing mode, which represents radial vibrations of the nanotube as a whole.

For the determination of not only the diameter but also the chirality (the torsion angle) of a given nanotube from the Raman spectra, one needs data on the electronic density of states for this tube [6]. The data reported in the literature refer to few specific geometric configurations of carbon nanotubes [8–10] and hexagonal boron nitride (BN) nanotubes [11–14]. For nanotubes formed of other layered materials (MoS_2, WS_2, MgB_2 [15, 16]), data on the density of states are virtually absent.

In view of this situation, it was necessary to develop a computer program for calculating the electronic density of states for any type of single-wall carbon and BN nanotube. One of the requirements for the program was its generality; being partially modified, it should provide similar calculations for nanotubes formed of any layered material. The results obtained by calculating the parameters of electronic structure for particular carbon nanotubes were experimentally verified by resonance Raman scattering.

1. COMPUTATIONAL ALGORITHM FOR THE ELECTRONIC DENSITY OF STATES

1.1. Single-Wall Carbon Nanotubes

Dependences of the electronic density of states on energy for single-wall carbon nanotubes were calculated by numerically differentiating the dispersion relation for a graphite plane by the Monte Carlo method with allowance for the boundary conditions obtained for the plane rolled up into a nanosized cylinder. As a dispersion relation, we used the dependence [9]

$$E(\bar{K}) = \pm\gamma_0\left\{1 + 4\cos\left(\frac{\sqrt{3}K_x a_0}{2}\right)\right.$$
$$\left.\times\cos\left(\frac{K_y a_0}{2}\right) + 4\cos^2\left(\frac{K_y a_0}{2}\right)\right\}^{1/2}, \quad (1)$$

where K_x and K_y are the x and y components of the wave vector **K** with the origin at the center of the Brillouin

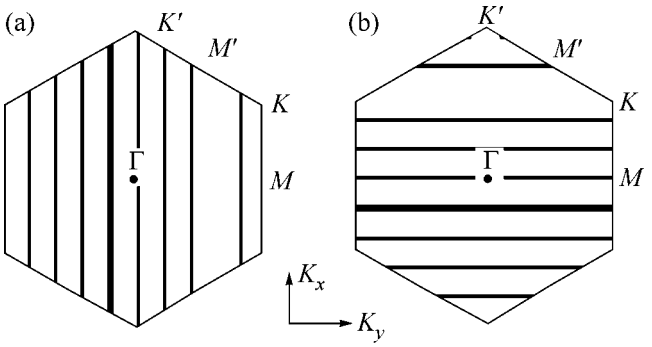

Fig. 1. Allowed values of the wave vector **K** for (a) (5,5) armchair nanotubes and (b) (9,0) zigzag nanotubes. The characteristic points of the Brillouin zone are denoted as *K*′, *M*′, *K*, and *M*.

zone, $\gamma_0 = 2.95$ eV is the overlap energy for the C–C bond, and $a_0 = 0.246$ nm is the graphite lattice constant.

The numerical differentiation should be performed for all allowed values of the wave vector within the first Brillouin zone. In the case of single-wall nanotubes, additional boundary conditions come into play. As a result, not all values of the wave vector **K** are allowed. Limitations appear because of rolling up the graphite plane into a cylinder with a diameter of about 10 Å; i.e., they are a consequence of the tube nanodimension.

The axes of the Cartesian coordinate system are chosen in such a way that the wave vector **K** is quantized along one axis and can take arbitrary continuous values along the other [8–10]. The direction of the quantized axis and the quantum size are different for different types of nanotubes. Hence, the resulting density of states widely varies for nanotubes of different geometry. Figure 1 shows the allowed values of the wave vector within the first Brillouin zone for (5,5) and (9,0) single-wall carbon nanotubes (Figs. 1a and 1b, respectively).

The allowed values of the wave vector are determined as follows [9]: we introduce a Cartesian coordinate system $X'Y'$, which has the origin at the point *K* of the first Brillouin zone and is rotated clockwise with respect to the initial coordinate system (Fig. 1) through an angle three times as great as the nanotube chirality angle. The latter is expressed as

$$\alpha = \arctan\left(\frac{\pi}{6} - \frac{1}{\sqrt{3}}\frac{n-m}{n+m}\right), \qquad (2)$$

where *n* and *m* are the nanotube parameters determining the width of the graphite plane strip and the way it is rolled up to form the nanotube (according to the adopted classification [1]).

In the new coordinate system $X'Y'$, the projection of the wave vector on the Y' axis takes any value, while the projection on the X' axis takes only the quantized values

$$K_{X'} = \frac{2}{3D}(3Q - n + m), \qquad (3)$$

where *Q* is an integer and *D* is the nanotube diameter in nanometers. The diameter of the nanotube as a function of its parameters *n* and *m* is expressed as

$$D = \frac{a_0}{\pi}\sqrt{n^2 + m^2 + nm}. \qquad (4)$$

By performing the inverse transformation of coordinates from the rotated coordinate system to the system used in Eq. (1), we obtain all allowed values of the wave vector **K**.

Using the formulas presented above, it is possible to perform the numerical differentiation of the dispersion relation with allowance for the boundary conditions. For the practical realization of the problem, we developed a computer program that provides the calculation of the density of states for any type of single-wall carbon nanotubes (the nanotube type should be preset before the calculation). The numerical differentiation was performed by the Monte Carlo method. Depending on the required accuracy of calculation, the execution time varied from 60 s to 1 h. The results of the calculation were entered into the Microcal Origin package.

1.2 Single-Wall Boron Nitride Nanotubes

Many materials that differ from carbon but have a layered structure (hexagonal BN, MoS_2, and WS_2) may exist in the form of nanotubes [14–16]. However, to date, single-wall nanotubes have been synthesized only from BN [14]. To understand their physical properties, one has to know their electronic structure. For this purpose, we modified our computer program so as to calculate the density of states for BN nanotubes.

We derived a formula describing the two-dimensional dispersion relation for hexagonal BN. In the literature [17], the dispersion curves were presented for some specific directions of the Brillouin zone. However, for the numerical differentiation, it is necessary to know the energy value for any allowed wave vector **K**. Hence, it is necessary to have a formula (analogous to Eq. (1)) that describes the dispersion relation for a two-dimensional sheet of hexagonal BN in the π-electron approximation. To obtain such a dependence, we performed the following calculations (similar to those used in [8] for the derivation of Eq. (1)). The Hamiltonian for a graphite plane has the form [9]

$$H = \begin{pmatrix} \varepsilon_{2p} & -\gamma_0 f(k) \\ -\gamma_0 f(k)^* & \varepsilon_{2p} \end{pmatrix},$$

$$f(k) = e^{ik_x a_0/\sqrt{3}} + 2e^{-ik_x a_0/2\sqrt{3}}\cos\frac{k_y a_0}{2},$$

where $a_0 = \sqrt{3}\,a_{c-c}$, a_{c-c} is the C–C bond length, and ε_{2p} is the $2p$ orbital energy. To derive Eq. (1), it was necessary to solve the equation $\det(H - ES) = 0$, where

$$S = \begin{pmatrix} 1 & sf(k) \\ sf(k)^* & 1 \end{pmatrix}$$

is the overlap integral matrix and E is the energy. To derive the desired formula for a BN plane, it is necessary to introduce some modifications. In the case of graphite, we deal with a single sort of atom, i.e., carbon. A boron nitride plane contains different sorts of atoms (boron and nitrogen). Therefore, the constants lying on the diagonal of the Hamiltonian H must be different; i.e., the Hamiltonian takes the form

$$H = \begin{pmatrix} \varepsilon_{2p1} & -\gamma_0 f(k) \\ -\gamma_0 f(k)^* & \varepsilon_{2p2} \end{pmatrix}, \quad (5)$$

where ε_{2p1} and ε_{2p2} are different constants. Performing the calculations similar to those in the derivation of Eq. (1) with the use of Hamiltonian (5), we arrive at the formula for the dispersion surface:

$$E(K_x, K_y) = \frac{\tilde{\varepsilon} \pm \sqrt{\tilde{\varepsilon}^2 + 4\tilde{\gamma}_0^2 \omega(K_x, K_y)}}{2},$$

$$\omega(K_x, K_y) = \left(1 + 4\cos\left(\frac{\sqrt{3}K_x\tilde{a}_0}{2}\right)\cos\left(\frac{K_y\tilde{a}_0}{2}\right) + 4\cos^2\left(\frac{K_y\tilde{a}_0}{2}\right)\right)^2, \quad (6)$$

where $\tilde{a}_0$, $\tilde{\gamma}_0$, and $\tilde{\varepsilon} \equiv \varepsilon_{2p1} - \varepsilon_{2p2}$ are constants.

To determine the constants, we used the dispersion curve given for crystalline hexagonal BN in [17]. The values of the constants were optimized to achieve the closest approximation to the dispersion curves for a π electron in the given directions. As a result, we obtained the values

$$\tilde{a}_0 = 0.249 \text{ nm}, \quad \tilde{\gamma}_0 = 2.85 \text{ eV}, \quad \tilde{\varepsilon} = 4.3 \text{ eV}.$$

The computer program described above was modified using dispersion relation (6) and applied for calculating the density of states of BN nanotubes of an arbitrary geometry. The selection rules for the allowed wave vectors were taken to be the same as in the case of carbon nanotubes.

A similar calculation can also be performed for nanotubes formed from other layered materials, on condition that the corresponding two-dimensional dispersion relation is preset.

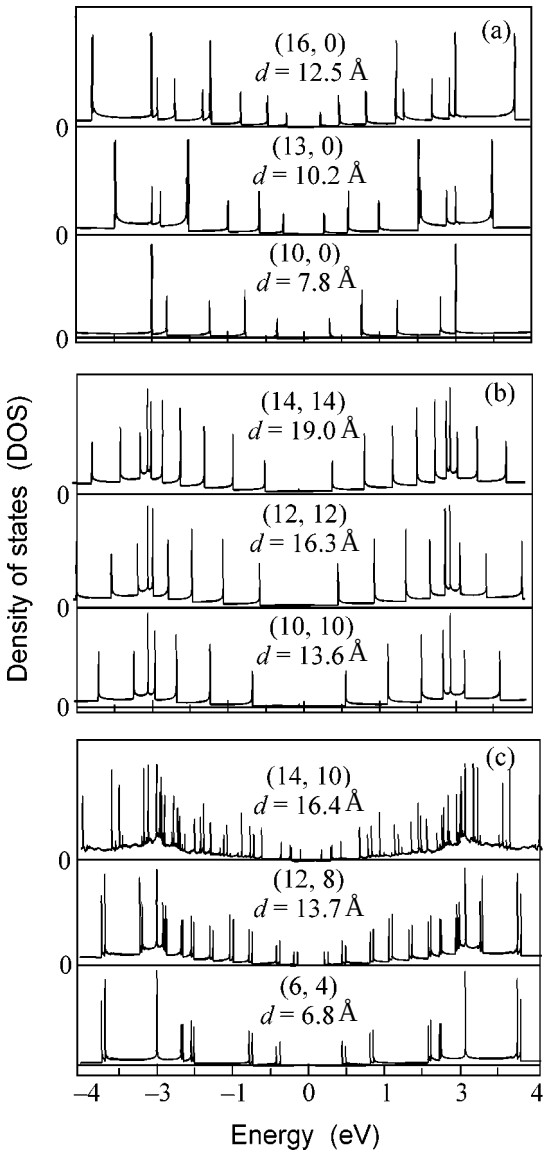

Fig. 2. Calculated densities of states for single-wall carbon nanotubes of different geometries. The plots demonstrate the monotonic dependence of the bandgap on the tube diameter for nanotubes of the (a) zigzag and (b) armchair types and (c) for nanotubes with an arbitrary chirality.

2. RESULTS

2.1. Modeling of the Electronic Density of States for Single-Wall Carbon Nanotubes of Different Geometry

Figure 2 presents the dependences of the density of states on the diameter for nanotubes of the zigzag (Fig. 2a) and armchair (Fig. 2b) types and for nanotubes with an arbitrary chirality (Fig. 2c). The dependences were obtained using the computer program described above. The energy spacings of the first, second, third, …, ith symmetric van Hove singularities [1] can by convention be considered as energy pseudogaps E_{11}, E_{22}, E_{33}, …, E_{ii} (Fig. 3). From Fig. 2, one can see

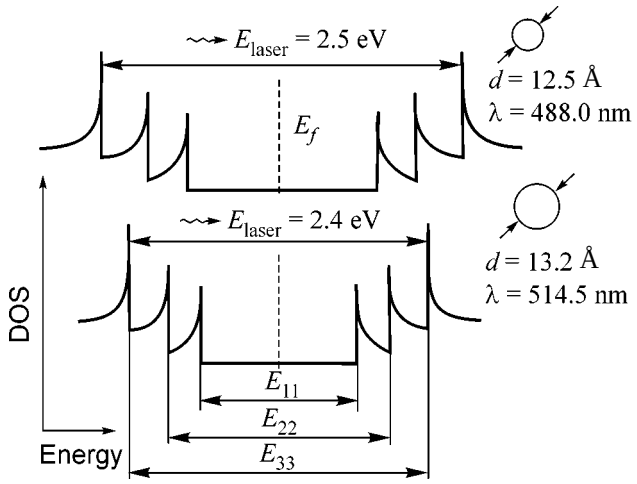

Fig. 3. Energy diagram illustrating the excitation of the resonance Raman scattering for nanotubes with different diameters; E_{ii} is the energy spacing of the *i*th symmetric (with respect to the Fermi level E_f) van Hove singularities and E_{laser} is the laser photon energy inducing the Raman scattering.

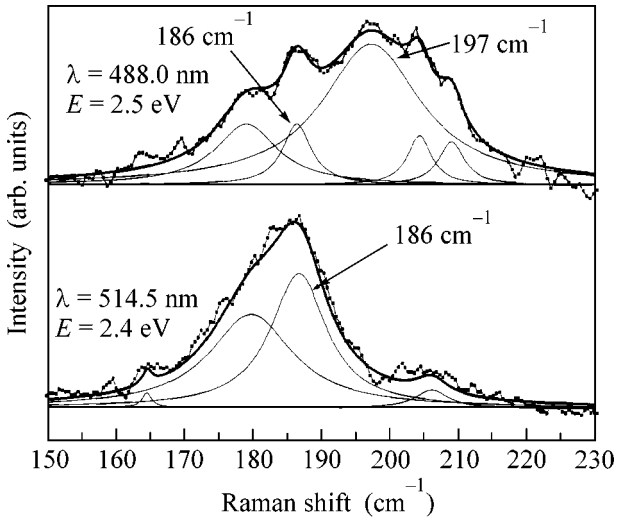

Fig. 4. Breathing mode region in the Raman spectrum of single-wall carbon nanotubes (obtained by laser ablation) for different wavelengths of the exciting laser radiation. The dotted line represents the experimental data, and the thin lines, the decomposition of the breathing mode spectrum into Lorentz modes; the thick line is the approximation of the experimental data by the summation of the Lorentz modes.

that, as the nanotube diameter increases, the calculated gap width E_{ii} decreases. The dependence obtained from the calculation coincides, to a high accuracy, with the data reported in [8, 9]. This coincidence testifies to the correct operation of the program.

The second fact in support of the correctness of our calculations is that the jumplike increase in the pseudogap width E_{ii} with the change from semiconducting to metallic tubes is reproduced. It is well known that, for tubes with a metallic conductivity, the value of E_{ii} is much greater than for semiconducting tubes of the same diameter. Metallic tubes include all armchair tubes and all arbitrary tubes for which the difference $(m - n)$ is a multiple of three [1]. The information on the nanotube conductivity type is not introduced into the computer program, and the input data include only the geometric parameters of nanotubes. Nevertheless, as the tube diameter monotonically varies, the calculated value of E_{ii} does increase in a jumplike manner for the tube geometries corresponding to metallic conductivity.

2.2. Experimental Verification of the Calculated Electronic Density of States for Specific Carbon Nanotubes by the Resonance Raman Scattering Method

For experimental verification of the calculated data obtained for the density of states in particular carbon nanotubes, we used the resonance Raman scattering method. The idea of the experiment consisted in the comparison between the real resonance excitation energy E_{laser} (laser wavelength) and its calculated value for those nanotubes whose breathing modes dominate the corresponding Raman spectrum. The confidence criterion for the calculation was formulated as the existence of no less than one geometric nanotube configuration with the diameter corresponding to the frequency of the breathing mode, for which one of the energy pseudogaps E_{ii} coincides with E_{laser} (Fig. 3).

Figure 4 presents the Raman spectra obtained for single-wall carbon nanotubes in the breathing mode region with different energies of the exciting laser radiation. The tubes were synthesized by laser ablation. One can see that, as the laser energy varies (from 2.4 eV at λ = 514.5 nm to 2.5 eV at λ = 488.0 nm), the profile of the breathing modes in the Raman spectrum changes; intensity is redistributed between peaks corresponding to different frequencies, and peaks either appear or disappear. One can conclude that, for each specific laser energy, the modes of those tubes dominate the spectrum, for which the resonance excitation conditions are satisfied; i.e., one of the energy spacings E_{ii} becomes equal to the photon energy of the laser radiation (Fig. 3). When the energy of the exciting radiation changes, the Raman resonance response is shifted to nanotubes with a different diameter.

The information on the true diameter of the "resonant" nanotubes can be obtained from the spectral characteristics of the breathing modes that dominate the Raman spectrum. Modes with different frequencies correspond to nanotubes of different diameters. In the general case, the breathing mode frequency in the

Table 1. Excitation energy of 2.4 eV

Nanotube type	Diameter, Å	Energy spacing E_{33}, eV
(12,7)	13.04	2.3
(13,6)	13.18	2.6
(16,2)	13.39	2.6
(17,0)	13.32	2.7

Table 2. Excitation energy of 2.5 eV

Nanotube type	Diameter, Å	Energy spacing E_{33}, eV
(11,7)	12.31	2.3
(13,5)	12.61	2.4
(14,3)	12.31	2.5
(15,2)	12.61	2.6
(16,0)	12.54	2.4

Raman spectrum depends on the nanotube diameter according to the relation [18]

$$\omega = C_1/d + C_2, \quad (7)$$

where ω is the frequency (cm^{-1}), d is the nanotube diameter (nm), and C_1 and C_2 are constants.

According to [18–20], the constant C_2 is determined by the van der Waals interactions in the beam, and the choice of the constant C_1 is determined by the dispersion curve [21]. For nanotubes obtained by laser ablation, these constants are $C_1 = 234$ and $C_2 = 10$ cm^{-1}.

According to Eq. (7), in the case shown in Fig. 4, the resonance conditions sequentially fall on nanotubes with diameters of about 13.2 Å (the breathing mode frequency is 186 cm^{-1}) and 12.5 Å (197 cm^{-1}). Tables 1 and 2 show the values of energy spacing E_{33} for nanotubes of different configurations with diameters of about 13.2 and 12.5 Å, which provide the closest coincidence with the laser radiation energy.

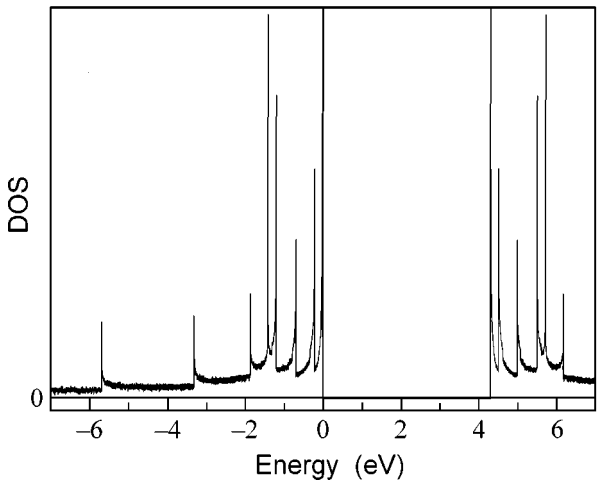

Fig. 5. Calculated electronic density of states for (10,10) single-wall BN nanotubes.

From the tables, one can see that a (12,7) nanotube has a diameter close to that calculated by Eq. (7) for a nanotube excited by a wavelength of 514.5 nm, as well as an energy spacing close to the laser photon energy at this wavelength (2.4 eV). For the radiation with a wavelength of 488 nm (2.5 eV), the same properties are characteristic of a (14,3) nanotube (Fig. 3).

Thus, the experiment showed that, for two particular nanotubes, namely, (12,7) and (14,3), the calculated parameters of the density of states adequately represent the shift of the resonance Raman response from one nanotube to another when the wavelength of the exciting radiation changes from 514.5 to 488.0 nm.

2.3. Modeling of the Electronic Density of States for Single-Wall Boron Nitride Nanotubes of Different Geometries

The modeling of the electronic structure was also performed for BN nanotubes of all possible geometric configurations. As an example, in Fig. 5 we present the density of states for (10,10) single-wall BN nanotubes. One can see that, for these tubes, the band gap is much greater than for carbon nanotubes. This result holds for all geometries of BN nanotubes, signifying that none of them is metallic.

CONCLUSIONS

Modeling of the electronic density of states was performed for single-wall carbon and BN nanotubes of all allowed geometries. The calculations are based on the use of the original computer program that performs numerical differentiation by the Monte Carlo method for two-dimensional dispersion relations for graphite and hexagonal boron nitride. The differentiation is performed for all allowed values of the wave vector using the π-electron approximation.

The estimates of the third pseudogaps E_{33} that occur in the densities of states of (12,7) and (14,3) chiral nanotubes are used as an example to demonstrate the good agreement between the calculated and experimental data.

The experimental energy values were obtained from the resonance effect observed in the Raman spectra of single-wall carbon nanotubes. The effect consisted in the change in the frequency of the dominant breathing mode when the wavelength (energy) of the exciting laser radiation was changed. The frequencies of the dominant breathing modes were determined. On the basis of these values, the diameters of nanotubes satisfying the resonance Raman scattering conditions were determined. The electronic densities of states were cal-

culated for all possible geometries of nanotubes with these diameters. The possibility of choosing the nanotube geometry with one of the pseudogaps corresponding to the laser excitation energy is indicated.

A computer program that allows one to calculate the density of states for BN nanotubes of all possible configurations is developed. A semiempirical formula describing the dispersion surface for hexagonal BN is derived. The absence of BN nanotube configurations with metallic conductivity is demonstrated. The program is shown to be suitable for calculating the density of states in nanotubes formed from other layered materials on the condition that the corresponding two-dimensional dispersion relation is introduced.

This work was supported by the Russian Foundation for Basic Research (project no. 01-02-17358), the Scientific Schools program (project no. 00-15-96559), INTAS-00-237, and the SCOPES 7SUPJ062400. A.V. Osadchy appreciates the ISSEP postgraduate grant and the support of the Moscow Government in 2002–2003.

REFERENCES

1. M. S. Dresselhaus, G. Dresselhaus, and P. C. Eklund, in *Science of Fullerenes and Carbon Nanotubes* (Academic, New York, 1996).
2. J. W. Mintmire and C. T. White, Phys. Rev. Lett. **81**, 2506 (1998).
3. L. C. Wildoer, A. G. Venema, A. Rinzler, *et al.*, Nature **391**, 59 (1998).
4. H. Kataura, Y. Kumazawa, Y. Maniwa, *et al.*, Synth. Met. **103**, 2555 (1999).
5. A. M. Rao, E. Richter, S. Bandow, *et al.*, Science **275**, 187 (1997).
6. M. S. Dresselhaus, G. Dresselhaus, A. Jorio, *et al.*, Carbon **40**, 2043 (2002).
7. E. D. Obraztsova, J.-M. Bonard, V. L. Kuznetsov, *et al.*, Nanostruct. Mater. **12**, 567 (1999).
8. R. Saito and H. Kataura, in *Carbon Nanotubes: Synthesis, Structure, Properties, and Applications*, Ed. by M. S. Dresselhaus, G. Dresselhaus, and P. Avouris (Springer, Berlin, 2002), p. 213.
9. M. S. Dresselhaus, in *Carbon Filaments and Nanotubes: Common Origins, Differing Applications*, Ed. by L. P. Biro *et al.* (Kluwer Academic, Dordrecht, 2001), p. 11, NATO ASI Ser., Ser. E, Vol. 372.
10. S. Reich and C. Thomsen, Phys. Rev. B **62**, 4273 (2000).
11. A. Rubio, J. L. Corkill, and M. L. Cohen, Phys. Rev. B **49**, 5081 (1994).
12. B. G. Demczyk, J. Cumings, A. Zettl, and R. O. Ritchie, Appl. Phys. Lett. **78**, 2772 (2001).
13. D. V. Kirin and P. N. D'yachkov, Dokl. Akad. Nauk, Ser. Khim. **373**, 344 (2000).
14. R. S. Lee, J. Gavillet, M. Lamy de la Chapelle, *et al.*, Phys. Rev. B **64**, 121405 (2001).
15. A. Rothschild, R. Popovits-Biro, O. Lourie, *et al.*, J. Phys. Chem. B **104**, 8976 (2000).
16. M. Renskar, Z. Skraba, F. Cleton, *et al.*, Appl. Phys. Lett. **69**, 351 (1996).
17. Y.-N. Xu and W. Y. Ching, Phys. Rev. B **44**, 7787 (1991).
18. H. Kuzmany, W. Plank, H. Hulman, *et al.*, Eur. Phys. J. B **22**, 307 (2000).
19. L. Henrard, V. N. Popov, and A. Rubio, Phys. Rev. B **64**, 205403 (2001).
20. A. M. Rao, J. Chen, E. Richter, *et al.*, Phys. Rev. Lett. **86**, 3895 (2001).
21. S. L. Fang, A. M. Rao, P. C. Eklund, *et al.*, J. Mater. Res. **13**, 2405 (1998).

Translated by E. Golyamina

JETP Letters, Vol. 77, No. 8, 2003, pp. 411–414. Translated from Pis'ma v Zhurnal Éksperimental'noĭ i Teoreticheskoĭ Fiziki, Vol. 77, No. 8, 2003, pp. 485–488.

Photoluminescence of GeO_2 Films Containing Germanium Nanocrystals

V. A. Volodin[1, *], E. B. Gorokhov[1], M. D. Efremov[1], D. V. Marin[1], and D. A. Orekhov[2]

[1] *Institute of Semiconductor Physics, Siberian Division, Russian Academy of Sciences, pr. Akademika Lavrent'eva 13, Novosibirsk, 630090 Russia*

** e-mail: volodin@isp.nsc.ru*

[2] *Novosibirsk State University, ul. Pirogova 2, Novosibirsk, 630090 Russia*

Received March 4, 2003

Germanium nanocrystals were formed in a GeO_2 film during the process of germanium monoxide gas-phase deposition onto a sapphire substrate and studied by photoluminescence (PL) and Raman scattering spectroscopy. A PL peak in this heterosystem was observed in the visible region at room temperature. The sizes of Ge nanocrystals were estimated from the position of a Raman peak corresponding to scattering by localized optical phonons in germanium. The PL peak position calculated with allowance for the electron and hole size quantization in Ge nanocrystals coincides well with the experimentally observed position of this peak. © *2003 MAIK "Nauka/Interperiodica".*

PACS numbers: 78.67.Pt; 78.55.-m; 78.30.-j

Interest in studying germanium and silicon nanocrystals in dielectrics is caused by the possible use of these structures in optoelectronic devices. The compatibility of the approaches used for their preparation with traditional "silicon" technology, as well as the possibility of modifying their optical properties caused by quantum size effects (bandgap engineering), are particularly attractive. The optical properties of the silicon and germanium nanocrystals prepared by various techniques in silicon dioxide and silicon nitride films were investigated earlier in [1–6]. The optical properties of germanium nanocrystals in GeO_2 have almost not been investigated to date. In this work, they were studied using photoluminescence (PL), Raman scattering, and light transmission methods. The express and nondestructive Raman scattering method, in conjunction with calculations [7, 8], is quite informative in the study of nanoobjects. The position of the Raman peak corresponding to the scattering from optical phonons is determined by the nanocrystal size, and it can be determined by the convolution of effective density of states [9].

Experimental samples were prepared by germanium monoxide gas-phase deposition onto a sapphire substrate at a temperature of 500°C. The deposition technique is described in detail in [10]. It was shown by ellipsometry, electron microscopy, and IR spectroscopy that the deposited film represented a heterosystem consisting of Ge and GeO_2 [10]. According to the ellipsometric data, the film was 0.33 μm in thickness. It was kept in the open form and was not coated with layers protecting from the atmosphere. The PL was excited by a pulsed N_2 laser (λ = 337 nm), and the spectra were recorded using a SDL-1 spectrometer with a FEU-79 photomultiplier as a detector. The transmission spectra were recorded by a SF-20 double-beam spectrometer. The Raman spectra were excited by a 514.5-nm (2.41 eV) Ar laser line and recorded at room temperature on an automated setup based on a DFS-52 spectrometer. The quasi-backscattering $Z\langle XY\rangle\bar{Z}$ geometry was used, for which the polarization planes of the incident and scattered light were mutually perpendicular.

The transmission spectrum of the heterosystem "Ge nanocrystals:GeO_2/Al_2O_3" is given in Fig. 1a. After approximating the transmission spectra with allowance for light interference in the structure, it was found that the film thickness was 0.33 μm, which coincided with the ellipsometric data, and the absorption edge was calculated for the film. One can see from Fig. 1a that the absorption edge (≈1.8 eV) strongly differs from the germanium bandgap (0.67 eV) [11]. The optical gap in GeO_2 equals ~5.5 eV [12], whence it follows that the absorption is due to the germanium inclusions. Such a strong difference can be caused by the quantum size effects in germanium nanocrystals. Since the barriers for electrons and holes in the germanium surrounded by GeO_2 are equal, respectively, to approximately 2 and 3 eV [12], the object under study is a quantum dot of type I. Because of the strong electron and hole localization and the removal of momentum selection rule, one can assume that the radiative electron–hole recombination becomes more efficient. Indeed, a peak in the red–yellow spectral range is seen in the PL spectrum at room temperature (Fig. 1b). No PL from the sapphire substrate was observed in this range. The large peak width and asymmetry are probably caused by the scat-

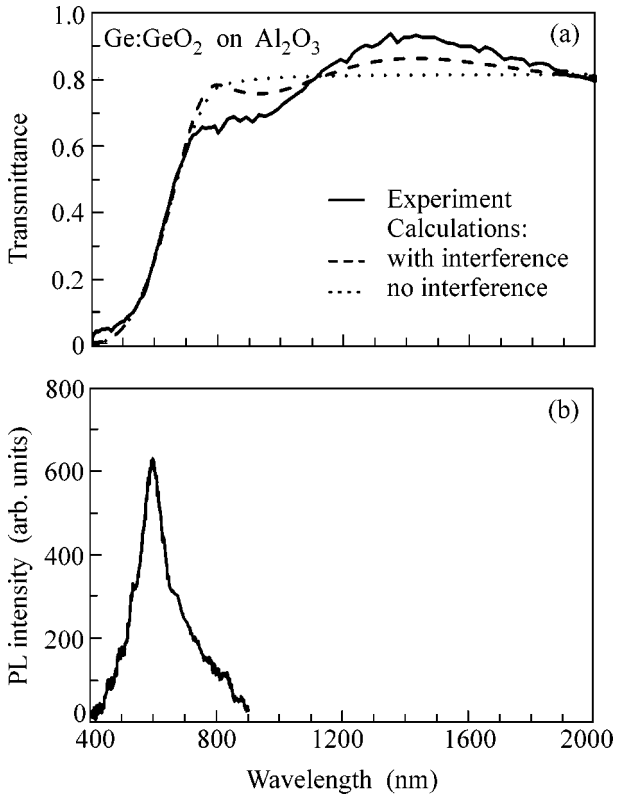

Fig. 1. (a) The experimental and calculated transmission spectra of a GeO_2 film with germanium nanocrystals, and (b) the PL spectra of this structure (T = 300 K).

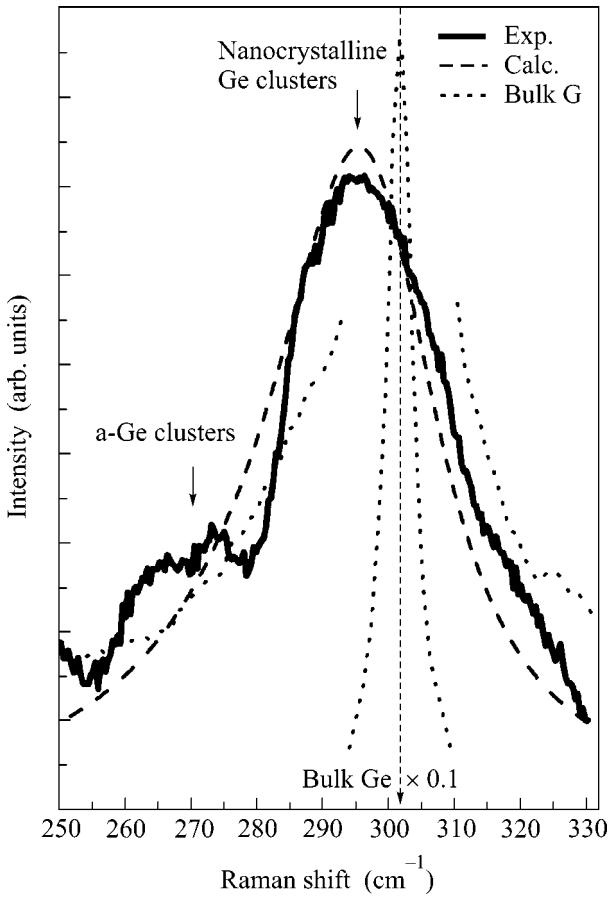

Fig. 2. Experimental and calculated Raman scattering spectra of a GeO_2 film with germanium nanocrystals. The spectrum of bulk germanium is shown for comparison.

ter of nanocrystal sizes. The PL maximum occurs at 2.09 eV, and, hence, the shift ΔE from the germanium bandgap is 1.42 eV.

To estimate the average size of germanium nanocrystals, the Raman spectrum of the structure was studied in the optical range (Fig. 2). The nanocrystal peak is shifted to lower frequencies from its position in a bulk germanium. A weak peak due to the scattering by the amorphous germanium clusters is also seen. Since the momentum selection rules are removed in the finite-size nanocrystals, vibrational modes with nonzero wavevectors are also seen in their Raman spectra. If the nanocrystal shape is close to a sphere, the Raman intensity can be written as [9]

$$I(\omega) = A \times \sum_{i=1}^{6} \int_{0}^{1} [n(\omega_i(q)) + 1] \frac{4\pi q^2 \exp(-q^2 r_0^2/4)}{(\omega - \omega_i(q))^2 + (\Gamma/2)^2} dq, \quad (1)$$

where $n(\omega)$ is the Bose–Einstein occupation number, $\omega_i(q)$ is the dispersion of the ith phonon branch, Γ is the line width, r_0 is the nanocrystal radius, and q is the wavevector. The dispersion curves for germanium were approximated by harmonic functions fitted to the experimentally measured dispersion curves [13]. From comparison of the experimental and calculated data, it is seen that the average radius of the germanium nanocrystals is 1.3 nm. The calculated spectrum is also shown in Fig. 2. Our estimates are in compliance with the frequencies calculated for the localized optical phonons in the crystalline germanium clusters using a microscopic valence-force model [14]. Note that, for the molar ratio $Ge : GeO_2 = 1 : 1$, which follows from the procedure of heterofilm preparation, and considering that the densities of Ge and amorphous GeO_2 are different, the average separation between the spherical nanoparticles in the oxide is always equal to ~1/2 of their diameter, i.e., to ~1.3 nm in our case. That is, for a diameter of ~3 nm, the nanocrystal density in the layer cross section is equal to ~10^{13} cm^{-2}.

The energies of localized electron and hole states in the germanium nanocrystals were also calculated. The valence band maximum in germanium occurs at the Γ point. The effective heavy-hole mass m_{hh} in germanium is equal to $0.33m_0$, and the mass of light holes m_{lh} is $0.042m_0$. The conduction band minimum lies along the (111) direction, with $m_{e\perp} = 0.082m_0$ and $m_{e\parallel} = 1.58m_0$, where m_0 is the electron mass [11].

The energy levels in a spherically symmetric well with radius r_0 and a barrier height U_0 were found in the following way [15]. After the separation of variables, one arrives at the following equation for the radial wave function:

$$\frac{1}{r^2}\frac{\partial^2}{\partial r^2}(r^2\Psi(r)) - \frac{L(L+1)}{r^2}\Psi(r) + \frac{2m(r)}{\eta^2}(E - U(r))\Psi(r) = 0. \quad (2)$$

We are interested in the ground state, for which the orbital angular momentum L is zero and the equation becomes one-dimensional with the potential well $U(r)$. For an infinite potential, it is solved exactly to give for a finite solution inside the well at $r = 0$

$$\Psi = A\frac{\sin(\alpha r)}{r}, \quad \alpha = \frac{\sqrt{2mE}}{\eta} = \frac{\pi}{r_0}. \quad (3)$$

Being localized, the states with wavevectors both along and transverse to the (111) direction will mix together; for this reason, following the approach described in [16], we took the electron effective mass in the form $m_e = 3m_{e\perp}m_{e\|}/(2m_{e\|} + m_{e\perp})$, so that $m_e = 0.123$. The hole level was calculated for heavy holes with $m_{hh} = 0.33$ [11]. Then, if the energy is measured in electron-volts and the well radius in nanometers, one has

$$E_{tr} = E_g + 4.1/r_0^2. \quad (4)$$

The solution for a finite barrier was found by matching the wave function and its derivative at the well boundary (m_{well} and m_{bar} are the effective masses in the well and barrier, respectively):

$$\Psi_{well} = \Psi_{bar}, \quad \Psi'_{well}/m_{well} = \Psi'_{bar}/m_{bar}. \quad (5)$$

The corresponding equations were solved numerically both without and with taking account of the differences in electron and hole masses inside the well and in the barrier. Although the electron and hole masses in GeO_2 are unknown, we considered GeO_2 a high-energy-gap material and assumed, as in [16], that the carrier masses are close to the free-electron mass. The computational results are shown in Fig. 3. One can see that, for the finite electron and hole barriers, the calculated optical transition energy of a germanium nanocrystal with a radius of 1.3 nm (Raman scattering data) coincides with the position of the PL peak.

Let us touch some aspects of bandgap engineering in a heterosystem "quantum dots in a dielectric matrix." The technology of a film heterosystem $Ge:GeO_2$ allows one to vary its optical properties in various ways, among which are

(1) the modification of Ge nanocrystal sizes by varying temperature and germanium monoxide condensation rate during the course of synthesis;

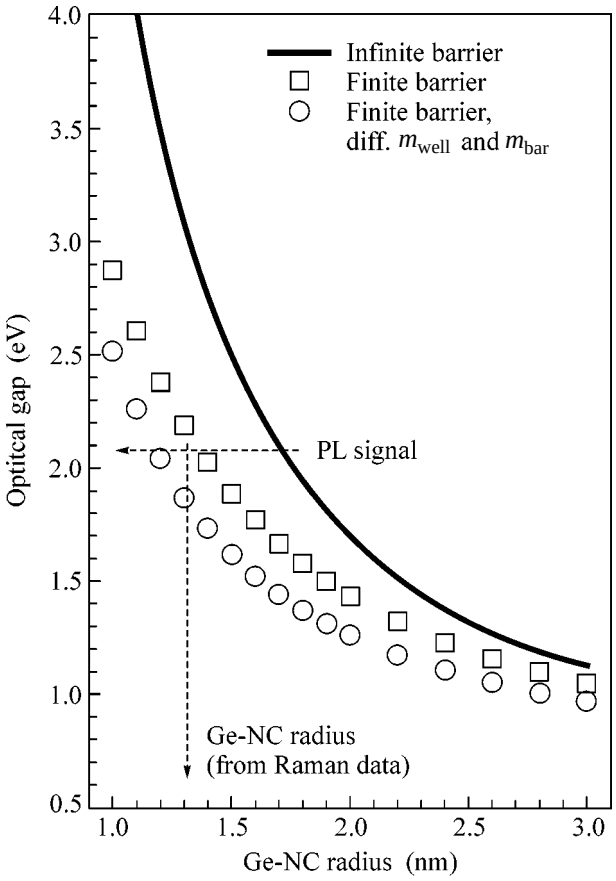

Fig. 3. The optical gap in spherical germanium nanocrystals (Ge NC) surrounded by GeO_2, as calculated for a finite barrier and with allowance for the difference in masses.

(2) a controlled increase in the sizes of Ge nanocrystals and barrier width between them (without changing the Ge : GeO_2 ratio in the film) through the diffusion-controlled transformation of small Ge clusters into large clusters during annealing in an inert medium;

(3) a controlled decrease in the nanocrystal sizes by oxidation (the temperatures of all processes are below 550°C);

(4) variation of the potential barrier height for the quantum wells in a heterosystem through chemical and phase transformations of the system components [17]. In particular, the fraction x in a germanosilicate glass $GeO_{2(x)}:Si_{2(1-x)}$ may change from 1 to 0, and, simultaneously, the optical and electronic parameters of the dielectric change continuously and almost linearly [18–20]. For the bandgap E_g, this implies an increase from ~5.5 to ~9 eV;

(5) the possible use of glasses with complex composition and their crystallization at low temperatures (below 650–700°C [19, 21, 22]), which also modifies the properties of dielectric barriers. Note that the dielectric constant of a film increases (by ~20% on the average) upon crystallization, which is favorable to the

devices of the "quasi-nonvolatile MOS memory" type on the quantum-dot traps [17].

Note in conclusion that the PL signal in the GeO_2 films containing germanium nanocrystals is observed at room temperature. Since the electron and hole barriers in the Ge:GeO_2 heterostructure are appreciably lower than in the Ge:SiO_2 structure (which was already used in the fabrication of the experimental specimens of optoelectronic devices [23]), this structure seems to be more efficient for electron and hole injection and, hence, holds promise for the fabrication of optoelectronic elements on its base.

We are grateful to the students of the Novosibirsk State University L.L. Rapatskiĭ and K.S. Pervunin for assistance in measurements and processing of transmission spectra.

REFERENCES

1. T. T. Shimizu-Iwayama, K. Fujita, S. Nakao, *et al.*, J. Appl. Phys. **75**, 7779 (1994).
2. G. A. Kachurin, S. G. Yanovskaya, V. A. Volodin, *et al.*, Fiz. Tekh. Poluprovodn. **36**, 685 (2002) [Semiconductors **36**, 647 (2002)].
3. S. Takeoka, M. Fujii, S. Hayashi, *et al.*, Phys. Rev. B **58**, 7921 (1998).
4. I. E. Tyschenko, V. A. Volodin, L. Rebohle, *et al.*, Fiz. Tekh. Poluprovodn. **33**, 559 (1999) [Semiconductors **33**, 523 (1999)].
5. N.-M. Park, C.-J. Choi, T.-Y. Seong, *et al.*, Phys. Rev. Lett. **86**, 1355 (2001).
6. D. Nesheva, C. Raptis, A. Perakis, *et al.*, J. Appl. Phys. **92**, 4678 (2002).
7. M. D. Efremov, V. A. Volodin, V. A. Sachkov, *et al.*, Pis'ma Zh. Éksp. Teor. Fiz. **70**, 73 (1999) [JETP Lett. **70**, 75 (1999)].
8. N. N. Ovsyuk, E. B. Gorokhov, V. V. Grishchenko, *et al.*, Pis'ma Zh. Éksp. Teor. Fiz. **47**, 248 (1988) [JETP Lett. **47**, 298 (1988)].
9. V. Pailard and P. Puech, J. Appl. Phys. **86**, 1921 (1999).
10. E. B. Gorokhov, V. V. Grishchenko, N. N. Ovsyuk, and L. I. Fedina, Poverkhnost **10**, 82 (1990).
11. V. I. Gavrilenko, A. M. Grekhov, D. V. Korbutyak, and V. G. Litovchenko, *Optical Properties of Semiconductors* (Naukova Dumka, Kiev, 1987).
12. A. M. Mishchenko, Preprint IFP SO RAN (Inst. of Semiconductor Physics, Siberian Division, Russian Academy of Sciences, Novosibirsk).
13. G. Nelin and G. Nilsson, Phys. Rev. B **5**, 3151 (1972).
14. Shang-Fen Ren and Wei Cheng, Phys. Rev. B **66**, 205328 (2002).
15. L. D. Landau and E. M. Lifshitz, *Course of Theoretical Physics*, Vol. 3: *Quantum Mechanics: Non-Relativistic Theory*, 4th ed. (Nauka, Moscow, 1989; Pergamon, New York, 1977).
16. V. A. Burdov, Fiz. Tekh. Poluprovodn. **36**, 1233 (2002) [Semiconductors **36**, 1154 (2002)].
17. Y. C. King, T. J. King, and C. Hu, in *Technical Digest of International Electron Devices Meeting* (1998), p. 115.
18. E. B. Gorokhov, A. M. Mishchenko, I. G. Kovalenko, *et al.*, Poverkhnost **5**, 67 (1983).
19. E. B. Gorokhov, I. G. Kosulina, S. V. Pokrovskaya, and I. G. Neizvestny, Phys. Status Solidi **101**, 451 (1987).
20. E. B. Gorokhov, S. V. Pokrovskaya, and I. G. Neizvestnyĭ, Poverkhnost **4**, 103 (1983).
21. E. B. Gorokhov and A. L. Aseev, in *Semiconductors*, Ed. by I. G. Neizvestnyĭ (Inst. Fiz. Poluprovodn. Sib. Otd. Ross. Akad. Nauk, Novosibirsk, 1995), p. 199.
22. E. B. Gorokhov, Poverkhnost **9**, 76 (1992).
23. L. Rebohle, J. von Borany, D. Borchert, *et al.*, Electrochem. Solid-State Lett. **4**, G57 (2001).

Translated by V. Sakun

JETP Letters, Vol. 77, No. 8, 2003, pp. 415–419. Translated from Pis'ma v Zhurnal Éksperimental'noĭ i Teoreticheskoĭ Fiziki, Vol. 77, No. 8, 2003, pp. 489–493.

Magnetic "Doublets" in Mössbauer Spectra of Superparamagnetic Particles

A. M. Afanas'ev and M. A. Chuev

Institute of Physics and Technology, Russian Academy of Sciences, Nakhimovskiĭ pr. 36, Moscow, 117218 Russia

Received March 7, 2003

It is shown that the Mössbauer magnetic hfs spectra of a superparamagnetic particle are cardinally affected by the rotation of its magnetic moment about the magnetic anisotropy field. This rotation renormalizes the nuclear *g* factors and qualitatively transforms the spectra. In particular, apart from the well-known magnetic sextet, five, four, three, and even two (magnetic "doublet") lines can arise in the ^{57}Fe absorption spectra. © *2003 MAIK "Nauka/Interperiodica".*

PACS numbers: 76.80.+y; 31.30.Gs

For over half a century, Mössbauer spectroscopy has served as a powerful tool for studying hyperfine (hf) interactions in solids. By now, it would seem that the formation mechanisms have been firmly established for the hfs spectra. The vast majority of experimental spectra are analyzed on the basis of static hfs, for which the line positions and intensities can be described in terms of static magnetic and electric fields acting on nuclei. For instance, the magnetic hfs spectrum of the most frequently used ^{57}Fe isotope consists of six lines, so-called magnetic sextet, while the line-intensity ratios are determined by the selection rules. The role of relaxation processes, which chaotically vary the hyperfine field at the nucleus, was also studied in detail [1–3]. Depending on the relaxation rate, the spectral lines broaden or the magnetic hfs collapses into a single line (or into a quadrupole doublet if the electric field gradient at the nucleus is nonzero).

In superparamagnetic particles, apart from the chaotic fluctuations, the hf magnetic field rotates due to the rotation of the magnetic moment of a particle in the magnetic anisotropy field. Although the rotation has an appreciable effect on the hfs spectra, it is ordinarily assumed that the rotation frequency Ω far exceeds the typical hf interaction frequencies [4]. In this case, the off-diagonal part of the hf interaction is averaged to zero, while the remaining diagonal part is again described by a static magnetic hf field (slightly lowered because of averaging), so that the spectral structure, e.g., the magnetic sextet for the ^{57}Fe nuclei, is retained.

In this work, general formulas are derived for the hfs spectra with an arbitrary Ω, and it is shown that, under these conditions, the spectra may be cardinally different from the static hfs spectra. In particular, instead of a magnetic sextet, the spectra of the ^{57}Fe isotope may show five, four, three, and even two (magnetic doublet) lines. The corresponding hfs spectrum depends not only on the magnitude of Ω but also on its sign, which, in turn, may be dictated by the sign of magnetic anisotropy constant.

The theory of Mössbauer spectra for a hyperfine field $\mathbf{H}_{hf}(t)$ varying in time along an arbitrary determinate trajectory was developed in [5–7], mainly with the aim of describing the effect of an external magnetic rf field on the absorption spectra. The following expression was obtained for the gamma-ray absorption cross section by a nucleus:

$$\sigma(\omega) = \frac{2}{\Gamma_0 T_{hf}}\mathrm{Re}\int_0^{T_{hf}} dt_0 \times \int_{t_0}^{\infty}\mathrm{Sp}\left\{\hat{V}^+\left[\hat{T}\exp\left\{\int_{t_0}^{t} i[(\omega + i\Gamma_0/2)\hat{\mathbf{I}} - \hat{\mathbf{L}}_{\hat{H}}(t')]dt'\right\}\right]\hat{V}\right\}dt, \quad (1)$$

where ω is the spectral frequency, Γ_0 is the width of nuclear excited level, $T_{hf} = 2\pi/\Omega$ is the hyperfine-field time period, $\hat{V}$ is the operator of interaction of a gamma-ray quantum with nucleus, $\hat{T}$ stands for the chronological ordering, $\hat{\mathbf{I}}$ is a unit operator, and the Liouvillean superoperator $\hat{\mathbf{L}}_{\hat{H}}(t)$ is determined by the time-dependent Hamiltonians of nuclear hyperfine interactions in the ground (*g*) and excited (*e*) states,

$$\hat{H}^{(g,e)}(t) = -g_{g,e}\mu_N\mathbf{H}_{hf}(t)\hat{\mathbf{I}}^{(g,e)}, \quad (2)$$

where μ_N is the nuclear magneton, $g_{g,e}$ are the nuclear *g* factors, and $\hat{\mathbf{I}}^{(g,e)}$ are nuclear spins. The superoperator $\hat{\mathbf{L}}_{\hat{H}}(t)$ acts in the space of $(2I^{(g)} + 1)$, $(2I^{(e)} + 1)$ variables:

$$(\hat{\mathbf{L}}_{\hat{H}})_{m_e m_g m'_e m'_g} = \hat{H}^{(e)}_{m_e m'_e}\delta_{m_g m'_g} - \hat{H}^{(g)}_{m_g m'_g}\delta_{m_e m'_e}, \quad (3)$$

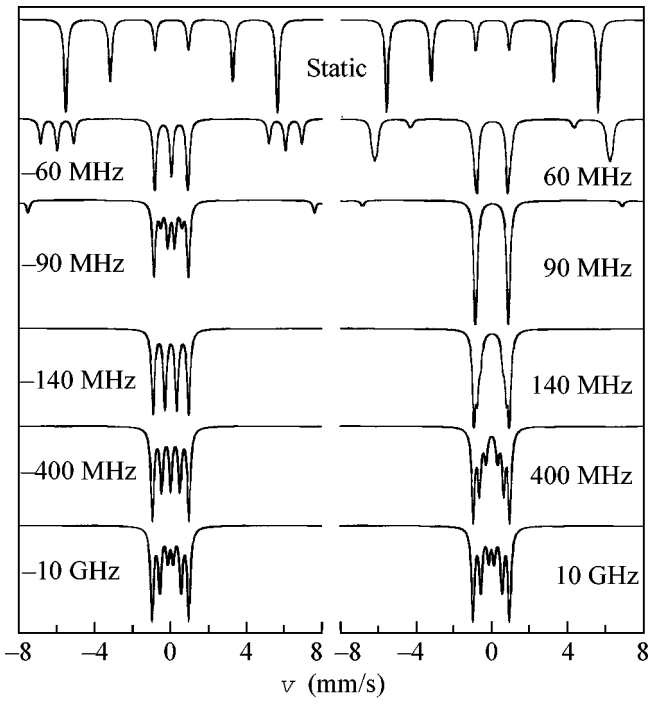

Fig. 1. ^{57}Fe Mössbauer absorption spectra (top curves) in a static hyperfine field and (lower curves) in the rotating hyperfine field ($\theta = 80°$) for various rotation frequencies $\Omega/2\pi$. Hereafter, the spectra are calculated for the nonpolarized gamma radiation, chaotic orientations of magnetic anisotropy axes, and $H_{hf} = 330$ kOe.

where $m_{g,e}$ are the nuclear spin projections onto some axis. Expression (1) was used to calculate the absorption spectra of nanostructured magnetic alloys subjected to an external rf field [8].

Assume that the hyperfine magnetic field rotates with frequency Ω about some axis z at the angle θ to this axis:

$$\begin{aligned}\mathbf{H}_{hf}(t) &= H_{hf}[\mathbf{n}_z\cos\theta \\ &+ (\mathbf{n}_x\cos(\Omega t) + \mathbf{n}_y\sin(\Omega t))\sin\theta],\end{aligned} \tag{4}$$

where $\mathbf{n}_x$, $\mathbf{n}_y$, and $\mathbf{n}_z$ are unit vectors along the x, y, and z axes, respectively. Expression (1) can be transformed using the superoperator

$$\begin{aligned}\hat{\mathbf{G}}(t_0, t) &= \hat{T}\exp\left(-i\int_{t_0}^{t}\hat{\mathbf{L}}_{\hat{H}}(t')dt'\right) \\ &= \hat{G}^{(e)}(t_0, t)\otimes\hat{G}^{(g)}(t, t_0),\end{aligned} \tag{5}$$

which is a direct product of the evolution operators for the ground and excited states:

$$\hat{G}^{(e,g)}(t_0, t) = \hat{T}\exp\left(-i\int_{t_0}^{t}\hat{H}^{(e,g)}(t')dt'\right). \tag{6}$$

Expression (6) can be greatly simplified after passing to the coordinate system rotating about the z axis with frequency Ω. This corresponds to the unitary transformations with the use of the operators of elementary rotation about the z axis. Then, in the evolution operators (6), one can perform integration with respect to time:

$$\begin{aligned}\hat{G}^{(e,g)}(t_0, t) &= e^{-i\Omega\hat{I}_z t_0}e^{i\Omega\hat{I}_z t_0} \\ &\times T\exp\left(-i\int_{t_0}^{t}\hat{H}^{(g,e)}(t')dt'\right)e^{-i\Omega\hat{I}_z t}e^{i\Omega\hat{I}_z t} \\ &\equiv e^{-i\Omega\hat{I}_z t_0}\exp(-i\hat{\tilde{H}}^{(g,e)}(t-t_0))e^{i\Omega\hat{I}_z t},\end{aligned} \tag{7}$$

where $\hat{\tilde{H}}^{(g,e)}$ are the time-independent hfs Hamiltonians in the rotating system of coordinates for the ground and excited states, respectively:

$$\hat{\tilde{H}}^{(g,e)} = (-\Omega + \omega_{g,e}\cos\theta)\hat{I}_z^{(g,e)} + \sin\theta\hat{I}_x^{(g,e)}, \tag{8}$$

and $\omega_{g,e} = -g_{g,e}\mu_N H_{hf}$ are the hfs constants for the ground and excited nuclear states.

By using Eq. (7), one can readily show that, in this case, Eq. (1) reduces to a rather simple analytic expression. After averaging over the incident radiation polarization η, one obtains for the absorption cross section

$$\begin{aligned}\sigma(\omega, \Omega, \theta) &= -\frac{\Gamma_0}{2}\mathrm{Im}\sum_{\eta}\sum_{\substack{m_g m_e \\ \tilde{m}_g\tilde{m}_e}} V^{(\eta)+}_{\tilde{m}_g\tilde{m}_e} \\ &\times\frac{\langle\tilde{m}_g|m_g\rangle\langle\tilde{m}_e|m_e\rangle}{\omega - (\tilde{\lambda}_e\tilde{m}_e - \tilde{\lambda}_g\tilde{m}_g) - \Omega(m_g - m_e) + i\Gamma_0/2}V^{(\eta)}_{m_e m_g},\end{aligned} \tag{9}$$

where $m_{g,e}$ are the z projections of the nuclear spin; $\tilde{m}_{g,e}$ are its projections onto the quantization axes, for which operators (8) are diagonal; and

$$\tilde{\lambda}_{g,e} = \sqrt{(-\Omega + \omega_{g,e}\cos\theta)^2 + \omega_{g,e}^2\sin^2\theta}. \tag{10}$$

Using Eq. (9), one can calculate absorption spectra as functions of rotation frequency Ω and angle θ. In Fig. 1, the ^{57}Fe Mössbauer spectra are shown for the case of hyperfine field rotating about the chosen axis at the angle $\theta = 80°$ for different frequencies Ω and different senses of rotation. One can clearly see that, for the levorotation ($\Omega < 0$), the spectra can take the form of a triplet, quartet, or quintet of lines, instead of the classical static magnetic hfs sextet (upper spectra in Fig. 1). At the same time, for the dextrorotation ($\Omega > 0$), the absorption spectra may collapse to a magnetic doublet. In other words, the hyperfine-field rotation cardinally changes the shape of hfs spectra.

The physical reason for such a cardinal spectrum transformation can be clarified by the example of a high hf-field rotation frequency ($|\Omega| \gg |\omega_{g,e}|$). One can see from Eqs. (9) and (10) that, in this case, the spectrum is

divided into a central group of six doubly degenerate lines and satellite lines. The analysis of the satellite shapes is of no interest in this situation, because, for high frequencies Ω, these satellites are far beyond the velocities of the standard Mössbauer spectrometers (Fig. 1). The main contribution to the absorption intensity comes from the central lines with $\tilde{m}_g = m_g$ and $\tilde{m}_e = m_e$. The approximate expression for the corresponding absorption cross section is

$$\sigma(\omega, \Omega, \theta) = -\frac{\Gamma_0}{2}\mathrm{Im}\sum_{\eta}\sum_{m_g m_e}\left|V^{(\eta)}_{m_e m_g}\right|^2 \times \frac{1}{\omega - (\tilde{\omega}_e m_e - \tilde{\omega}_g m_g) + i\Gamma_0/2}, \quad (11)$$

where

$$\tilde{\omega}_{g,e} = -\tilde{g}_{g,e}\mu_N H_{hf}\cos\theta \quad (12)$$

are, respectively, the effective nuclear ground- and excited-state hfs constants, which are found from Eq. (10) and determined by the renormalized nuclear g factors

$$\tilde{g}_{g,e} = g_{g,e}\left(1 - \frac{\omega_{g,e}}{2\Omega}\sin\theta\tan\theta\right). \quad (13)$$

It is seen from Eq. (12) that, in addition to the well-known effective (proportional to $\cos\theta$) decrease in the magnitude of hyperfine field [4], the rotation effect qualitatively transforms the hfs spectra through the renormalization of the nuclear g factors (13). The changes in the effective $\tilde{g}$ factors are different for the ground and excited nuclear states because of the different original nuclear g factors ($g_g = 0.18$ and $g_e = -0.10$ for the ^{57}Fe nuclei).

It follows from Eq. (13) that, upon the rotation with frequencies $\Omega > 0$, the absolute value of the $\tilde{g}$ factor decreases for the excited nuclear state and increases for the ground state. Hence, the excited-state $\tilde{g}_e$ factor can change sign for the angles θ close to $\pi/2$. For instance, if the angle θ and the rotation frequency Ω are related to each other by the condition

$$\Omega\cos\theta = \omega_e/2, \quad (14)$$

the effective excited-state $\tilde{g}_e$ factor becomes zero, and only a doublet will be observed in the magnetic hfs spectrum (on the right in Fig. 1). The level splitting scheme is shown for this case in Fig. 2.

In turn, for rotation with frequencies $\Omega < 0$, the absolute value of the ground-state $\tilde{g}$ factor will decrease, while the excited-state value will increase. For θ angles close to $\pi/2$, the $\tilde{g}_g$ factor may change sign. This is precisely the reason that underlies the cardinal rearrangement of the absorption spectra, i.e., the appearance of a triplet, quartet, or quintet in a series of

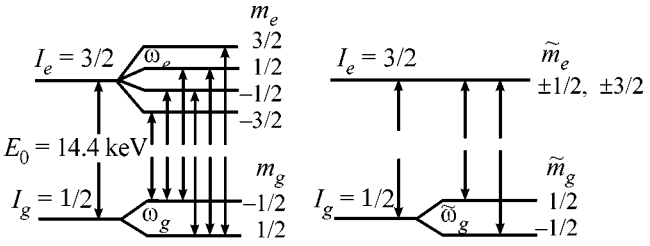

Fig. 2. Scheme of level splitting for the ^{57}Fe nucleus in the excited (e) and ground (g) states. Left: magnetic sextet in a static hyperfine field; right: magnetic doublet in the rotating hyperfine field satisfying condition (14), for which $\tilde{\omega}_e = 0$.

left-hand spectra shown in Fig. 1. In particular, if condition (14) is satisfied after replacing ω_e by ω_g, a magnetic quartet should be observed in the absorption spectrum.

For a uniformly magnetized axisymmetric particle, the magnetic-anisotropy energy density is given by the well-known expression [9]

$$E_{an} = -K\frac{M_z^2}{M_0^2} = -K\cos^2\theta, \quad (15)$$

where K is the magnetic-anisotropy constant, M_0 is the magnetic moment of a particle unit volume, and M_z is the projection of the magnetic moment onto the symmetry axis. In this case, one has for the magnetic-anisotropy field

$$H_{an} = -\partial E_{an}/\partial M_z = 2K\frac{M_z}{M_0^2} = K\cos\theta/M_0. \quad (16)$$

It is well known that, if a magnetic moment deviates by the angle θ from the magnetic-field direction, it precesses about this axis with the frequency [10]

$$\Omega = -\gamma H_{an} = \Omega_0\cos\theta, \quad (17)$$

where γ is the gyromagnetic ratio and

$$\Omega_0 = -2\gamma K/M_0. \quad (18)$$

One can see from these formulas that the precession frequency Ω is independent of the particle size and determined by the K constant and the deflection angle θ. An important point is that, for the near-zero θ, the precession frequency is maximal, and it becomes zero at $\theta = \pi/2$. Consequently, there always exists a range of angles θ where the frequency Ω is comparable to the frequencies of nuclear-spin precession in a hyperfine field.

At the same time, the sense of magnetic-moment rotation depends on the sign of the K constant. For $K > 0$, i.e., in the presence of easy magnetic axis, the hf field at the ^{57}Fe nuclei is levorotatory ($\Omega < 0$). For the anisotropy of easy magnetic-plane type ($K < 0$), the hf field at the ^{57}Fe is dextrorotatory ($\Omega > 0$). This fact is crucial for

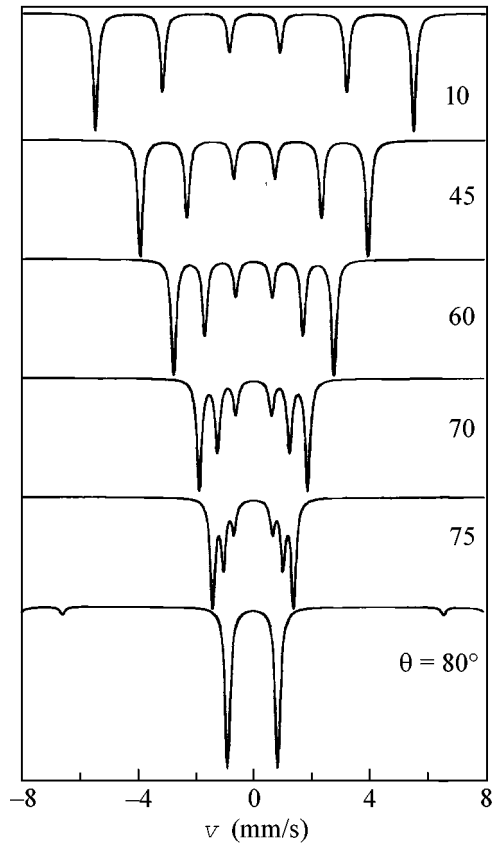

Fig. 3. ^{57}Fe Mössbauer absorption spectra in the rotating hyperfine field for various values of angle θ and the parameter $\Omega_0/2\pi = 0.5$ GHz.

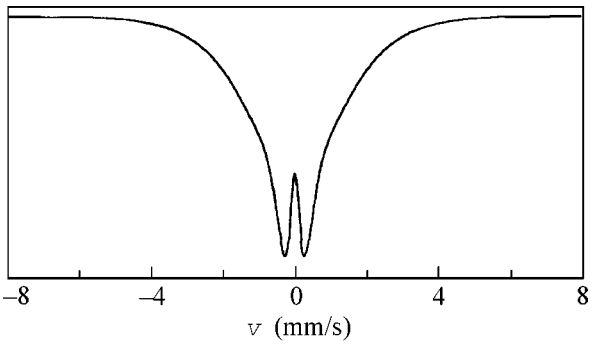

Fig. 4. ^{57}Fe Mössbauer absorption spectrum for a superparamagnetic particle with the magnetic anisotropy constant $K < 0$ ($\Omega_0/2\pi = 0.5$ GHz).

the transformation of Mössbauer spectra, as is clearly seen in Fig. 1.

In Fig. 3, the ^{57}Fe Mössbauer spectra are shown for the hf field rotating at various angles θ to the chosen axis and for the parameter $\Omega_0/2\pi = 0.5$ GHz corresponding to γ-Fe_2O_3 particles with an average diameter of 7 nm [11]. The magnetic hfs with the renormalized $\tilde{g}$ factors is clearly observed in the absorption spectra for $\theta > 70°$. With a decrease in the angle θ, the effect of fast rotation on the spectrum shape weakens, except for the effective increase in the magnitude of hf field. However, one should take into account that the rotation effect in the form of renormalized nuclear g factors should be observed not only for the nonstandard spectra, as shown in Fig. 1, but also in the case where the corresponding line shifts are comparable to the linewidth Γ_0. In particular, the effect of rotation with frequency $\Omega_0/2\pi$ on the order of 1 GHz becomes essential for the ^{57}Fe nuclei at $\theta > 30°$.

Modern technique allows the growth of magnetic particles with very small sizes, on the order of few nanometers (see, e.g., [11–15]). Due to the small volume, the total magnetic anisotropy energy KV (V is the particle volume) is on the order of several hundred degrees, so that all states with arbitrarily directed magnetic moments may become populated even at room temperature. In the absence of relaxation effects, the absorption spectrum of an individual particle with magnetic anisotropy (15) is expressed by the weighted sum of partial spectra (9) with different deviation angles θ:

$$\bar{\sigma}(\omega) = \int \sigma(\omega, \Omega_0 \cos\theta, \theta) P(\theta) \sin\theta d\theta, \qquad (19)$$

where $P(\theta)$ determines the population of states with different directions of magnetic moment at a given temperature T:

$$P(\theta) = C \exp\left(\frac{KV\cos^2\theta}{k_B T}\right) \qquad (20)$$

(k_B is the Boltzmann constant and C is the normalization factor).

One can see from Eq. (19) that the anomalies observed in the partial spectra in Fig. 1 should smear, to a large extent, in the resulting spectra of small superparamagnetic particles whose states with magnetic moments arbitrarily oriented about the anisotropy axis are all populated. Nevertheless, one can clearly see, even from the visual comparison of the left and right series in Fig. 1, that the degree of smearing should be substantially different for different senses of hyperfine-field rotation. For negative Ω frequencies ($K > 0$), the line positions in the partial spectra are widely scattered, so that no clear-cut structure should be observed in the resulting spectrum. At the same time, for rotation with positive Ω ($K < 0$), the topological shape of magnetic doublet is retained over a rather broad range of Ω frequencies (and, hence, over a broad range of angles θ for a given value of parameter Ω_0), allowing one to hope that the doublet can be observed in the resulting absorption spectrum. As an example, the ^{57}Fe absorption spectrum calculated by formula (19) with parameters $KV/k_BT = -5$ and $\Omega_0/2\pi = 0.5$ GHz is shown in Fig. 4. It is seen from this figure that a well-defined magnetic

doublet is retained in the resulting spectrum of a superparamagnetic particle.

REFERENCES

1. H. H. Wickman, in *Mossbauer Effect Methodology*, Ed. by I. J. Gruverman (Plenum, New York, 1966), Vol. 2.
2. M. Blume, Phys. Rev. **174**, 351 (1968).
3. A. M. Afanas'ev and V. D. Gorobchenko, Zh. Éksp. Teor. Fiz. **66**, 1406 (1974) [Sov. Phys. JETP **39**, 690 (1974)].
4. S. Mörup, J. Magn. Magn. Mater. **37**, 39 (1983).
5. A. M. Afanas'ev, M. A. Chuev, and J. Hesse, Phys. Rev. B **56**, 5489 (1997).
6. A. M. Afanas'ev, M. A. Chuev, and J. Hesse, Zh. Éksp. Teor. Fiz. **113**, 1799 (1998) [JETP **86**, 983 (1998)].
7. A. M. Afanas'ev, M. A. Chuev, and J. Hesse, Zh. Éksp. Teor. Fiz. **116**, 1001 (1999) [JETP **89**, 533 (1999)].
8. J. Hesse, T. Graf, M. Kopcewicz, *et al.*, Hyperfine Interact. **113**, 499 (1998).
9. L. D. Landau and E. M. Lifshitz, *Course of Theoretical Physics*, Vol. 8: *Electrodynamics of Continuous Media*, 4th ed. (Nauka, Moscow, 1992; Pergamon, New York, 1984).
10. A. Abragam and B. Bleaney, *Electron Paramagnetic Resonance of Transition Ions* (Clarendon Press, Oxford, 1970; Mir, Moscow, 1972), Vol. 1.
11. E. Tronc, A. Ezzir, R. Cherkaoui, *et al.*, J. Magn. Magn. Mater. **221**, 63 (2000).
12. S. Morup, Hyperfine Interact. **90**, 171 (1994).
13. I. P. Suzdalev, A. S. Plachinda, V. N. Buravtsev, *et al.*, Chem. Phys. Rep. **17**, 1355 (1998).
14. A. J. Hernando, J. Phys.: Condens. Matter **11**, 9455 (1999).
15. F. Bodker, M. F. Hansen, Ch. B. Koch, *et al.*, Phys. Rev. B **61**, 6826 (2000).

Translated by V. Sakun

JETP Letters, Vol. 77, No. 8, 2003, pp. 420–423. From Pis'ma v Zhurnal Éksperimental'noĭ i Teoreticheskoĭ Fiziki, Vol. 77, No. 8, 2003, pp. 494–497.

Unconventional Superconductivity in Two-Dimensional Electron Systems with Long-Range Correlations¶

V. A. Khodel[1] and V. M. Yakovenko[2]

[1] *Russian Research Centre Kurchatov Institute, Moscow, 123182 Russia*

[2] *University of Maryland, College Park, MD 20472-4111, USA*

Received March 7, 2003

Properties of superfluid states of two-dimensional electron systems with critical antiferromagnetic fluctuations are investigated. These correlations are found to result in the emergence of rapid variation in the momentum space terms in all components of the mass operator, including the gap function $\Delta(\mathbf{p})$. It is shown that the domain where these terms reside shrinks with temperature, leading to a significant difference between the temperature T_c, at which superconductivity is terminated, and the temperature T^*, where the gap in the single-particle spectrum vanishes. © *2003 MAIK "Nauka/Interperiodica".*

PACS numbers: 74.20.Mn

The problem of high-temperature superconductivity is known to defy solution within the Fermi liquid approach. Initially it looked like it had to do with only normal states of high-T_c superconductors. However, later it was acknowledged that the BCS theory fails in dealing with their superfluid states as well [1, 2]. This is best demonstrated by the persistence of a gap Δ in the spectra of single-particle (sp) excitations of many high-T_c superconductors above the critical temperature T_c, at which superconductivity disappears (the so-called pseudogap phenomenon [1–4]).

Another salient feature of a two-dimensional electron liquid of high-T_c superconductors is the universality of its phase diagram versus the doping x. At low $|x| \le x_c \simeq 0.05$, corresponding to a filling close to 1/2, two-dimensional compounds are antiferromagnetic insulators. At larger x, antiferromagnetic ordering is nil, but in the vicinity of the phase transition long-range correlations with wave vectors $\mathbf{q}$, close to the antiferromagnetic vector $\mathbf{Q} = (\pi, \pi)$, turn out to be drastically enhanced, which results in the divergence of the electron–electron scattering amplitude $\Gamma = \Gamma_0 + \Gamma_a\sigma_1\sigma_2$ with

$$\Gamma_a(\mathbf{q} \longrightarrow \mathbf{Q}, \omega \longrightarrow 0; x) \sim [(\mathbf{q}-\mathbf{Q})^2 + r_a^{-2}(x) + ic|\omega|]^{-1}, \quad (1)$$

the correlation radius $r_a(x)$ becoming infinite at $x = x_c$ [5, 6].

The impact of this singularity on sp properties is studied proceeding from the RPA formula $\Sigma_a = (\Gamma_a * G)$, which presents the part Σ_a of the mass operator Σ associated with antiferromagnetic fluctuations as a convolution of the amplitude Γ_a with the sp Green's function G (see, e.g., [5–9]). For a long time, attention was focused on the energy dependence of Σ, while its momentum-dependent part $\Sigma(\mathbf{p}, \varepsilon = 0)$ was parameterized by the effective mass m^*. This is justified in systems with short-range correlations, where the mass operator $\Sigma(\mathbf{p}, \varepsilon = 0)$ is a smooth function of $\mathbf{p}$. But this is not the case. Straightforward calculations show that long-range correlations (1) trigger a component $\Sigma_a(\mathbf{p})$ of the function $\Sigma(\mathbf{p}, \varepsilon = 0) \equiv \Sigma_r(\mathbf{p}) + \Sigma_a(\mathbf{p})$ rapidly varying with $\mathbf{p}$, being a convolution of Γ_a and the pole part G^q of the Green's function G. It should be emphasized that $\Sigma_a(\mathbf{p})$ has to be evaluated self-consistently, otherwise the flattening of the sp spectra $\xi(\mathbf{p})$ in normal states found in [10] and observed in many high-T_c compounds gets lost.

To get rid of the energy-dependent terms in Σ, we calculate the derivative $\partial \mathrm{Re}\Sigma(\mathbf{p}, \varepsilon)/\partial\mathbf{p} \longrightarrow (\mathrm{Re}\Gamma_a * \partial \mathrm{Im} G^q/\partial\mathbf{p})$. After simple algebra we obtain

$$\frac{\partial \mathrm{Re}\Sigma_a(\mathbf{p})}{\partial \mathbf{p}} = \frac{3}{2} z \times \int \Gamma_a(\mathbf{p}-\mathbf{p}_1, \omega = E(\mathbf{p})) \frac{\partial n(\mathbf{p}_1, T)}{\partial \mathbf{p}_1} d\tau_1. \quad (2)$$

Here, $z = [1 - (\partial\Sigma(\varepsilon)/\partial\varepsilon)_0]^{-1}$ is the renormalization factor, $d\tau = d^2p/(2\pi)^2$, and

$$n(\mathbf{p}, T) = v^2(\mathbf{p})(1 - f(E)) + (1 - v^2(\mathbf{p}))\, f(E) = \frac{1}{2} - \frac{\xi(\mathbf{p})}{2E(\mathbf{p})} \tanh\frac{E(\mathbf{p})}{2T} \quad (3)$$

is the quasiparticle momentum distribution. In this formula, $f(E) = (1 + \exp(E/T))^{-1}$, while $v^2(\mathbf{p}) = (E(\mathbf{p}) - \xi(\mathbf{p}))/2E(\mathbf{p})$, where $E(\mathbf{p}) = \sqrt{\xi^2(\mathbf{p}) + \Delta^2(\mathbf{p})}$ and Δ is the

¶This article was submitted by the authors in English.

gap function, while $\xi(\mathbf{p}) = z(\xi^0_{\mathbf{p}} + \Sigma_a(\mathbf{p}) + \Sigma_r(\mathbf{p})) \equiv \xi^0(\mathbf{p}) + z\Sigma_a(\mathbf{p})$ is the sp energy spectrum of the normal state measured from the chemical potential μ. To a good approximation, the spectrum $\xi^0(\mathbf{p})$ and the LDA electron spectrum $\xi^0_{\mathbf{p}}$ are related by $\xi^0(\mathbf{p}) = \xi^0_{\mathbf{p}}/m^*$.

In what follows, the argument $\omega = E(\mathbf{p}_1)$ of the function $\Gamma_a(\mathbf{p} - \mathbf{p}_1, \omega)$ in Eq. (2) is replaced by 0, since both the functions $\partial n(\mathbf{p}_1, T)/\partial \mathbf{p}_1$ and $\Gamma_a(\mathbf{p} - \mathbf{p}_1)$, taken at $\xi(\mathbf{p}) = 0$, are peaked at $\xi(\mathbf{p}_1) = 0$. Upon inserting this result into Eq. (2) and integrating over momenta, one finds

$$\xi(\mathbf{p}) = \xi^0(\mathbf{p}) + \frac{3}{2}z^2\int \Gamma_a(\mathbf{p} - \mathbf{p}_1)n(\mathbf{p}_1, T)d\tau_1. \quad (4)$$

The gap $\Delta(\mathbf{p})$, obeying the BCS gap equation, is also decomposed into the sum $\Delta(\mathbf{p}) = \Delta_a(\mathbf{p}) + \Delta_r(\mathbf{p})$ of a regular $\Delta_r(\mathbf{p})$ and a rapidly varying with $\mathbf{p}$ component $\Delta_a(\mathbf{p})$. In the case of singlet pairing, the respective equation for $\Delta_a(\mathbf{p})$ is [11]

$$\Delta_a(\mathbf{p}) = -3z^2\int \Gamma_a(\mathbf{p} - \mathbf{p}_1)\frac{\tanh\dfrac{E(\mathbf{p}_1)}{2T}}{2E(\mathbf{p}_1)}\Delta(\mathbf{p}_1)d\tau_1. \quad (5)$$

The analysis of solutions of the above nonlinear equations is greatly facilitated if the interaction (1), taken at $\omega = 0$, is approximated by a δ-function $\frac{3}{2}z^2\Gamma_a(\mathbf{q}) \longrightarrow f_a\delta(\mathbf{q} - \mathbf{Q})$ [5], appropriate in the domain of momentum space where the functions $n(\mathbf{p})$ and $\Delta_a(\mathbf{p})$ change more slowly than the amplitude $\Gamma_a(\mathbf{p} - \mathbf{p}_1)$. As a result, the integrations cancel, and we are left with

$$\begin{aligned}\xi(\mathbf{p}) &= \xi^0(\mathbf{p}) + f_a n(\mathbf{p} - \mathbf{Q}, T),\\ \xi(\mathbf{p} - \mathbf{Q}) &= \xi^0(\mathbf{p} - \mathbf{Q}) + f_a n(\mathbf{p}, T),\end{aligned} \quad (6)$$

$$\begin{aligned}\Delta(\mathbf{p}) &= -f_a\Delta(\mathbf{p} - \mathbf{Q})\frac{\tanh(E(\mathbf{p} - \mathbf{Q})/2T)}{E(\mathbf{p} - \mathbf{Q})},\\ \Delta(\mathbf{p} - \mathbf{Q}) &= -f_a\Delta(\mathbf{p})\frac{\tanh(E(\mathbf{p})/2T)}{E(\mathbf{p})},\end{aligned} \quad (7)$$

where the constant $f_a > 0$ is small compared to the band width ω_0. In obtaining these equations, we neglected the term $\Delta_r(\mathbf{p})$. Setting here $T = 0$, we arrive at a set of equations derived in [12] in a different way.

If pairing correlations are somehow suppressed, Eqs. (7) are knocked out. Upon solving the two remaining Eqs. (6), we find that, in the case when the van Hove points $(\pm\pi, 0)$ and $(0, \pm\pi)$ are situated quite close to the Fermi line (FL), the portion of the sp spectrum adjacent to the van Hove points (vHP) turns out to be flat [12]. We shall see later that the flattening holds if pairing correlations come into play.

As seen from Eqs. (7), the gap $\Delta(\mathbf{p})$ changes its sign going over to a neighbor vHP, as in the conventional D-pairing model, in which the gap $\Delta_D(\mathbf{p}) \sim (\cos p_x - \cos p_y) \neq 0$ anywhere in the momentum space but the zone diagonals. However, in contrast to this model, nontrivial solutions of Eqs. (7) exist only in a domain C, the boundaries of which are found by combining the two Eqs. (7), which yields

$$f_a^2\frac{\tanh(E(\mathbf{p})/2T)}{E(\mathbf{p})}\frac{\tanh(E(\mathbf{p} - \mathbf{Q})/2T)}{E(\mathbf{p} - \mathbf{Q})} = 1, \quad \mathbf{p} \in C. \quad (8)$$

Otherwise, $\Delta_a \equiv 0$, and $E(\mathbf{p}) = |\xi(\mathbf{p})|$, as in the Nozieres model [13–15] with the effective long-range interaction $\Gamma(\mathbf{q}) \sim \delta(\mathbf{q})$.

In overdoped compounds, the domain C is made up of two quite narrow stripes. The first, denoted further C_F and described by the equation $\xi^0(\mathbf{p}) = 0$, is adjacent to the FL. The second, associated with the conjugate line (CL), is determined by the equation $\xi^0(\mathbf{p} - \mathbf{Q}) = 0$. In these compounds, the FL and CL are well separated, and when dealing with $\mathbf{p} \in C_F$ the energy $E(\mathbf{p} - \mathbf{Q})$ can be replaced by $|\xi^0(\mathbf{p} - \mathbf{Q})|$, so that Eq. (8) is recast to

$$E(\mathbf{p}) = g(\mathbf{p})\tanh(E(\mathbf{p})/2T), \quad \mathbf{p} \in C_F, \quad (9)$$

with the coupling constant $g(\mathbf{p}) = f_a^2/|\xi^0(\mathbf{p} - \mathbf{Q})|$.

As x drops, the FL and the CL approach to meet each other at a critical doping x_m. In most high-T_c compounds, such as Bi2212, Bi2201, etc., the FL is concave, while the CL is convex, and the first meeting between these lines occurs at the vHPs. Close to the vHPs, the boundaries of the C domain are calculated combining Eq. (8) with the relations $E(\mathbf{p}) = |\xi^0(\mathbf{p})|$ and $E(\mathbf{p}) = |\xi^0(\mathbf{p}) + f_a|$, which yields restrictions $-2f < \xi^0(\mathbf{p}) < f$. In this case, Eq. (8) is easily solved, and close to the vHPs, the sp spectrum turns out to be quite flat: $E(\mathbf{p}, T = 0) \simeq f_a$. We see that this value is significantly in excess of those obtained if the FL and the CL have no points of intersection. When the gap landscape is drawn in the doping region $x \sim x_m$, it comprises four "twin towers," each one being associated with its own vHP. Each tower, whose height $\Delta_{vHP}(T = 0, x_m)$, according to Eq. (8), is equal to f_a, is connected with its neighbors by narrow "walls." According to Eq. (9), their height drops towards the zone diagonals, where the gap Δ vanishes. Thus, we infer that the gap function $\Delta(p_x, p_y)$ attains its maximum $\Delta_{\max}(T = 0) = f_a$ at the vHPs. This picture, confirmed by numerical calculations of [12], is in agreement with the available experimental data [2].

As T rises, the region C where $\Delta_a(\mathbf{p}) \neq 0$ shrinks, the effect first found in [15] under investigation of the Nozieres model [13]. Indeed, for points fairly far away from the vHPs, Eq. (9) can be employed. Its nontrivial solutions exist only if $g(\mathbf{p}) > 2T$. Since the function $|\xi^0(\mathbf{p} - \mathbf{Q})|$ identifying the energy splitting between the FL and the CL rises while the magnitude of the function

$g(\mathbf{p})$ drops, as the vector $\mathbf{p}$ moves along the FL towards the zone diagonal, the shrinkage begins in the diagonal region at $T_i(x) \simeq f_a^2/2|\xi_{\max}(x)|$, where $\xi_{\max}(x)$ is the bare sp energy, corresponding to the point of intersection between the CL and the zone diagonal. With further T increase, the shrinkage region is augmented, approaching the vHPs, where the gap Δ has its maximum value. Eventually, the whole C domain shrinks into several symmetric points at the FL, closest to the vHPs. Recently, such a behavior of the gap landscape, the so-called arc phenomenon [2], was experimentally observed. The final shrinkage temperature $T^*(x \sim x_m)$ is easily evaluated from Eq. (8). It is $T^*(x \sim x_m) \simeq f_a/2$, so that the gap $\Delta_{\max}(T = 0)$ and T^* are connected with each other by

$$\Delta_{\max}(T = 0) \simeq 2T^*, \quad x \sim x_m, \tag{10}$$

which is in accord with the available experimental data [1, 2].

It is worth noting that, inside the **C** region, the behavior of Δ remains the same as that in the BCS theory, since by retaining the leading terms in Eq. (9) one obtains

$$\Delta^2(\mathbf{p};\, T \longrightarrow T^*) \simeq 12T^*(T^* - T), \quad \mathbf{p} \in C. \tag{11}$$

Let us now turn to a rather rare case of the convex FL. Here the first intersection between the FL and the CL occurs at the zone diagonals, and if one rotates the entire zone picture by the angle $\phi = \pi/4$, these points will coincide with the intersection points between the FL and the CL in the case of the concave FL. The analysis shows that this feature seems to hold in dealing with all the solutions, including the gap landscape. We shall revisit this prediction of our model in a future paper.

So far we have neglected all the electron–electron interactions except the long-range one given by Eq. (1). By involving an electron–phonon exchange, the most pronounced out of the remaining ones, we trigger a regular component $\Delta_r(\mathbf{p}) \neq 0$ anywhere in the momentum space. As a result, the Landau criterion for superconductivity, which is violated in the above model at $T > T_i$, is now satisfied. Presumably, the magnitude of $\Delta_r(\mathbf{p})$ slowly varies with x, allowing us to estimate it from highly overdoped compounds. Since in this case T_c is small, we infer that the impact of Δ_r on properties of the superfluid state is insignificant. On the other hand, the electron–phonon exchange specified by the phonon propagator $D(\omega, k) = k^2/(\omega^2 - c^2k^2)$ gives rise to a renormalization of the constant f_a as well. The respective contribution $\delta\Delta(\mathbf{p})$ to the gap Δ is given by the integral

$$\delta\Delta(\mathbf{p}) \sim \int D(\mathbf{p} - \mathbf{p}_1, \omega_1)\frac{\Delta_a(\mathbf{p}_1)}{\omega_1^2 - E^2(\mathbf{p}_1)}d\tau_1\frac{d\omega_1}{2\pi i}. \tag{12}$$

Employing in the integral (12) the "tower" structure of the function $\Delta_a(\mathbf{p}, x \sim x_m)$, one can decompose overwhelming contributions into two: one from the same "tower" and the other from the neighboring one. The first contribution, proportional to the "tower" range, is small. When calculating the second one, where the momentum transfer $\mathbf{p} - \mathbf{p}_1$ is comparable to p_F, the propagator D can be replaced by –1, yielding a number that suppresses the initial f_a value. This interference may be significant.

Now we proceed to evaluation of the superfluid density $\rho_s(T)$, expressed in terms of a correlator of the velocities $\partial\xi^0(\mathbf{p})/\partial\mathbf{p}$. Evaluation of this correlator in crystals with the help of the Larkin–Migdal method [16, 17] yields

$$\rho_s(T) = -\frac{1}{2}\int\frac{\partial\xi^0(\mathbf{p})}{\partial p_i}\left[\frac{\partial n(\mathbf{p}, T)}{\partial p_i} - \frac{\partial f(E)}{\partial E}\frac{\partial\xi(\mathbf{p})}{\partial p_i}\right]d\tau, \tag{13}$$

the function $n(\mathbf{p}, T)$ being given by Eq. (3). In an ideal homogeneous Fermi gas, where $\xi(p) = p^2/2M - \mu$, Eq. (13) is converted into the ordinary textbook formula. Obviously, no contributions to ρ_s are made from regions in momentum space where the ratio $\Delta(\mathbf{p})/T$ is negligible. Indeed, if $\Delta(\mathbf{p}) = 0$, the distribution $n(\mathbf{p}, T)$ is converted to $n_F(\mathbf{p}, T) = (1 + \exp(\varepsilon(\mathbf{p})/T))^{-1}$, while the product $(\partial f(E)/\partial E)(\partial\xi(\mathbf{p})/\partial p_i) \longrightarrow \partial n_F(\mathbf{p}, T)/\partial p_i$, and both the terms in Eq. (13) cancel each other. As a result, at $T > \Delta_r$, contributions from regions other than the C domain may be neglected.

A full examination of the formula (13) will be performed elsewhere. Here we restrict ourselves to the region of the dopings $x \simeq x_m$ and temperatures $T \longrightarrow T^* \simeq f_a/2$. In this case, the ratio $E(\mathbf{p} \in C)/T$ is small, and an expansion of the terms in the integrand of Eq. (13) yields $\partial n(\mathbf{p}, T)/\partial p_i \simeq -(\partial\xi(\mathbf{p})/\partial p_i)/4T + \xi^2(\mathbf{p})(\partial\xi(\mathbf{p})/\partial p_i)/16T^3 + \Delta^2(\mathbf{p})(\partial\xi(\mathbf{p})/\partial p_i)/48T^3$ and $\partial f(E)/\partial E \simeq -1/4T + E^2(\mathbf{p})/16T^3$. After canceling similar terms and employing relation (11), we are left with

$$\rho_s(T \longrightarrow T^*) \simeq \frac{1}{48}\int_C\frac{\partial\xi_{\mathbf{p}}^0}{\partial p_i}\Delta^2(\mathbf{p})\frac{\partial\xi(\mathbf{p})}{\partial p_i}d\tau \simeq \alpha n(T^* - T)^2/T^{*2}, \tag{14}$$

where the numerical factor α is on the order of 10^{-2}. As we shall see, such a suppression of $\rho_s(T \longrightarrow T^*)$ results in a marked distinction between the critical temperature T_c for termination of superconductivity and the temperature T^* for vanishing of the gap Δ. The reason for that is a great diversity in the gap values, which, as we have seen, results in the temperature shrinkage of the domain of integration over momentum space in Eq. (13).

Strictly speaking, in two-dimensional systems, the temperatures T^* and T_c never coincide because of the Berezinsky–Kosterlitz–Thouless (BKT) phase transition [18–20], terminating superconductivity due to a spontaneous generation of an infinite number of vortices. This transition always occurs before vanishing of

the gap Δ. The BKT temperature, being, in fact, the critical temperature T_c, is given by the equation [18]

$$\pi T_c = 2\rho_s(T_c). \quad (15)$$

In conventional superconductors, where $\rho_s(T \longrightarrow T^*) \sim n(T^* - T)/T_c$ and, hence, $(T^* - T_c) \sim T_c^2/\epsilon_F^0$, the ratio T_c/ϵ_F^0 does not exceed 0.2%. However, in two-dimensional electron compounds with the doping $x \sim x_m$, the situation is different. Indeed, upon inserting the result (14) into Eq. (15), one obtains

$$T_c = \alpha_m \epsilon_F^0 (T^* - T_c)/T^*, \quad (16)$$

where the factor $\alpha_m \simeq 10^{-2}$. In high-T_c superconductors, the ratio T_c/ϵ_F^0 is on order of 10^{-2} and, hence, the ratio $\tau = (T^* - T_c)/T^*$ may attain values comparable to unity.

In conclusion, we have evaluated the effect of critical antiferromagnetic fluctuations on electron spectra and superfluid densities of superfluid states of overdoped and optimally doped high-T_c compounds. In underdoped electron systems, the situation is more complicated due to the emergence of a branch of low-lying collective excitations, whose contribution to properties is significant [21]. The interplay between these oscillations and critical fluctuations in underdoped compounds will be studied in a separate paper.

We thank L.P. Gor'kov, G. Kotliar, A.I. Lichtenstein, M.R. Norman, N.E. Zein, and M.V. Zverev for valuable discussions. We also thank ITF (Santa Barbara, USA) for the kind hospitality.

This work was supported in part by the National Science Foundation (grant no. PHY-0140316), by the McDonnell Center for the Space Sciences, and by the Russian Foundation for Basic Research (grant no. 00-15-96590).

REFERENCES

1. A. Damescelly, Z.-X. Shen, and Z. Hussein, cond-mat/0208504.
2. J. C. Campuzano, M. R. Norman, and M. Randeria, cond-mat/0209476.
3. Y. J. Uemura, G. M. Luke, B. J. Sternlieb, *et al.*, Phys. Rev. Lett. **62**, 2317 (1989).
4. Y. J. Uemura, L. P. Le, G. M. Luke, *et al.*, Phys. Rev. Lett. **66**, 2665 (1991).
5. A. Kampf and J. R. Schrieffer, Phys. Rev. B **41**, 6399 (1990).
6. A. J. Millis, H. Monien, and D. Pines, Phys. Rev. B **42**, 167 (1990).
7. S. Doniach and S. Engelsberg, Phys. Rev. Lett. **17**, 750 (1966).
8. A. M. Dyugaev, Zh. Éksp. Teor. Fiz. **70**, 2390 (1976) [Sov. Phys. JETP **43**, 1247 (1976)].
9. A. Abanov and A. Chubukov, Phys. Rev. Lett. **83**, 1652 (1999).
10. V. A. Khodel and V. R. Shaginyan, Pis'ma Zh. Éksp. Teor. Fiz. **51**, 488 (1990) [JETP Lett. **51**, 553 (1990)].
11. A. B. Migdal, *Theory of Finite Fermi Systems and Applications to Atomic Nuclei* (Nauka, Moscow, 1965; Interscience, New York, 1967).
12. M. V. Zverev, V. A. Khodel, and J. W. Clark, Pis'ma Zh. Éksp. Teor. Fiz. **74**, 48 (2001) [JETP Lett. **74**, 46 (2001)].
13. P. Nozières, J. Phys. I **2**, 443 (1992).
14. G. E. Volovik, Pis'ma Zh. Éksp. Teor. Fiz. **59**, 798 (1994) [JETP Lett. **59**, 830 (1994)].
15. J. Dukelsky, V. A. Khodel, P. Schuck, and V. R. Shaginyan, Z. Phys. B **102**, 245 (1997).
16. A. I. Larkin and A. B. Migdal, Zh. Éksp. Teor. Fiz. **44**, 1703 (1963) [Sov. Phys. JETP **17**, 1146 (1963)].
17. A. J. Millis, S. M. Girvin, L. B. Ioffe, and A. I. Larkin, J. Phys. Chem. Solids **59**, 1742 (1998).
18. J. M. Kosterlitz and D. Thouless, J. Phys. C **6**, 1181 (1973); J. Phys. C **7**, 1046 (1974).
19. D. Arioso and H. Beck, Phys. Rev. B **43**, 344 (1991).
20. V. J. Emery and S. A. Kivelson, Nature **374**, 434 (1995).
21. M. Eschrig and M. R. Norman, Phys. Rev. Lett. **85**, 3261 (2000).

JETP Letters, Vol. 77, No. 8, 2003, pp. 424–428. From Pis'ma v Zhurnal Éksperimental'noĭ i Teoreticheskoĭ Fiziki, Vol. 77, No. 8, 2003, pp. 498–502.

Suppression of 2D Superconductivity by the Magnetic Field: Quantum Corrections vs. the Superconductor–Insulator Transition¶

V. F. Gantmakher[1], S. N. Ermolov[1], G. E. Tsydynzhapov[1], A. A. Zhukov[1], and T. I. Baturina[2]

[1] *Institute of Solid State Physics, Russian Academy of Sciences, Chernogolovka, Moscow oblast, 142432 Russia*

[2] *Institute of Semiconductor Physics, Siberian Division, Russian Academy of Sciences, Novosibirsk, 630090 Russia*

e-mail: gombo@issp.ac.ru

Received March 20, 2003

Magnetotransport of superconducting $Nd_{2-x}Ce_xCuO_{4+y}$ (NdCeCuO) films is studied in the temperature interval 0.3–30 K. The microscopic theory of the quantum corrections to conductivity, both in the Cooper and in the diffusion channels, qualitatively describes the main features of the experiment, including the negative magnetoresistance in the high-field limit. Comparison with the model of the field-induced superconductor–insulator transition is included and a crossover between these two theoretical approaches is discussed. © *2003 MAIK "Nauka/Interperiodica".*

PACS numbers: 74.40.+k; 74.20.Mn; 74.78.Bz; 74.25.Ha; 75.70.Ak

The superconductor–insulator transition (SIT) is an example of a quantum phase transition [1], which constitutes a drastic change of the ground state of the system at zero temperature with variation of a parameter. The field was pioneered by Goldman *et al.* in 1989 [2], who obtained the transition from an insulating to superconductive state in a thin Bi film with the change of its thickness. Later, Fisher [3] suggested the existence of magnetic-field-induced SIT in two-dimensional (2D) systems, and Hebard and Paalanen demonstrated [4, 5] such a transition in amorphous InO_x films. Numerous results obtained in several other materials by different groups [6–9] were also interpreted within the framework of the field-induced SIT. The main arguments in favor of this interpretation were the negative derivative of resistance $\partial R/\partial T$ in fields above the critical and the existence of a finite-size scaling, i.e., the existence of some critical region on the (T, B)-plane where the behavior of the system was governed by competition of the quantum phase transition correlation length $\xi \propto (B - B_c)^{-\nu}$ and thermal length $L_T \propto T^{1/z}$ with z and ν being constants called the critical exponents. All relevant quantities in this region are supposed to be universal functions f of the ratio of the lengths, which can be written in the form of scaling variable $(B - B_c)/T^{1/z\nu}$. For the resistivity in two dimensions $R_\square$, this dependence takes form [3]

$$R_\square(B, T) = R_c f[(B - B_c)/T^{1/z\nu}], \qquad (1)$$

where R_c is a constant on the order of $h/4e^2 \approx 6.5\ \mathrm{k}\Omega$. It is called the critical resistance.

In the analysis of experiments [6–9], the negative derivative $\partial R/\partial T$ was rated as an indicator of the insulating state. However, that is not enough: the characteristic of any insulator is the exponential temperature dependence of the resistance. This was demonstrated only in InO_x films [10]. The growth of the resistance with decreasing temperature on the nonsuperconducting side of the field-induced transition in the experiments with MoGe [6], MoSi [7], and NdCeCuO [8, 9] was minuscule, about ten percent at most. It rather reminded a metal with quantum corrections to its conductivity than an insulator. Usually, the authors do not dwell on the issue, considering weak localization-like behavior to be the telltale sign of insulator, since, according to scaling hypothesis [11], there is no nonsuperconducting delocalized state at zero temperature in 2D and weak localization is expected to transform sooner or later into strong. However, this crossover might be postponed to an extremely low temperature, which would never be achieved in practice.

There exists one more sign of SIT. According to the boson–vortex duality model [1, 3], the insulating state that appears as the result of SIT is rather specific: it contains pair correlations between the localized electrons as the remnant of the superconducting pairing. Such an insulator is called a Bose insulator [5], and the correlated electrons are called localized electron pairs. These correlations should be destroyed by strong magnetic field, leading to increase of the carrier mobility, to negative magnetoresistance [12], and even to a reentrant insulator–normal-metal transition [10]. Negative mag-

¶This article was submitted by the authors in English.

netoresistance was observed in MoSi [13] and NdCeCuO [9]. But it was much weaker than in InO, just the same as the growth of the resistance with decreasing temperature discussed above.

When comparing the whole set of data in InO [4, 5, 10, 14] with those in MoGe [6], MoSi [7], and NdCeCuO [9], one cannot help thinking that they have many similar features, although they are of different scales of magnitude. At the same time, it was shown in a set of InO_x films with various oxygen content x that in low-resistivity films a transition to the metallic state replaces SIT, the rate of the temperature dependence scales down, and the whole pattern of curves approaches that of the usual superconducting transition [10, 14]. The main idea of this paper follows from this observation. It is to compare the experimental set of data of a "small-scale" type with the theory of the superconducting transition in the dirty limit and, keeping in mind its features related to SIT, to build a bridge between SIT and the thermodynamic superconducting transition.

The experiment was performed on 1000-Å-thick films of $Nd_{2-x}Ce_xCuO_{4+y}$ (NdCeCuO) obtained by laser ablation with CuO_2 planes parallel to the plane of the film. Films were not superconductive as-grown. In order to obtain superconductivity, they were annealed at 720°C in flowing ^{4}He gas for several hours. As we aimed to study vicinity of the SIT, we were not trying to reach maximal T_c of this material but were paying attention to smoothness and width of the zero-field transition. A sample was chosen with zero-field transition temperature $T_{c0} = 11.8 \pm 0.4$ K (found by fitting the superconducting fluctuation contribution to the conductivity above T_{c0}) and the transition width $\Delta T \simeq 2$ K.

The resistivity was measured in the *ab* plane by the four-terminal technique. Both current and potential probes were attached on the surface of the films by silver paste. The distance between potential probes corresponded to one square. A magnetic field was applied perpendicular to the film plane (along the *c* axis). Data were obtained, both as a function of field at constant temperature and as a function of temperature at constant field, though only the latter will be presented below. The upper panel of Fig. 1 presents an overview of the impact of the field on $R(T)$ dependence and the lower one zooms in on the region of interest, i.e., on the low-temperature and high-field region.

On the right axis of Fig. 1, the resistance reduced per one CuO_2 plane per square is denoted. As NdCeCuO is highly anisotropic [15], it is reasonable to assume the film to be a stack of 2D conducting CuO_2 planes with interplane spacing 6 Å, quasi-independent and connected in parallel. This is supported by observations of 2D character of quantum interference corrections [16] and magnetoresistance [17]. Later, we continue discussion in terms of this variable, disregarding full resistivity and actual thickness of the film. As one can see from

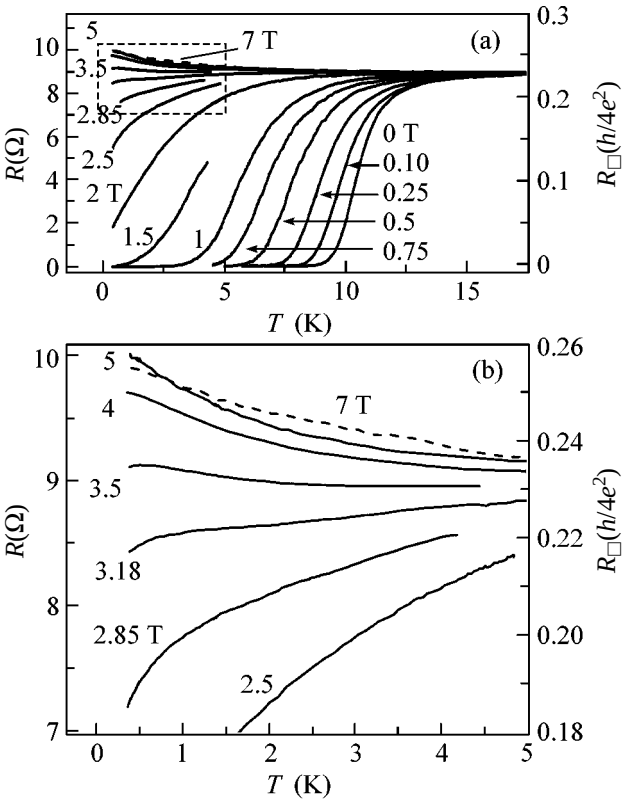

Fig. 1. Low-temperature resistivity data for the NdCeCuO film. The enlarged designated area of panel (a) is shown on panel (b). Curve at 7 T (dashed line) is crossing the other ones manifesting the negative magnetoresistance below 1 K.

Fig. 1, the value of the resistance per layer stays quite far from the quantum resistance $h/4e^2$ expected for the SIT.

The data are quite typical for the material (cf., for example, Ichikawa *et al.* [9]). In the low-field region, the transition is shifted to the lower temperature as the field increases, while the shape of the transition is preserved relatively well. Above 2 T, the transition broadens drastically and eventually disappears; at about 3.5 T, the dR/dT changes its sign. At higher fields, above 5 T, the resistance starts to decrease with the increasing field; it follows from the crossing of the 5 T and 7 T curves that a region of the negative magnetoresistance exists below 0.8 K and at $B > 5$ T.

The set of curves $R(T)$ on the lower panel of Fig. 1 is similar to those obtained in [6–9], which had been regarded as a field-induced SIT. Low-field curves (which bend down) may be supposed to reach zero resistivity at zero temperature and to become a superconductor, while high field curves (which bend up) may be supposed to diverge toward zero temperature and become an insulator. In between, there is a curve which is almost horizontal; it manifests itself as a common crossing point of all isotherms on the R–B graph. The corresponding state should be considered as the critical one with the temperature-independent resistance at the

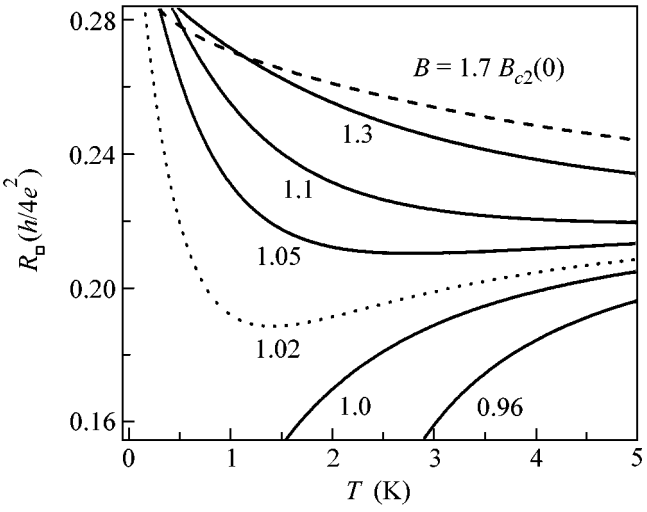

Fig. 2. Functions $R(T)$ at different B calculated from Eqs. (2) and (3). The curves are labeled by reduced field values. The curve that shows the negative magnetoresistance is marked by dashed line. The dotted curve should not be compared to experiment (see text).

critical field $B_c \approx 3.5$ T. But instead of seeking scaling parameters, we shall compare experimental data with the microscopic theory of the superconducting transition in the dirty limit formulated in terms of quantum corrections to the classical Drude conductivity $\sigma_0 = e^2/h(k_F l)$, where k_F is the Fermi wavevector and l is the elastic mean free path. This comparison became possible due to recent progress in calculation of the corrections due to superconducting fluctuations [18].

All quantum corrections fall into two categories—a one-particle correction, usually called weak localization, and those due to *e–e* interactions. The latter are divided into a diffusion channel correction (also known as the Aronov–Altshuler term) and Cooper channel corrections (also known as superconductive fluctuations corrections, which include Aslamazov–Larkin, Maki-Thompson, and DOS terms). Weak localization and Aronov–Altshuler corrections diverge at $T \longrightarrow 0$, while Cooper channel corrections diverge at $T \longrightarrow T_c(B)$, with $T_c(B)$ being mean field transition temperature. When the superconductivity is suppressed by the magnetic field, $T_c(B) \longrightarrow 0$ and all corrections are important.

Recently, Galitski and Larkin [18] succeeded in extending calculations in the Cooper channel for two-dimensional superconductors to the low temperature $T \ll T_c(0)$ and high magnetic field $B \gtrsim B_{c2}(0)$. The correction to the conductivity in the dirty limit $\delta\sigma$ is obtained as the sum of contributions of ten Feynman diagrams in the first (one-loop) approximation and can be written in the form

$$\delta\sigma = \frac{4e^2}{3\pi h}\left[-\ln\frac{r}{b} - \frac{3}{2r} + \psi(r) + 4(r\psi'(r) - 1)\right], \quad (2)$$

where $r = (1/2\gamma')(b/t)$, $\gamma' = e^\gamma = 1.781$ is the exponential of Euler's constant, and $t = T/T_{c0} \ll 1$ and $b = (B - B_{c2}(T))/B_{c2}(0) \ll 1$ are reduced temperature and magnetic field.

To compare these calculations with the experiment, we added to the correction (2) an additional term to account for Aronov–Altshuler contribution, which is assumed to be field independent. Weak localization was omitted, because we are interested in the region of rather strong magnetic fields, where this correction was expected to vanish. Finally, we arrived at the formula

$$R^{-1}(B, T) = \sigma_0 + \delta\sigma(B, T) - \alpha\frac{e^2}{h}\ln(T/T^*). \quad (3)$$

Inserting $T_{c0} = 11.8$ K and the experimental value of the classical conductivity $\sigma_0 = 1/R$ (7 T, 20 K) and choosing $T^* = 20$ K to make the last term zero at 20 K and $\alpha = 1/2$ match the temperature dependence of the experimental curve at 7 T, we get the plot of Fig. 2, which can be compared with the experimental one (Fig. 1b). (Note that in Fig. 2, curves are labeled by reduced field values, those in units of $B_{c2}(0)$. The same cannot be done on Fig. 1, because the experimental value of $B_{c2}(0)$ is a bit uncertain.)

As one can see, the picture bears a clear resemblance to the experiment—there is separation between low-field curves, which "bend down," and the high-field, which "bend up"; there is also high field negative magnetoresistance at low temperature. There are two remarkable points: (i) the scales of variation of resistance both with temperature and magnetic field are correct and (ii) the region and the magnitude of the negative magnetoresistance are in reasonable agreement with the experiment as well.

However, the similarity is qualitative. It is difficult to make it quantitative, and both the experiment and the theory are responsible for this.

The disadvantage of the experiment is hidden in the macroinhomogeneity of the film. It follows from Fig. 2 that small 2–3% changes of $B_{c2}(0)$ lead to a drastic shift in the shape of $R(T)$ curves, especially near the critical value of B. Inevitable dispersion of the values of $B_{c2}(0)$ along the film smoothes the curves and clears away the extremum. Hence, one should scarcely expect to find in the experimental assortment of curves one similar to the theoretical curve labeled 1.02 (plotted by the dotted line on Fig. 2).

The expression (2) is apparently very sensitive to the function $B_{c2}(T)$. Basically, this function is an implicit parameter of the theory. In [18], the authors used for $B_{c2}(T)$ the mean-field function from the Werthamer–Helfand–Hohenberg theory. It is doubtful that this theory is applicable to high-resistive 2D objects, especially since the shape of transition in the 2D case should be affected by the vortex motion (Berezinsky–Kosterlitz–Thouless theory).

As a side note, a comment about the finite-size scaling equation (1) related to SIT. Certainly, expression (3) does not have the form of equation (1) and no genuine scaling exists. However, in a restricted region of values of T and B, representation of the *theoretical* curves in the form (1) can be done. This is illustrated by Fig. 3, where calculated data from the region $0.98 < B/B_{c2}(0) < 1.2$ and $0.1 < T/T_c < 0.15$ are used for the tracing. As the "critical" magnetic field $B^* = 1.016B_{c2}(0)$, the crossing point of several isotherms $R(B)$ was taken; B^* is the field where the minimum of the isomagnetic curve $R(T)$ is located in the middle of the chosen temperature region. (Actually, in the limited range of parameters B and T, scaling always exists, provided that several $R(B)$ curves have a common crossing point.) It follows that the scaling tracing is a necessary but not sufficient element of the analysis of the SIT, especially taking into account that we always deal with a limited temperature range in the experiment.

The appearance of the negative correction to conductance in the microscopic theory of the superconductive fluctuations [18] is very remarkable. It confirms that the superconducting correlations may lead, at fields above the critical one, not to a drop but to an *upsurge* of the resistance. This can be regarded as a tendency toward a Bose insulator, which can be distinguished from the Aronov–Altshuler term because it leads to a negative magnetoresistance. All the materials mentioned above can be lined up demonstrating continuous crossover from the Bose insulator and gigantic negative magnetoresistance in InO_x to faint low-temperature rise of the resistance and its tiny drop in strong magnetic fields in MoSi and NdCeCuO. In essence, these films are similar to each other: they are uniform, highly disordered films, with the resistance close to the quantum value $h/4e^2$. Nevertheless, experimental observations on InO_x and, for example, on NdCeCuO are quite different, and there is a reason for it.

There is little doubt that at low enough temperature the growth of $R(T)$ we observe in high magnetic field, i.e., in the normal state, will become exponential. According to the phenomenological estimate suggested by Larkin and Khmel'nitskii [19], the crossover happens when the corrections to the conductivity reach the level of the conductivity itself. The condition $\sigma_0 \sim (e^2/h)\ln T$ gives the crossover temperature

$$T_{LKh} \simeq \frac{\varepsilon_F}{k_F l} e^{-2(k_F l)}, \qquad (4)$$

where ε_F and k_F are the Fermi energy and the Fermi wavevector and l is the elastic mean free path [19]. Below this temperature, there will definitely be a superconductive state at low field and pronounced insulating behavior at high field, and there would be clear reason to apply SIT framework. So, the quantum corrections to the conductivity and the quantum phase transition phenomena are manifested in different temperature regions.

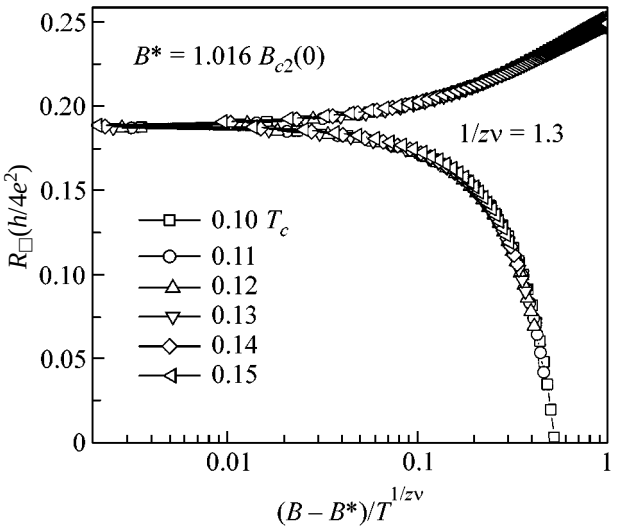

Fig. 3. "Scaling" of the curves calculated from Eqs. (2) and (3) in the same way as Fig. 2. Restricted ranges of T and B are selected (see text).

Though T_{LKh} may be very low for a normal metal ($T_{LKh} \lesssim 1$ mK already for $k_F l \approx 5$), there are clear experimental indications that crossover to bosonic insulator behavior (that is, to the SIT framework) in the intermediate field range, where pair correlations are still important, occurs at a higher temperature [10]. This is consistent with the theoretical observation [20] that the attractive interaction stimulates localization by combining single particles into pairs.

By equating the two last terms in the relation (3) to the σ_0 and solving the resulting equation, one gets the crossover temperature to bosonic insulator T_0 as a function of the magnetic field. These curves for σ_0 equal $5e^2/h$ (or $k_F l = 5$), $7e^2/h$, and $9e^2/h$ and are represented in Fig. 4 by solid lines. Thin solid lines represent levels of T_{LKh} determined by using only the last term in relation (3) and corresponding σ_0. As equation (2) is valid only in fields close to $B_{c2}(0)$, the parts of the curves in higher fields, where $T_0(B)$ approaches T_{LKh}, are indicated qualitatively by dotted lines. In agreement with [10, 20], the crossover to activation behavior in the medium-range fields occurs at temperatures more than order of magnitude higher than T_{LKh}. At the same time, the crossover temperature falls off exponentially with increasing classical conductivity, so that for the actual value of our experiment it becomes infinitesimal. That is why field-induced SIT is so manifest in the InO_x, whereas it is not observed in MoGe or NdCeCuO, and there is not the slightest sign of it in the Al film (note that, according to scaling hypothesis [11], any metal film should become insulating at $T = 0$ if the superconductivity is destroyed by the magnetic field).

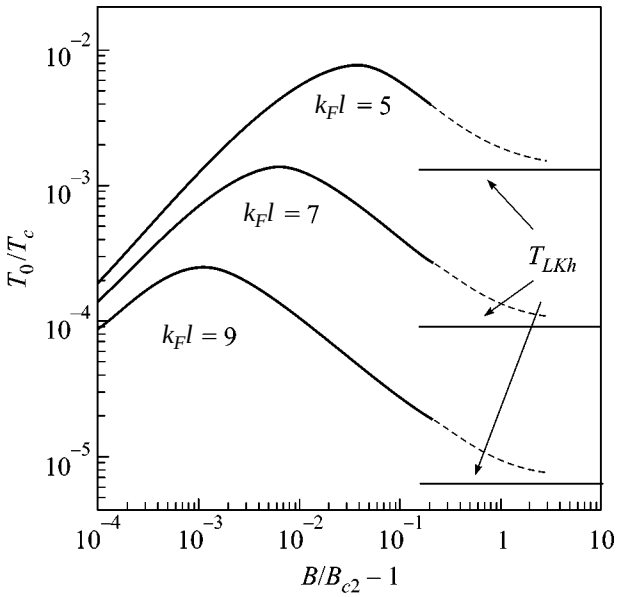

Fig. 4. Crossover temperature T_0 for several reduced values of the mean free path l calculated by equating to zero the right part of Eq. (3) for the fields values up to $B = 1.2B_{c2}(0)$. Dotted lines qualitatively designate the asymptotic parts of the curves. Levels of T_{LKh} approximately corresponding to the same values of l are marked by horizontal lines.

To summarize, we compared experimental data obtained on two-dimensional NdCeCuO superconductor in magnetic field at low temperature with the calculations of quantum corrections to the conductivity and found reasonable agreement. Lack of the activation behavior at high fields (on the "insulating side of transition") was the main reason that made inferior the comparison of the same data with the model of field-induced SIT. Apparently, this happened because the temperature range turned out to be too high for this specific material. The type of the resistance dependence on the temperature is the guide in choosing the theoretical approach. To employ the framework of the SIT in full for NdCeCuO, further substantial lowering of the temperature is necessary.

This work was supported by the Russian Foundation for Basic Research (grant nos. 02-02-16782, 02-02-08004, and 03-02-16368) and by a grant from the Ministry of Science.

REFERENCES

1. S. L. Sondhi, S. M. Girvin, J. P. Carini, and D. Shahar, Rev. Mod. Phys. **69**, 315 (1997).
2. D. B. Haviland, Y. Liu, and A. M. Goldman, Phys. Rev. Lett. **62**, 2180 (1989).
3. M. P. A. Fisher, Phys. Rev. Lett. **65**, 923 (1990).
4. A. F. Hebard and M. A. Paalanen, Phys. Rev. Lett. **65**, 927 (1990).
5. M. A. Paalanen, A. F. Hebard, and R. R. Ruel, Phys. Rev. Lett. **69**, 1604 (1992).
6. A. Yazdani and A. Kapitulnik, Phys. Rev. Lett. **74**, 3037 (1995).
7. S. Okuma, T. Terashima, and N. Kokubo, Solid State Commun. **106**, 529 (1998).
8. S. Tanda, S. Ohzeki, and T. Nakayama, Phys. Rev. Lett. **69**, 530 (1992).
9. F. Ichikawa, Y. Yamasaki, T. Nishizaki, *et al.*, Solid State Commun. **98**, 139 (1996).
10. V. F. Gantmakher, M. V. Golubkov, V. T. Dolgopolov, *et al.*, Pis'ma Zh. Éksp. Teor. Fiz. **68**, 337 (1998) [JETP Lett. **68**, 363 (1998)].
11. E. Abrahams, P. W. Anderson, D. C. Licciardello, and T. V. Ramakrishnan, Phys. Rev. Lett. **42**, 673 (1979).
12. J. Lages and D. L. Shepelyansky, Phys. Rev. B **64**, 094502 (2001).
13. S. Okuma, T. Terashima, and N. Kokubo, Phys. Rev. B **58**, 2816 (1998).
14. V. F. Gantmakher, M. V. Golubkov, V. T. Dolgopolov, *et al.*, Pis'ma Zh. Éksp. Teor. Fiz. **71**, 231 (2000) [JETP Lett. **71**, 160 (2000)]; Pis'ma Zh. Éksp. Teor. Fiz. **71**, 693 (2000) [JETP Lett. **71**, 473 (2000)].
15. T. B. Charikova, A. I. Ponomarev, A. N. Ignatenkov, *et al.*, Fiz. Met. Metalloved. **91** (2), 46 (2001).
16. G. I. Harus, A. I. Ignatenkov, A. I. Ponomarev, *et al.*, Pis'ma Zh. Éksp. Teor. Fiz. **70**, 93 (1999) [JETP Lett. **70**, 97 (1999)].
17. A. Kussmaul, J. S. Moodera, P. M. Tedrow, *et al.*, Physica C (Amsterdam) **177**, 415 (1991).
18. V. M. Galitski and A. I. Larkin, Phys. Rev. B **63**, 174506 (2001).
19. A. I. Larkin and D. E. Khmel'nitskiĭ, Zh. Éksp. Teor. Fiz. **83**, 1140 (1982) [Sov. Phys. JETP **56**, 647 (1982)].
20. B. Srinivasan, G. Benenti, and D. L. Shepelyansky, Phys. Rev. B **66**, 172506 (2002).

JETP Letters, Vol. 77, No. 8, 2003, pp. 429–433. Translated from Pis'ma v Zhurnal Éksperimental'noĭ i Teoreticheskoĭ Fiziki, Vol. 77, No. 8, 2003, pp. 503–508.

Orientational Defects in Freely Suspended Smectic *C* Films

P. V. Dolganov and B. M. Bolotin

Institute of Solid-State Physics, Russian Academy of Sciences, Chernogolovka, Moscow region, 142432 Russia
Institute of Chemical Reagents and Special-Purity Substances, Moscow, 107076 Russia

Received March 20, 2003

Linear orientational defects (2π and π walls) in freely suspended thin smectic *C* films exposed to a magnetic field were studied. The bend and splay elastic constants, as well as the orientational viscosity of a two-dimensional **c**-director field, were determined. It was established that a change in the polar and azimuthal angles of magnetic-field orientation in a sample cardinally transforms the wall structure. This is caused by the anisotropy of orientational elasticity of the **c** director. © *2003 MAIK "Nauka/Interperiodica"*.

PACS numbers: 61.30.Jf; 61.30.Gd; 68.55.Ln

In tilted smectic liquid-crystal films, linear and point defects are formed either spontaneously or under the action of an external field [1–6]. Freely suspended thin (2–100 molecular layers) films are suitable objects for studying these defects [7]. Such films are composed of a strictly fixed number of smectic layers parallel to the free surface. In smectic *C* (Sm*C*) liquid crystals, the average orientation of the molecular long axes (**n** director; Fig. 1a) is tilted at angle θ with the normal **z** to the smectic layer. The **n**-director projection onto the plane of a smectic layer forms a two-dimensional (2D) field of molecular orientations, which can be described by a 2D unit vector **c**(*xy*), so-called **c** director [8, 9]. The defects in the layer plane are formed due to the modulation of **c**-director orientation. Up to now, the defects were studied mostly in electric-field-oriented polar films or in nonoriented samples.

In this work, linear orientational defects were studied in freely suspended films exposed to a magnetic field. The use of a magnetic field allowed the study of nonpolar Sm*C* and observation of the linear defects (π walls) that cannot form in polar structures in an electric field. It is established that the structure of a 2π wall strongly depends on its orientation about the direction of magnetic field, owing to the anisotropy of the orientational elastic energy of the **c**-director field. The bend and splay elastic constants were determined for the **c**-director field in nonpolar Sm*C* films.

Measurements were performed on a freely suspended liquid-crystal Sm*C* 4-hexyl-4'-hexyloxy-2'-hydroxybenzalaniline films. In a bulk sample, the Sm*C* phase is observed in the temperature range from 39.8 to 80.4°C. Freely suspended films were prepared in a round hole with a diameter of 3 mm made in a thin glass plate. Immediately after the preparation, the film was inhomogeneous in thickness. On holding the sample in the Sm*C* phase for one hour, the thickness, as a rule, became homogeneous. Measurements were made on films with a strictly fixed number of smectic layers. The number of layers in the film was determined from the measured optical reflectance spectra [10]. The direction of a magnetic field about the film plane (polar angle α) could be changed by turning the sample or magnetic field in the *yz* plane (Fig. 1b). The samples were placed in a thermostatted cell. The defects were imaged in reflected polarized light using an optical microscope and a CCD chamber.

We first describe qualitatively the linear and point defects that are observed in a magnetic field (Fig. 2). In the crossed-polarizer images, the **c** director continuously turns by an angle of 90° upon passing through a light stripe; i.e., the linear defects in Figs. 2a and 2b with two and four stripes correspond to the π and 2π walls, respectively. Near the topological defects

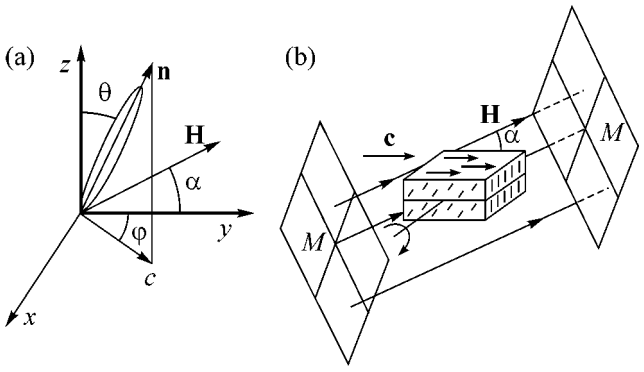

Fig. 1. (a) The **n** director in the Sm*C* structure makes the angle θ with the normal *z* to the smectic layer. The azimuthal molecular orientation in the layer plane (*xy*) is specified by the angle φ or by the orientation of **c** director. The magnetic field **H** is parallel to the *yz* plane and makes the angle α with the smectic layer. (b) The orientation of the **c** director in the field-oriented sample is shown by the arrows. The angle α could vary by the rotation of magnets (*M*) or film about the *x* axis.

0021-3640/03/7708-0429$24.00

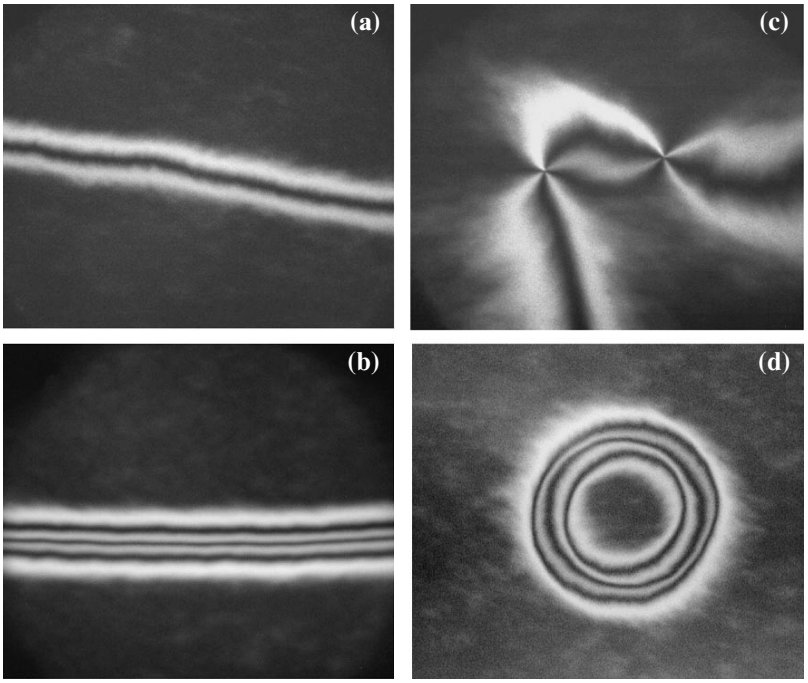

Fig. 2. (a, b, d) Disclination walls and (c) point topological defects in a magnetic field. Images were obtained in the reflected light with crossed polarizer and analyzer. Linear (a) π and (b) 2π walls are observed, respectively, for a magnetic field oriented in the film plane ($\alpha = 0$) and tilted to it ($\alpha \neq 0$). The frame horizontal size is L = 825 μm, and H = (a, b, d) 3.3 kOe. (c) The pair of point topological defects are of different sign: (left defect) +1 and (right defect) –1. H = 1.1 kOe and L = 760 μm. (d) Annihilation of a closed disclination loop.

(Fig. 2c), the orientation of $\mathbf{c}(xy) = [\sin\varphi(xy), \cos\varphi(xy)]$ changes by the angle [8, 9]

$$\oint \nabla_i \varphi dr_i = 2\pi s \tag{1}$$

upon going counter-clockwise round the defect along a closed loop, where s is the topological charge and $i = x, y$. In the Sm*C* phase, the defects with a high topological charge are energetically less favorable and dissociate into defects with unit charge. The observation of variously oriented topological defects in crossed polarizers showed that the topological charges of two topological point defects (Fig. 2c) are s = +1 (levo) and s = –1 (dextro), and the **c** director has a circular configuration in the +1 topological defect (counter-clockwise rotation). In the presence of a field, single topological defects are attracted to the film boundaries, because this minimizes the film energy. Defects with topological charges of different sign (Fig. 2c) are attracted together and annihilate, as it occurs in the absence of the field [2]. The closed linear defects shrink to a ring and also annihilate because of the linear tension (Fig. 2d). Those linear defects whose ends are anchored to the opposite film boundaries remain in the sample. One can see (Fig. 2) that both π and 2π walls can form in smectic films in a magnetic field. This differentiates the system under consideration from the others. For example, in polar smectic films, only the 2π walls can form in an electric field, and only the π walls can form in nematics in a magnetic field [8, 9].

The interaction between the orientational order and magnetic field H is described by the energy density $-1/2\chi_a(\mathbf{H} \cdot \mathbf{n})^2$, where χ_a denotes the magnetic anisotropy [8, 9]. The elastic energy of the $\mathbf{c}(x, y)$ orientation field in a thin Sm*C* film has the following form in an external magnetic field with the geometry shown in Fig. 1:

$$F = F_0 + \frac{h}{2}\int [K_s(\nabla \cdot \mathbf{c})^2 + K_b(\nabla \times \mathbf{c})^2 - \chi_a H^2 (A_1 \cos\varphi + A_2 \cos 2\varphi)]\, dxdy, \tag{2}$$

where h is the film thickness and K_s and K_b are, respectively, the 2D splay and bend elastic constants of the **c** director [11]. F_0 is the φ-independent free energy. The last two terms on the right-hand side in Eq. (2) account for the magnetic energy: $A_1 = 1/2 \sin 2\theta \sin 2\alpha$ and $A_2 = 1/2 \sin^2\theta \cos^2\alpha$, where α is the angle between the magnetic field and the film plane. The 2π periodicity of the magnetic energy for $\alpha \neq 0$ and the π periodicity for $\alpha = 0$ should give rise, respectively, to the 2π and π walls. The value of $\varphi(x, y)$ is found by minimizing free energy (2). In the general case of $K_s \neq K_b$, the solution cannot be found in the analytic form. To demonstrate the typical behavior of φ in a magnetic field, we take $K_s = K_b = K$.

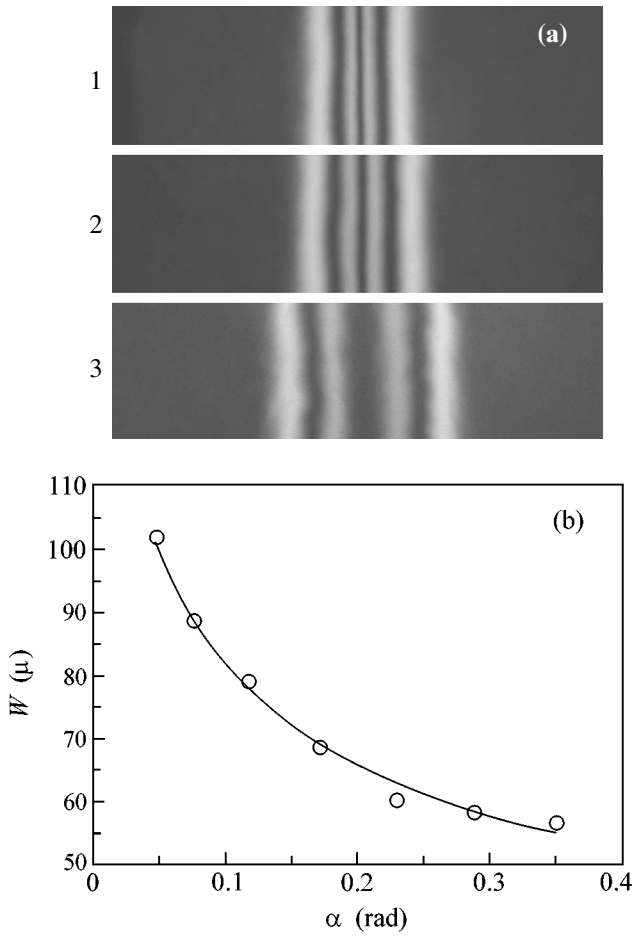

Fig. 3. (a) The form of a 2π wall for different tilts of a magnetic field to the film plane: α = (1) 1.5°, (2) 9°, and (3) 1.5°. As the tilt angle decreases, the wall broadens and forms two weakly interacting π walls. The magnetic field H = 3.3 kOe is perpendicular to the 2π wall. The frame horizontal size is 700 μm. Away from the wall, **c** is directed from left to right. The number of smectic layers N = 7, and T = 53°C. (b) Dependence of the 2π-wall halfwidth on α. N = 2.

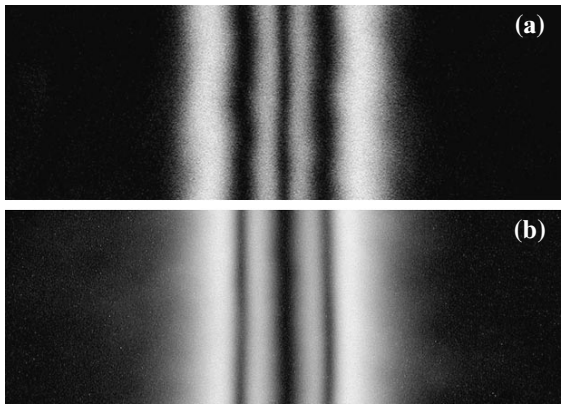

Fig. 4. The form of a 2π wall for its orientations perpendicular and parallel to $\mathbf{H}_y$. Away from the walls, **c** is directed (a) from left to right and (b) from top to bottom. In the wall center, the deformation of **c** director is bend in photograph (a) and splay in photograph (b). The separation between the central light stripes is smaller for the bend deformation ($K_b < K_s$). The situation is reversed in the center of the two side dark stripes: (a) bend and (b) spray deformations. T = 53°C, H = 3.3 kOe, and N = 4; the frame horizontal size is 480 μm.

A single-constant approximation was used earlier in the description of linear and concentric 2π solitons in polar films exposed to an external electric field [1, 12]. In contrast to the electric field, the minimization of Eq. (2) gives the spatially one-dimensional solitonic solutions of two types:

$$\varphi = \mp 2\arctan[D/\sinh(Bx/\xi)], \quad \alpha \neq 0, \qquad (3)$$

$$\varphi = \pm 2\arctan[\exp(Bx/\xi)], \quad \alpha = 0, \qquad (4)$$

where $\xi = (K/\chi_a H^2)^{1/2}$ is the magnetic coherence length, $B^2 = \sin\theta\cos\alpha\sin(\theta + \alpha)$ and $D^2 = \sin(\theta + \alpha)/\cos\theta\sin\alpha$. Expression (3) describes the 2π wall and Eq. (4) describes the π wall; x is measured from the wall center. The 2π-wall halfwidth w, i.e., the separation between the points where the direction of **c** director changes from π/2 to 3π/2, is proportional to ξ and diverges logarithmically with decreasing α:

$$w = 2\xi/B\ln(\sqrt{1 + D^2} + D). \qquad (5)$$

At $w \gg \xi$, the equation for the 2π wall in the vicinity of π/2 and 3π/2 takes the form $\varphi \approx \pm 2\arctan\{\exp[B(w/2 \pm x)/\xi]\}$, where the plus sign in the exponent is taken for $x < 0$ and the minus sign is taken for $x > 0$. From the comparison with Eq. (4), one can see that, upon broadening, the 2π wall transforms to two π walls, each remaining narrow. Such a transformation was observed in our experiments. Figure 3a presents the photographs of a 2π wall for different tilts of magnetic field. The angular dependence of the halfwidth is shown in Fig. 3b. The 2π wall broadens mainly due to its central part. At a small tilt angle, the 2π wall diverges into two weakly interacting π walls. The orientational elasticity K can be determined from the data in Fig. 3b. However, the real situation is more complicated. In the single-constant approximation, the wall structure should not depend on the azimuthal direction of magnetic field. Photographs of the 2π wall (a) for its orientation perpendicular to the magnetic field and (b) for the **H** projection $\mathbf{H}_y$ parallel to the wall are shown in Fig. 4. One can see that the wall structures are essentially different, evidencing that the ordinarily used single-constant approximation is too crude.

The necessity of taking into account the fact that the wall structures should be described by two elastic constants requires the use of a more complicated procedure for determining $\varphi(x, y)$ than was used in the literature in describing the 2π walls. The first derivatives $\varphi'_{x,y}$ were

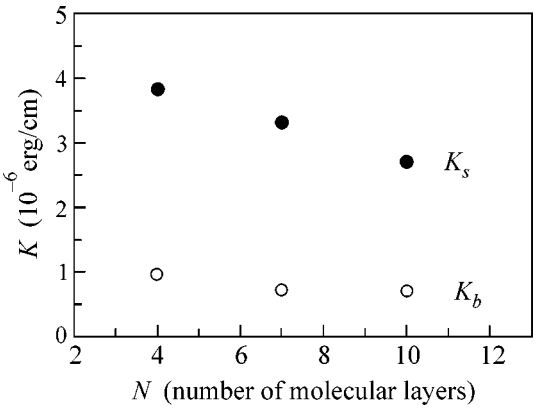

Fig. 5. Two-dimensional bend (K_b) and spray (K_s) orientational elastic constants of the **c**-director field for films of various thickness. $T = 53°C$.

found in the analytic form from the Euler equation obtained by minimizing the free energy functional (2):

$$\varphi'_{x,y} = \left[\frac{\chi_a H^2 (A_1 + A_2 - A_1\cos\varphi - A_2\cos 2\varphi)}{K_\varphi}\right]^{1/2}, \quad (6)$$

where $K_\varphi = K_s\cos^2\varphi + K_b\sin^2\varphi$ for φ'_x (the wall is parallel to **y**) and $K_\varphi = K_s\sin^2\varphi + K_b\cos^2\varphi$ for φ'_y (the wall is parallel to **x**). Expression (6) also follows from the condition for equilibrium between the elastic and magnetic density energies of a uniformly oriented film. The function $\varphi(x, y)$ can be found by numerical integration of Eq. (6). For the crossed-polarizer observations, rotations of the **c** director by $\pi/4$, $7\pi/4$ and $3\pi/4$, $5\pi/4$ correspond to two pairs of light stripes in the image of 2π wall, while rotation by $\pi/2$, $3\pi/2$ corresponds to a pair of dark stripes. The calculated and experimental positions of these stripes were compared with each other. The elastic constants K_b and K_s served as fitting parameters. The resulting orientational elastic constants are shown in Fig. 5. The magnetic anisotropy was taken to be $\chi_a = 1.2 \times 10^{-7}$ [8].

Before discussing the difference between K_s and K_b, we analyze the wall dynamics, which can be considered in the single-constant approximation for the wall motion as a whole. Expression (3) describes only a steady-state solitonic solution for $\alpha \neq 0$. Under the assumption that the relaxation dynamics of the **c** director is described by the effective viscosity coefficient γ, the equation of motion for $\varphi(x, t)$ has the form

$$\gamma\frac{\partial\varphi}{\partial t} = K\frac{\partial^2\varphi}{\partial x^2} - 1/2\chi_a H^2 (A_1\sin\varphi + 2A_2\sin 2\varphi). \quad (7)$$

In a tilted magnetic field, apart from the steady-state solution to Eq. (3), there is a self-similar solution to Eq. (7) of the form $\varphi(x, t) = u(x - vt)$ with the boundary conditions $\varphi \longrightarrow 0$ at $x \longrightarrow -\infty$ and $\varphi \longrightarrow \pi$ at $x \longrightarrow +\infty$ that describes the switching wave between the metastable ($\varphi = \pi$) and the stable ($\varphi = 0$) states: $u = 2\arctan\{\exp[B'(x - vt)/\xi]\}$, where $B' = \cos\alpha\sin\theta$, and v corresponds to the velocity of uniform motion of the switching wave (π walls),

$$v = K/(\xi\gamma)\sin\alpha\cos\theta. \quad (8)$$

The switching wave moves in the direction for which the **c**-director orientation corresponds to the minimal magnetic energy. The viscosity coefficient γ characterizes the dissipative molecular rotation that accompanies the π-wall motion. The switching wave was produced by the rotation of film about the **x** in such a way that α changes its sign. The π wall appeared near the boundary and moved through the sample. The switching-wave velocity was measured. The value of γ was determined from these data, with the effective elastic constant taken as $K \approx 1.2 \times 10^{-6}$ erg/cm. For films of different thickness, γ was on the order of 2.1×10^{-2} P. With the known γ, K_s, and K_b, the 2D orientational diffusivities were found to be [8] $D_s \approx 1 \times 10^{-4}$ cm^2/s and $D_b \approx 0.24 \times 10^{-4}$ cm^2/s. The obtained $D_{s,b}$ values are consistent with the values determined from the measurements of the orientational fluctuation dynamics in films [2].

Up to now, the 2D orientational elastic constants $K_{s,b}$ in smectic films have been determined from quasielastic light-scattering experiments. The K_b constant in nonpolar Sm*C* films was found to be $(0.4–1.4) \times 10^{-6}$ erg/cm for various substances [13], in agreement with our data obtained from the analysis of the structure of 2π walls (Fig. 5). Both 2D constants were measured in polar films [14, 15]. Their values are markedly different because of the spatial modulation of electric polarization P upon the deformation giving rise to the electric charges $\rho_p = -\nabla \cdot \mathbf{P}$ in the film. The electrostatic interaction of charges makes an additional contribution to the deformation energy and renormalizes the elastic constants. For example, according to [16], the K_b renormalization caused by the polarization charges can change the elastic modulus by an order of magnitude. The same changes in K were observed in polar films with anticlinic structure [12]. In our work, the $K_{s,b}$ measurements were carried out in a nonpolar Sm*C*, in which $K_{s,b}$ should not be renormalized due to the spontaneous polarization, so that it would be more correct to compare $K_{s,b}$ with the Frank's 3D moduli K_{11} (splay), K_{22} (twist), and K_{33} (bend) [8]. The two-dimensional elastic constants $K_{s,b}$ can be expressed through the nematic moduli as [11, 17]

$$K_s = K_{11}\sin^2\theta, \qquad K_b = K_{22}\sin^2\theta\cos^2\theta + K_{33}\sin^4\theta. \quad (9)$$

Expressions (9) are written without taking into account the layered structure of the smectic. In nematics, $K_{ii} \approx$

10^{-6} erg/cm [8], slightly underestimating the absolute values of the 2D constants. It should be noted, however, that anisotropy of the 2D elasticity can be qualitatively explained by the geometrical relations (9) and from the fact that K_{11}/K_{33} increases in liquid crystals with local smectic ordering in the nematic phase [18, 19].

The measurements performed in this study for stationary walls and walls producing switching waves have become possible due to the use of a **c**-director-orienting magnetic field and broadened the class of substances for investigation. Moreover, in contrast to an electric field used for orienting polar smectics, the orientation of the magnetic field about the field plane could be varied. This allowed us to study the orientational defects in the **c** field (2π and π walls) in nonpolar Sm*C* films and determine the 2D orientational elastic constants. It was shown that the wall structure strongly depends on the wall orientation about the unperturbed **c**-field direction and that the wall structure can be correctly described only if the anisotropy of elastic constants are taken into account.

This work was supported by the Russian Foundation for Basic Research (project no. 01-02-16507), the program "New Materials and Structures" of the Section of Physical Sciences of the Russian Academy of Sciences, and the state program "Study of Low-Dimensional and Mesoscopic Condensed Systems."

REFERENCES

1. R. Pindak, C. Y. Young, R. B. Meyer, and N. A. Clark, Phys. Rev. Lett. **45**, 1193 (1980).
2. D. H. V. Winkle and N. A. Clark, Phys. Rev. A **38**, 1573 (1988).
3. J. Pang and N. A. Clark, Phys. Rev. Lett. **73**, 2332 (1994).
4. D. R. Link, G. Natale, N. A. Clark, and J. E. Maclennan, Phys. Rev. Lett. **82**, 2508 (1999).
5. I. Kraus and R. B. Meyer, Phys. Rev. Lett. **82**, 3815 (1999).
6. R. B. Meyer and R. A. Pelkovits, Phys. Rev. E **65**, 061704 (2002).
7. P. Pieranski, L. Beliard, J.-Ph. Tournellec, *et al.*, Physica A (Amsterdam) **194**, 364 (1993).
8. P. G. de Gennes and J. Prost, *The Physics of Liquid Crystals*, 2nd ed. (Clarendon Press, Oxford, 1993; Mir, Moscow, 1982).
9. P. Chaikin and T. C. Lubenski, *Principles of Condenced Matter Physics* (Cambridge Univ. Press, Cambridge, 1995).
10. M. Born and E. Wolf, *Principles of Optics*, 2nd ed. (Pergamon, New York, 1964; Nauka, Moscow, 1973).
11. C. Y. Young, R. Pindak, N. A. Clark, and R. C. Meyer, Phys. Rev. Lett. **40**, 773 (1978).
12. D. R. Link, L. Radzihovsky, G. Natale, *et al.*, Phys. Rev. Lett. **84**, 5772 (2000).
13. M. S. Spector and J. D. Lister, Phys. Rev. E **51**, 4698 (1995).
14. C. Rosenblatt, R. Pindak, N. A. Clark, and R. Meyer, Phys. Rev. Lett. **42**, 1220 (1979).
15. S. B. Dierker and R. Pindak, Phys. Rev. Lett. **59**, 1002 (1987).
16. M.-H. Lu, K. A. Crandall, and C. Rosenblatt, Phys. Rev. Lett. **68**, 3575 (1992).
17. S. M. Amador and P. S. Pershan, Phys. Rev. A **41**, 4326 (1990).
18. M. J. Bradshaw, E. P. Raynes, I. Fedak, and A. J. Leadbetter, J. Phys. (Paris) **45**, 157 (1984).
19. N. K. Pradhan and R. Paul, Mol. Cryst. Liq. Cryst. **366**, 157 (2001).

Translated by V. Sakun

JETP Letters, Vol. 77, No. 8, 2003, pp. 434–437. Translated from Pis'ma v Zhurnal Éksperimental'noĭ i Teoreticheskoĭ Fiziki, Vol. 77, No. 8, 2003, pp. 509–512.

Effect of Long-Range Interactions on the Critical Behavior of Three-Dimensional Disordered Systems

S. V. Belim

Omsk State University, Omsk, 644077 Russia

e-mail: belim@univer.omsk.su

Received February 25, 2003

A field-theoretical description of the behavior of a disordered Ising system with long-range interactions is presented. The description is performed in the two-loop approximation in three dimensions using the Padé–Borel resummation technique. The renormalization group equations are analyzed, and the fixed points determining the critical behavior of the system are found. It is shown that the effect of frozen structural defects on a system with long-range interactions may cause a change in its critical behavior or smearing of the phase transition.

PACS numbers: 64.60.Cn; 64.60.Ak; 75.10.Hk

The effect of long-range interactions, which at long distances is described by the power law $1/r^{-D-a}$, was studied analytically in terms of ε expansion [1–3] and numerically by the Monte Carlo method [4–6] for two- and one-dimensional systems. It was found that the effect of long-range interactions on the critical behavior of Ising systems is considerable for $a < 2$. The study [7] carried out for a three-dimensional space in the two-loop approximation confirmed the prediction of ε expansion for a homogeneous system with long-range interactions.

According to the results of [8, 9], the introduction of frozen impurities into a system leads to a change in its critical behavior. In this connection, it is of interest to determine the effect of frozen structural defects on the critical behavior of a system with long-range interactions.

This paper describes the critical behavior of a three-dimensional disordered system with long-range interactions for different values of the parameter a.

The Hamiltonian of a system with long-range interactions has the form

$$H_0 = \frac{1}{2}\int d^D q(\tau_0 + q^a)S_q S_{-q} + \frac{1}{2}\int d^D q \Delta\tau_q S_q S_{-q} + u_0 \int d^D q S_{q1} S_{q2} S_{q3} S_{-q1-q2-q3}, \quad (1)$$

where S_q denotes the fluctuations of the order parameter, D is the space dimension, $\tau_0 \sim |T - T_c|$, T_c is the critical temperature, u_0 is a positive constant, and $\Delta\tau(x)$ is the random field of impurities of the random temperature type.

The critical behavior strongly depends on the parameter a, which determines the rate of interaction decrease with distance. According to [1], the effect of long-range interactions on the system behavior is considerable for $0 < a < 2$, while, for $a \geq 2$, the critical behavior is equivalent to that of a system with short-range interactions. Therefore, only the case of $0 < a < 2$ is considered below.

For a low impurity concentration, the distribution of the random field $\Delta\tau_q$ can be considered as Gaussian and described by the function

$$P[\Delta\tau] = A\exp\left[-\frac{1}{\delta_0}\int \Delta\tau_q^2 d^D q\right], \quad (2)$$

where A is the normalization factor and δ_0 is a positive constant proportional to the concentration of frozen structural defects.

Applying the replica procedure for averaging over random fields caused by the frozen structural defects, we obtain the effective Hamiltonian of the system

$$H_R = \frac{1}{2}\int d^D q(\tau_0 + q^a)\sum_{b=1}^{m} S_q^b S_{-q}^b - \frac{\delta_0}{2}\sum_{b,c=1}^{m}\int d^D q(S_{q1}^b S_{q2}^b)(S_{q3}^c S_{-q1-q2-q3}^c) + u_0\sum_{b=1}^{m}\int d^D q S_{q1}^b S_{q2}^b S_{q3}^b S_{-q1-q2-q3}^b. \quad (3)$$

The properties of the initial system can be obtained in the limit of the number of replicas (transforms) $m \longrightarrow 0$.

Applying the standard renormalization-group procedure based on the Feynman diagram technique [10] with the propagator $G(\mathbf{k}) = 1/\tau + |\mathbf{k}|^a$, we arrive at the

expressions for the functions β_u, β_δ, γ_φ, and γ_t, which determine the differential renormalization-group equation:

$$\begin{aligned}\beta_u &= -(4-D)u\Big[1-36uJ_0+24\delta J_0\\ &\quad+1728\Big(2J_1-J_0^2-\frac{2}{9}G\Big)u^2\\ &\quad-2304\Big(2J_1-J_0^2-\frac{1}{6}G\Big)u\delta+672\Big(2J_1-J_0^2-\frac{2}{3}G\Big)\delta^2\Big],\\ \beta_\delta &= -(4-D)\delta\Big[1-24uJ_0+16\delta J_0\\ &\quad+576\Big(2J_1-J_0^2-\frac{2}{3}G_1\Big)u^2\\ &\quad-1152\Big(2J_1-J_0^2-\frac{1}{3}G\Big)u\delta+352\Big(2J_1-J_0^2-\frac{1}{22}G\Big)\delta^2\Big],\end{aligned} \tag{4}$$

$$\begin{aligned}\gamma_t &= (4-D)[-12uJ_0+4\delta J_0\\ &\quad+288\Big(2J_1-J_0^2-\frac{1}{3}G\Big)u^2\\ &\quad-288\Big(2J_1-J_0^2-\frac{2}{3}G\Big)u\delta+32\Big(2J_1-J_0^2-\frac{1}{2}G\Big)\delta^2\Big],\\ \gamma_\varphi &= (4-D)64G(3u^2-3u\delta+\delta^2);\end{aligned} \tag{5}$$

$$J_1 = \int\frac{d^Dqd^Dp}{(1+|\vec{q}|^a)^2(1+|\vec{p}|^a)(1+|q^2+p^2+2\vec{p}\vec{q}|^{a/2})},$$

$$J_0 = \int\frac{d^Dq}{(1+|\vec{q}|^a)^2},$$

$$G = -\frac{\partial}{\partial|\vec{k}|^a}\times\int\frac{d^Dqd^Dp}{(1+|q^2+k^2+2\mathbf{kq}|^a)(1+|\mathbf{p}|^a)(1+|q^2+p^2+2\mathbf{pq}|^{a/2})}.$$

Let us redetermine the effective interaction vertex:

$$v_1 = \frac{u}{J_0},\quad v_2 = \frac{\delta}{J_0}. \tag{6}$$

As a result, we obtain the following expressions for the functions β, γ_φ, and γ_t:

$$\begin{aligned}\beta_1 &= -(4-D)\Big[1-36v_1+24v_2\\ &\quad+1782\Big(2\tilde{J}_1-1-\frac{2}{9}\tilde{G}\Big)v_1^2\\ &\quad-2304\Big(2\tilde{J}_1-1-\frac{1}{6}\tilde{G}\Big)v_1v_2+672\Big(2\tilde{J}_1-1-\frac{2}{3}\tilde{G}\Big)v_2^2\Big],\\ \beta_2 &= -(4-D)\delta\Big[1-24v_1+16v_2\\ &\quad+576\Big(2\tilde{J}_1-1-\frac{2}{3}\tilde{G}\Big)v_1^2\\ &\quad-1152\Big(2\tilde{J}_1-1-\frac{1}{3}\tilde{G}\Big)v_1v_2\\ &\quad+352\Big(2\tilde{J}_1-1-\frac{1}{22}\tilde{G}\Big)v_2^2\Big],\\ \gamma_t &= (4-D)\Big[-12v_1+4v_2+288\Big(2\tilde{J}_1-1-\frac{1}{3}\tilde{G}\Big)v_1^2\\ &\quad-288\Big(2\tilde{J}_1-1-\frac{2}{3}\tilde{G}\Big)v_1v_2+32\Big(2\tilde{J}_1-1-\frac{1}{2}\tilde{G}\Big)v_2^2\Big],\\ \gamma_\varphi &= (4-D)64\tilde{G}(3v_1^2-3v_1v_2+v_2^2).\end{aligned} \tag{7}$$

Such a redetermination makes sense for $a \le D/2$. In this case, J_0, J_1, and G are divergent functions. Introducing the cutoff parameter Λ and considering the ratios

Values of the fixed points and the eigenvalues of the stability matrix*

a	v_1^*	v_2^*	b_1	b_2
1.5	−0.395432	0.951135	84.530	59.517
1.6	−0.227628	0.594810	45.302	32.575
1.7	−0.045234	0.274890	13.235	3.915
1.8	0.064189	0.046878	0.626*	0.626*
1.9	0.066557	0.040818	0.559*	0.559*

* For complex eigenvalues, only their real parts are presented.

$$\frac{J_1}{J_2} = \frac{\int_0^\Lambda\int_0^\Lambda d^D q\, d^D p/((1+|\mathbf{q}|^a)^2(1+|\mathbf{p}|^a)(1+|q^2+p^2+2\mathbf{pq}|^a))}{\left[\int_0^\Lambda d^D q/(1+|\mathbf{q}|^a)^2\right]^2},$$
$$\frac{G}{J_0^2} = \frac{-\partial/(\partial|\vec{k}|^a)\int_0^\Lambda\int_0^\Lambda d^D q\, d^D p/((1+|q^2+k^2+2\vec{k}\vec{q}|^a)(1+|\vec{p}|^a)(1+|q^2+p^2+2\vec{p}\vec{q}|^a))}{\left[\int_0^\Lambda d^D q/(1+|\vec{q}|^a)^2\right]^2}, \quad (8)$$

we obtain finite expressions in the limit $\Lambda \longrightarrow \infty$.

The values of the integrals were determined numerically. For the case $a \le D/2$, a sequence of the values of J_1/J_0^2 and G/J_0^2 was constructed for different Λ and approximated to infinity.

The critical behavior is completely determined by the stable fixed points of the renormalization-group transformation. These points can be found by equating the β functions to zero:

$$\beta_1(v_1^*, v_2^*) = 0, \quad \beta_2(v_1^*, v_2^*) = 0. \quad (9)$$

The stability requirement for a fixed point reduces to the condition that the eigenvalues b_i of the matrix

$$B_{i,j} = \frac{\partial\beta_i(v_1^*, v_2^*)}{\partial v_j} \quad (10)$$

lie in the right half-plane of the complex plane.

The index ν characterizing the growth of the correlation radius in the vicinity of the critical point ($R_c \sim |T - T_c|^{-\nu}$) is obtained from the relation

$$\nu = \frac{1}{2}(1+\gamma_t)^{-1}.$$

The Fisher index η describing the behavior of the correlation function in the vicinity of the critical point in the wavevector space ($G \sim k^{2+\eta}$) is determined from the scaling function γ_φ: $\eta = \gamma_\varphi(v_1^*, v_2^*)$. The values of other critical indices can be determined from the scaling relations.

It is well known that the perturbation series expansions are asymptotic, and the interaction vertices of the order-parameter fluctuations in the fluctuation region are sufficiently large, so that Eqs. (7) apply. Therefore, to extract the desired physical information from the expressions derived above, the Padé–Borel method generalized to the many-parameter case was used. The corresponding direct and inverse Borel transformations have the form

$$f(v_1, v_2) = \sum_{i_1, i_2} c_{i_1, i_2} v_1^{i_1} v_2^{i_2} = \int_0^\infty e^{-t} F(v_1 t, v_2 t)\, dt,$$
$$F(v_1, v_2) = \sum_{i_1, i_2} \frac{c_{i_1, i_2}}{(i_1+i_2)!} v_1^{i_1} v_2^{i_2}. \quad (11)$$

For the analytic continuation of the Borel transform of a function, a series expansion in powers of the auxiliary variable θ is introduced:

$$\tilde{F}(v_1, v_2, \theta) = \sum_{k=0}^\infty \theta^k \sum_{i_i, i_2} \frac{c_{i_1, i_2}}{k!} v_1^{i_1} v_2^{i_2} \delta_{i_1+i_2, k}, \quad (12)$$

and the [L/M] Padé approximation is applied to this series at the point $\theta = 1$. This approach was proposed and tested in [11] for describing the critical behavior of systems characterized by several interaction vertices of the order-parameter fluctuations. The property (revealed in [11–14]) that the system retains its symmetry when using the Padé approximants in the variable θ is essential in the description of multivertex models.

The table shows the stable fixed points of the renormalization-group transformation and the eigenvalues of the stability matrix at a fixed point for the parameter values $1.5 \le a \le 1.9$. One can see that stable fixed points exist in the physical region ($v_1^*, v_2^* > 0$) only when the long-range interaction parameter is $a \ge 1.8$. The calculations showed that, for any $a < 1.8$, the stable points of a three-dimensional impurity system are characterized by a negative value of the vertex v_1^*.

The calculation of the critical indices gave the following values:

$$a = 1.9, \quad \nu = 0.671447, \quad \eta = 0.0344048,$$
$$a = 1.8, \quad \nu = 0.659510, \quad \eta = 0.050978. \quad (13)$$

Thus, for a three-dimensional Ising system with long-range interactions, the introduction of frozen

structural defects leads to a change in its critical behavior if the long-range interaction parameter is $a \geq 1.8$ and to smearing of the phase transition if the parameter is $a < 1.8$.

REFERENCES

1. M. E. Fisher, S.-K. Ma, and B. G. Nickel, Phys. Rev. Lett. **29**, 917 (1972).
2. J. Honkonen, J. Phys. A **23**, 825 (1990).
3. E. Luijten and H. Mebingfeld, Phys. Rev. Lett. **86**, 5305 (2001).
4. E. Bayong and H. T. Diep, Phys. Rev. B **59**, 11919 (1999).
5. E. Luijten, Phys. Rev. E **60**, 7558 (1999).
6. E. Luijten and H. W. J. Bloöte, Phys. Rev. B **56**, 8945 (1997).
7. S. V. Belim, Pis'ma Zh. Éksp. Teor. Fiz. **77**, 118 (2003) [JETP Lett. **77**, 112 (2003)].
8. I. O. Mayer, A. I. Sokolov, and B. N. Shalaev, Ferroelectrics **95**, 93 (1989).
9. I. O. Mayer, J. Phys. A **22**, 2815 (1989).
10. J. Zinn-Justin, *Quantum Field Theory and Critical Phenomena* (Clarendon Press, Oxford, 1989).
11. S. A. Antonenko and A. I. Sokolov, Phys. Rev. B **49**, 15901 (1994).
12. K. B. Varnashev and A. I. Sokolov, Fiz. Tverd. Tela (St. Petersburg) **38**, 3665 (1996) [Phys. Solid State **38**, 1996 (1996)].
13. A. I. Sokolov, K. B. Varnashev, and A. I. Mudrov, Int. J. Mod. Phys. B **12**, 1365 (1998).
14. A. I. Sokolov and K. B. Varnashev, Phys. Rev. B **59**, 8363 (1999).

Translated by E. Golyamina

JETP Letters, Vol. 77, No. 8, 2003, pp. 438–441. From Pis'ma v Zhurnal Éksperimental'noĭ i Teoreticheskoĭ Fiziki, Vol. 77, No. 8, 2003, pp. 513–516.

On the Supersymmetric Partition Function in QCD-inspired Random Matrix Models¶

Y. V. Fyodorov[1, 2] and G. Akemann[3]

[1] *Department of Mathematical Sciences, Brunel University Uxbridge, UB8 3PH, United Kingdom*

[2] *St. Petersburg Institute of Nuclear Physics, Gatchina, 188350 Russia*

[3] *Service de Physique Théorique, CEA/DSM/SPhT Unité de recherche associée au CNRS, F-91191, France*

Received March 5, 2003

We show that the expression for the supersymmetric partition function of the chiral unitary (Laguerre) ensemble conjectured recently by Splittorff and Verbaarschot [Phys. Rev. Lett. **90**, 041601 (2003)] follows from the general expression derived recently by Fyodorov and Strahov [J. Phys. A: Math. Gen. **36**, 3203 (2003)]. © *2003 MAIK "Nauka/Interperiodica".*

PACS numbers: 11.15.-q; 12.38.-t; 11.30.Pb; 11.30.Rd

A class of random matrices that has attracted considerable attention recently [1–10] is the so-called *chiral* (Gaussian) unitary ensemble (chGUE), also known as the Laguerre ensemble. The corresponding matrices are of the form $\hat{D} = \begin{pmatrix} \mathbf{0} & \hat{W} \\ \hat{W}^\dagger & \mathbf{0} \end{pmatrix}$, where $\hat{W}$ stands for a complex matrix, with $\hat{W}^\dagger$ being its Hermitian conjugate. The off-diagonal block structure is characteristic for systems with chiral symmetry. The chiral ensemble was introduced to provide a background for calculating the universal part of the microscopic level density for the Euclidian QCD Dirac operator (see [11] and references therein). Independently and simultaneously, it was realized that the same chiral ensemble describes a new group structure associated with scattering in disordered mesoscopic wires [2]. One of the main objects of interest in QCD is the so-called Euclidean partition function used to describe a system of quarks characterized by n_f flavors and quark masses m_f interacting with the Yang–Mills gauge fields. At the level of random matrix theory, the true partition function is replaced by the matrix integral

$$Z_{n_f}(\hat{M}_f) = \int \mathcal{D}\hat{W} \prod_{k=1}^{n_f} \det\{i\hat{D} + m_f^{(k)} \mathbf{1}_{2N}\} \times e^{-N\mathrm{Tr}V(\hat{W}^\dagger \hat{W})}, \quad (1)$$

where $\hat{M}_f = \mathrm{diag}(m_f^{(1)}, \ldots, m_f^{(n_f)})$ and $V(z)$ is a suitable potential. Here, the integration over complex $\hat{W}$ replaces the functional integral over gauge field configurations [11]. Then the calculation of the partition function amounts to performing the ensemble average of the product of characteristic polynomials of $i\hat{D}$ over the probability density $P(W) \propto e^{-N\mathrm{Tr}V(\hat{W}^\dagger \hat{W})}$. In the general case of nonzero topological charge $\nu > 0$, the matrices $\hat{W}$ have to be chosen rectangular of size $N \times (N + \nu)$ [11]. For simplicity, one may choose the probability distribution to be Gaussian as defined by the formula $d\mathcal{P}(W) \propto d\hat{W}\, d\hat{W}^\dagger \exp{-[N\mathrm{Tr}\, \hat{W}^\dagger\, \hat{W}]}$.

The characteristic feature of the chiral ensemble is the presence of a particular point $\lambda = 0$ in the spectrum, also called the "hard edge" [3]. The eigenvalues of chiral matrices appear in pairs $\pm\lambda_k$, $k = 1, \ldots, N$. Far from the hard edge, the statistics of eigenvalues are practically the same as for usual GUE matrices without chiral structure, but in the vicinity of the edge eigenvalues behave very differently.

Let $\mathcal{Z}_N[m]$ be the spectral determinant (characteristic polynomial of $i\hat{D}$)

$$\mathcal{Z}_N[m] = \det(m^2 \mathbf{1}_N + \hat{W}^\dagger \hat{W}), \quad (2)$$

and let us consider a more general (supersymmetric) partition function for the chGUE defined as

$$\mathcal{H}(\hat{M}_f, \hat{M}_b) = \left\langle \frac{\prod_{j=1}^{L} \mathcal{Z}_N[m_f^{(j)}]}{\prod_{j=1}^{M} \mathcal{Z}_N[m_b^{(j)}]} \right\rangle_W, \quad (3)$$

where

$$\hat{M}_f = \mathrm{diag}(m_f^{(1)}, \ldots, m_f^{(L)}),$$

¶ This article was submitted by the authors in English.

$$\hat{M}_b = \mathrm{diag}(m_b^{(1)}, \ldots, m_b^{(M)}).$$

This correlation function contains much more information on the spectra of chiral matrices than the partition function (1), since it involves both a product and ratios of the characteristic polynomials. Much effort were spent on developing methods allowing one to calculate particular cases of such a general supersymmetric partition (or correlation) function [9, 10]. In particular, the case $\nu = 0$ was completely solved in [12] by a variant of the supermatrix method [10, 13] augmented with a generalization of Itzykson–Zuber type integrals [4, 5] to integration over noncompact group manifolds. In the recent paper [14], Splittorff and Verbaarschot conjectured the result for arbitrary integer $\nu > 0$ in the microscopic (sometimes also called "chiral") large-N limit: $N \longrightarrow \infty$ such that $\hat{X}_{b,f} = 2N\hat{M}_{b,f}$ is finite. The authors of [14] used the advanced version of the replica method suggested recently by Kanzieper [15]. The final result is given in terms of a determinant containing modified Bessel functions $I_l(z)$ ("compact integrals") and their noncompact partners—Macdonald functions $K_l(z)$. The goal of the present letter is to show that the case $\nu \neq 0$ considered in [14] in fact follows from a very general expression derived in the recent paper [16]. The demonstration of this fact also provides a natural explanation of why both compact and noncompact integrals must appear on an equal basis.

The eigenvalues $x_1, \ldots, x_N$ of the $N \times N$ positive definite matrix $H = \hat{W}^\dagger \hat{W}$ are known to be distributed according to the Laguerre ensemble density function

$$\mathcal{P}(x_1, \ldots, x_N) \propto \Delta^2(\hat{X}) \prod_{i=1}^{N} w_\nu(x_i), \tag{4}$$

where $w_\nu(x) = x^\nu e^{-Nx}$ and $\Delta(\hat{X}) = \prod_{i>j}(x_i - x_j)$. Note that the spectral determinant $\mathcal{Z}_N(m) = (-1)^N \prod_{i=1}^{N} [(-m^2) - x_i]$ is just the characteristic polynomial of matrices H from the Laguerre ensemble taken at negative real values of the spectral parameter. As is proved in the paper [16], one can express the general correlation function of the characteristic polynomials for an arbitrary unitary invariant ensemble of $\beta = 2$ symmetry class in terms of a $(M + L)$-sized determinant. The main building blocks of that determinant are (monic) orthogonal polynomials $\pi_n(x) = x^n + \ldots$ satisfying

$$\int_D dx w(x) \pi_n(x) \pi_m(x) = \delta_{nm} c_n^2, \tag{5}$$

where $w(x)$ is a general weight function, c_n are normalization constants, and D is the corresponding interval of orthogonality. A novel feature revealed in [16] is that for $M > 0$ such a determinant structure contains the *Cauchy transforms* of the orthogonal polynomials

$$h_n(\epsilon) = \frac{1}{2\pi i} \int_D dx \frac{w(x)}{x - \epsilon} \pi_n(x) \tag{6}$$

alongside with the orthogonal polynomials themselves. For them to be well defined, we need to have $\mathrm{Im}(\epsilon) \neq 0$.

Actually, the partition function Eq. (3) is given by [16]

$$\mathcal{H}(\hat{M}_f, \hat{M}_b) \propto \frac{1}{\Delta(\hat{M}_b^2)\Delta(\hat{M}_f^2)} \times \det \begin{vmatrix} h_{N-M}(-[m_b^{(1)}]^2) & h_{N-M+1}(-[m_b^{(1)}]^2) & \ldots & h_{N+L-1}(-[m_b^{(1)}]^2) \\ \vdots & \vdots & & \vdots \\ h_{N-M}(-[m_b^{(M)}]^2) & h_{N-M+1}(-[m_b^{(M)}]^2) & \ldots & h_{N+L-1}(-[m_b^{(M)}]^2) \\ \pi_{N-M}(-[m_f^{(1)}]^2) & \pi_{N-M+1}(-[m_f^{(1)}]^2) & \ldots & \pi_{N+L-1}(-[m_f^{(1)}]^2) \\ \vdots & \vdots & & \vdots \\ \pi_{N-M}(-[m_f^{(L)}]^2) & \pi_{N-M+1}(-[m_f^{(L)}]^2) & \ldots & \pi_{N+L-1}(-[m_f^{(L)}]^2) \end{vmatrix}. \tag{7}$$

For the Laguerre ensemble of matrices H with positive eigenvalues $\hat{X} = \mathrm{diag}(x_1, \ldots, x_N)$, the weight function is just $w_\nu(x) = x^\nu e^{-Nx}$, the domain is $D = [0 \leq x < \infty]$, and the monic polynomials are

$$\pi_n(x) = \frac{(-1)^n}{N^n} n! L_n^\nu(xN),$$

with $L_n^\nu(xN)$ being the standard Laguerre polynomials. Here ν can be taken real valued with $\nu > -1$. To calculate the Cauchy transform Eq. (6), we exploit a well-known integral representation for the Laguerre polynomials containing the Bessel function $J_\nu(x)$:

$$\pi_n(x) = \frac{(-1)^n}{N^{n+\nu/2}} e^{Nx} x^{-\nu/2} \times \int_0^\infty dt e^{-t} t^{n+\nu/2} J_\nu(2\sqrt{Nxt}). \quad (8)$$

Let us consider, for definiteness, $\mathrm{Im}(\epsilon) > 0$ and further employ the integral representation

$$\frac{1}{x-\epsilon} = i\int_0^\infty d\tau e^{-i\tau(x-\epsilon)}. \quad (9)$$

Then, replacing $\pi_n(x)$ in (6) by (8) and $1/(x-\epsilon)$ by (9), we easily perform the integration over x first, then integrate over τ, and arrive at the following representation (cf. Eq. (8)):

$$h_n(\epsilon) = \frac{(-1)^n}{2N^{n+\nu/2}} \epsilon^{\nu/2} \int_0^\infty dt e^{-t} t^{n+\nu/2} H_\nu^{(1)}(2\sqrt{N\epsilon t}). \quad (10)$$

Here, $H_\nu^{(1)}(z)$ is the Hankel function of the first order. Being actually interested in analytically continued values of $\pi_n(x)$, $h_n(x)$ for the region $x = -m^2 < 0$, we introduce the modified Bessel and Macdonald functions according to $I_\nu(z) = e^{-i\pi\nu/2} J_\nu(iz)$ and $K_\nu(z) = (i\pi/2) e^{i\pi\nu/2} H_\nu^{(1)}(iz)$. We then have

$$\pi_n(-m^2) = \frac{(-1)^n}{N^{n+\nu/2}} e^{-Nm^2} m^{-\nu} \times \int_0^\infty dt e^{-t} t^{n+\nu/2} I_\nu(2m\sqrt{Nt}), \quad (11)$$

$$h_n(-m^2) = \frac{(-1)^n}{N^{n+\nu/2}} \frac{m^\nu}{i\pi} \int_0^\infty dt e^{-t} t^{n+\nu/2} K_\nu(2m\sqrt{Nt}). \quad (12)$$

Substituting such representations into the expression (7), it is easy to show that the right-hand side can be rewritten as the $(M+L)$-fold integral

$$\mathcal{H}(\hat{M}_f, \hat{M}_b) \propto \frac{1}{\Delta(\hat{M}_b^2)\Delta(\hat{M}_f^2)} \exp\left\{-N\sum_{j=1}^L [m_f^{(j)}]^2\right\} \times \left[\frac{\det M_b}{\det M_f}\right]^\nu \int_{t_i>0} d\hat{t} \det(\hat{t})^{N-M} \Delta(\hat{t}) \exp(-N\mathrm{Tr}\hat{t}) \times \prod_{l=1}^L [t_l^{\nu/2} I_\nu(2m_f^{(l)} N\sqrt{t_l})] \times \prod_{l=L+1}^{L+M} [t_l^{\nu/2} K_\nu(2m_b^{(l-L)} N\sqrt{t_l})]. \quad (13)$$

Here, $\hat{t} > 0$ is a diagonal matrix of the size $M+L$ with entries $t_1, \ldots, t_{M+L}$, and we rescaled $t \longrightarrow Nt$. Such an equation generalizes the integral representation (Eqs. (28), (29) from [12]) to nonzero values of ν. It is valid for any integer N, L, M. The chiral limit $N \longrightarrow \infty$ can be performed exactly along the same lines as in [12], and the result is the one conjectured by Splittorff and Verbaarschot [14, 17]:

$$\mathcal{H}(X_f, X_b) \propto \left[\frac{\det X_b}{\det X_f}\right]^\nu \frac{1}{\Delta(X_b^2)\Delta(X_f^2)} \times \det[X_i^{j-1} \mathcal{J}_{\nu+j-1}(X_i)]_{i,j=1,\ldots,M+L}. \quad (14)$$

Here, $X_f = X_{\{i=1,\ldots,L\}}$ and $X_b = X_{\{i=L+1,\ldots,L+M\}}$ denote the rescaled fermionic and bosonic masses, respectively, as well as $\mathcal{J}_i = I_i$ for $i = 1, \ldots, L$ and $\mathcal{J}_i = K_i$ for $i = L+1, \ldots, L+M$. Note that the presence of "compact" (modified Bessel) and "noncompact" (Macdonald) functions in the final expressions is a direct consequence of the presence of both orthogonal polynomials and their nonpolynomial partners (Cauchy transforms) in the determinantal representation. One may also wish to consider a more general type of potentials V in the probability density (see, e.g., [7]). The related universality questions will be addressed elsewhere [18].

Y.V.F. is grateful to Jac Verbaarschot for stimulating our interest in the problem and useful communications.

This work was supported by EPSRC (grant no. GR/R13838/01 "Random Matrices Close to Unitary or Hermitian") (Y.V.F.) and by a Heisenberg fellowship of the Deutsche Forschungsgemeinschaft (G.A.).

REFERENCES

1. E. V. Shuryak and J. J. M. Verbaarschot, Nucl. Phys. A **560**, 306 (1993); J. J. M. Verbaarschot and I. Zahed, Phys. Rev. Lett. **70**, 3852 (1993).
2. K. Slevin and T. Nagao, Phys. Rev. B **50**, 2380 (1994); A. V. Andreev, B. D. Simons, and N. Taniguchi, Nucl. Phys. B **432**, 487 (1994).
3. P. J. Forrester, Nucl. Phys. B **402**, 709 (1993); C. Tracy and H. Widom, Commun. Math. Phys. **161**, 289 (1994).
4. A. D. Jackson, M. K. Sener, and J. J. M. Verbaarschot, Phys. Lett. B **387**, 355 (1996); Nucl. Phys. B **479**, 707 (1996); Nucl. Phys. B **506**, 612 (1997).
5. T. Guhr and T. Wettig, J. Math. Phys. **37**, 6395 (1996); Nucl. Phys. B **506**, 589 (1997).
6. J. Jurkiewicz, M. A. Nowak, and I. Zahed, Nucl. Phys. B **478**, 605 (1996); Err.: Nucl. Phys. B **513**, 759 (1998); T. Wilke, T. Guhr, and T. Wettig, Phys. Rev. D **57**, 6486 (1998); R. A. Janik, M. A. Nowak, and I. Zahed, Phys. Lett. B **392**, 155 (1997).

7. G. Akemann, P. H. Damgaard, U. Magnea, and S. Nishigaki, Nucl. Phys. B **487**, 721 (1997); E. Kanzieper and V. Freilikher, Philos. Mag. B **77**, 1161 (1998); P. H. Damgaard and S. M. Nishigaki, Nucl. Phys. B **518**, 495 (1998).
8. E. Brezin and S. Hikami, Commun. Math. Phys. **214**, 111 (2000).
9. D. Dalmazi and J. J. M. Verbaarschot, Nucl. Phys. B **592**, 419 (2001).
10. Y. V. Fyodorov, Nucl. Phys. B **621**, 643 (2002).
11. J. J. M. Verbaarschot and T. Wettig, Annu. Rev. Nucl. Part. Sci. **50**, 343 (2000).
12. Y. V. Fyodorov and E. Strahov, Nucl. Phys. B **647**, 581 (2002).
13. K. B. Efetov, *Supersymmetry in Disorder and Chaos* (Cambridge Univ. Press, Cambridge, 1997).
14. K. Splittorff and J. J. M. Verbaarschot, Phys. Rev. Lett. **90**, 041601 (2003).
15. E. Kanzieper, Phys. Rev. Lett. **89**, 250201 (2002).
16. Y. V. Fyodorov and E. Strahov, J. Phys. A: Math. Gen. **36**, 3203 (2003).
17. Note that the factor $[\det X_b/\det X_f]^\nu$ is absent in the corresponding expression in [14]. Instead, it is (implicitly) included in the normalization of the probability measure of the chiral random matrix ensemble.
18. G. Akemann and Y. V. Fyodorov (under preparation).

JETP Letters, Vol. 77, No. 8, 2003, pp. 442–450. Translated from Pis'ma v Zhurnal Éksperimental'noĭ i Teoreticheskoĭ Fiziki, Vol. 77, No. 8, 2003, pp. 517–526.

Magnetic Properties of Defects in Spin-Gap Magnets

A. I. Smirnov*, V. N. Glazkov, and S. S. Sosin

Kapitza Institute for Physical Problems, Russian Academy of Sciences, ul. Kosygina 2, Moscow, 117973 Russia

** e-mail: smirnov@kapitza.ras.ru*

Received March 14, 2003

The magnetic properties of defects were studied in spin-gap magnets such as spin-Peierls magnet $CuGeO_3$, Haldane magnet $PbNi_2V_2O_8$, and charge-ordered ladder magnet NaV_2O_5. Doping of these systems with nonmagnetic impurities leads to additional magnetic degrees of freedom, which manifest themselves at low temperatures, where the intrinsic magnetic susceptibility of a spin-gap system is close to zero. Magnetic susceptibility appears due to the local destruction of the singlet ground state as a result of impurity-induced breakage of spin chains. Antiferromagnetically correlated areas arise near the spin-chain breaks. The sizes of these areas and the effective spin of these specific spin clusters are estimated. The order parameter and its spatially modulated depth are determined for impurity-induced magnetically ordered phases. The magnetic properties of defects for the NaV_2O_5 ladder structure are explained in the model of electrons "hopping" near the chain break. The hopping degree of freedom effectively influences the total spin of a spin-chain fragment and magnetization of the system. © *2003 MAIK "Nauka/Interperiodica".*

PACS numbers: 75.10.Jm; 75.60.Ch; 75.50.Ee; 75.30.-m

Chains of spins coupled by the Heisenberg antiferromagnetic exchange interaction

$$\mathcal{H} = \sum_i JS_iS_{i+1} \quad (1)$$

have been actively studied in recent years. The simple formulation of the problem and the nontrivial solution and results attract the attention of theorists. Experimentalists are interested in the realization of objects exhibiting new quantum phenomena.

The ground state of a chain of $S = 1/2$ spins arranged along a straight line with the period a is singlet and has no magnetic order; i.e., the average spin projection at each site is zero, $\langle S_i^z \rangle = 0$ [1]. The absence of the average magnetic moment at the lattice site in the ground state is a quantum effect and has no classical analogue. The dispersion law of long-wavelength excitations of such a chain is similar to the spectrum of spin waves in an ordinary antiferromagnet $\varepsilon(k) \sim |\sin(ka/2)|$. However, the velocity of excitation propagation $v = \pi Ja/2\hbar$ is higher than the velocity $v_{mf} = Ja/\hbar$ [2] calculated in the molecular-field approximation. Although long-range magnetic order is absent, the length of spin–spin correlation is infinite, because the correlation function decreases following a power law.

The properties of $S = 1$ spin chains with antiferromagnetic exchange differ even more strongly from the properties of ordered antiferromagnets. Indeed, the correlation length ξ is finite and equal to about $7a$, and the spectrum of spin excitations (triplets) is separated from the ground state (disordered and singlet) by a gap of exchange-origin (so-called Haldane gap) $\Delta \simeq 0.41J$ [3, 4].

The spectrum of spin excitations in $S = 1/2$ spin chains also has an energy gap if the exchange is alternating, i.e., if the exchange integral between neighboring ions in a chain alternately takes one of the two values $J \pm \delta$. In this case, the gap is determined by the alternating parameter, $\Delta \simeq \delta$ [5]. The appearance of a spin gap is responsible for a finite correlation length $\xi \simeq v\hbar/\Delta$.

The described spin-gap systems are realized in crystals including $S = 1$ spin chains and alternating chains of $S = 1/2$ spins. The alternation of spin chains can arise either due to the crystal structure [6] or spontaneously through so-called spin-Peierls transition occurring because the alternation (dimerization) leads to gain in the exchange energy [7, 8]. There are other disordered spin-gap systems such as ladder spin structures [9] and systems of coupled spin dimers [10]. The disordered ground state is insensitive both to weak interactions between chains and to anisotropy if the corresponding perturbation energy is low compared to the spin gap. Magnetic excitations of a spin-gap crystal are frozen out at low temperatures $T \ll \Delta/k_B$, and the system of magnetic ions becomes nonmagnetic.

The replacement of a magnetic ion by a nonmagnetic one results in the breakage of a spin chain and local disturbance of the singlet state. As a result, an area of antiferromagnetically correlated nonzero average spin projections, i.e., an area of local antiferromagnetic order, appears near an impurity (see Fig. 1). These antiferromagnetic areas will be called clusters. We empha-

size that these clusters are formed by the base-matrix spins recovered from the singlet background due to exchange interaction with an end spin. The number of magnetic ions in a cluster is equal to about ξ/a, and the absolute value of the average spin projection is maximal near the chain end and decreases with distance from the chain end. A cluster has nonzero spin and magnetic moment. The formation of clusters with local antiferromagnetic order was analyzed theoretically in [11] for a spin-Peierls magnet and in [12] for a Haldane magnetic (see Fig. 1).

Moreover, the appearance of clusters leads to an extraordinary phenomenon—stimulation of long-range antiferromagnetic order by impurities introduced in a spin-gap matrix. This effect was predicted in [13] and was then observed in a spin-Peierls magnet [14], a Haldane magnet [15], and a dimeric spin system [16]. Impurities (including nonmagnetic) induce magnetic ordering, because the wings of spin clusters overlap with each other, clusters in neighboring chains correlate due to weak interaction between chains, and the antiferromagnetic order extends over the whole sample. In this case, the order parameter is strongly inhomogeneous.

In this paper, experiments on studying clusters and the impurity-induced magnetic order in spin-gap systems are reviewed. The size of clusters, as well as the average order parameter and its modulation depth in an impurity-induced ordered phase, are estimated by analyzing magnetic resonance spectra. "Hopping defects" in a spin-gap magnet with a charge degree of freedom will be described at the end of the review.

1. Magnetic resonance of spin clusters and triplet excitations in a spin-Peierls magnet. A suitable object for studying defects in a spin-gap matrix is the inorganic spin-Peierls magnet $CuGeO_3$, where the temperature of the spin-Peierls transition is $T_{SP} = 14.5$ K and the spin gap at low temperatures $\Delta(0) \simeq 25$ K [7].

The spin gap is opened at temperature T_{SP} and is close to its maximum value $\Delta(0)$ below 7 K. Samples are grown as perfect single crystals, and the magnetic Cu^{2+} ($S = 1/2$) ions can be replaced by, e.g., nonmagnetic ions (Zn, Mg) or magnetic Ni ($S = 1$) ions. These impurities occupy the sites of Cu^{2+} ions in the $CuGeO_3$ lattice. In this case, the solubility limit exceeds 6%. Thus, a controlled number of the breaks of dimerized chains can be introduced by doping with zinc or magnesium. When doping with nickel, the spatially uniform singlet state is disturbed so that two fragments of the chain are coupled through a nickel magnetic ion, and the impurity ion is located at the center of a cluster. The contributions of the defects of spin-gap systems to susceptibility and to the magnetic resonance signals are clearly seen against the background of a singlet and nonmagnetic matrix. In pure $CuGeO_3$ crystals, the low-frequency magnetic resonance [$f \ll \Delta(0)$] at temperatures below T_{SP} is caused by the transitions between the spin sublevels of triplet excitations. Its intensity

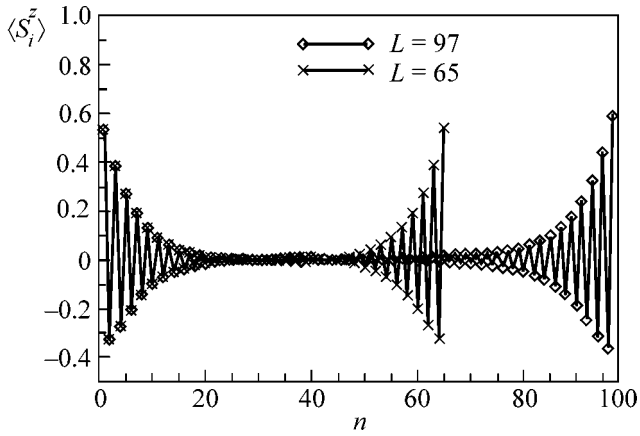

Fig. 1. Spin structure of a fragment of a Haldane spin chain for an odd number of spins and total projection $S^z_{tot} = 1$, where n is the site number. The figure is taken from [12].

decreases with decreasing temperature because of excitation freezing out. The resonance field virtually does not change with temperature and corresponds to the g factor $g_{Cu} \simeq 2.1$ characteristic of the Cu ions [17]. In doped samples, a strong magnetic resonance signal due to the defect spins appears at low temperatures. The dimerized phase in nickel-doped crystals, in contrast to crystals doped with other elements, exhibits an anomalous temperature dependence of the g factor. At $T < T_{SP}$, the effective g factor decreases and reaches an anomalously small value of 1.4 at low temperatures and $\mathbf{H} \parallel c$ [18]. This g-factor value differs strongly from the value characteristic for nickel and copper ions. The anomaly in the g factor is associated with the Dzyaloshinskii–Moriya interaction near a defect and the multispin nature of a cluster. Indeed, the Dzyaloshinskii–Moriya interaction in a system including more than two spins gives rise to a strong anisotropy of the effective g factor and reduces its value [19]. Calculations with a model with six spins show that the Dzyaloshinskii–Moriya interaction with an energy of 30% of the exchange energy in a chain suffices to explain $g_c = 1.4$ [18].

The anomaly in the g factor makes it possible to reliably distinguish the magnetic resonance signals of defects formed due to the inclusion of nickel ions from a signal of the base matrix. High-quality $Cu_{(1-x)}Ni_xGeO_3$ samples, where signals from individual clusters at low concentrations are not smeared by the interaction with residual defects, were studied in [20]. Figures 2 and 3 show the EPR line shape for samples with $x = 0.002$ and 0.008. The EPR intensity decreases at $T < T_{SP}$, because triplet excitations become frozen. The position of the line varies smoothly with temperature. Figure 4 shows the temperature dependence of the g factor. Variation of the g factor reflects the continuous transition of magnetic resonance from the resonance frequency of triplet excitations to the res-

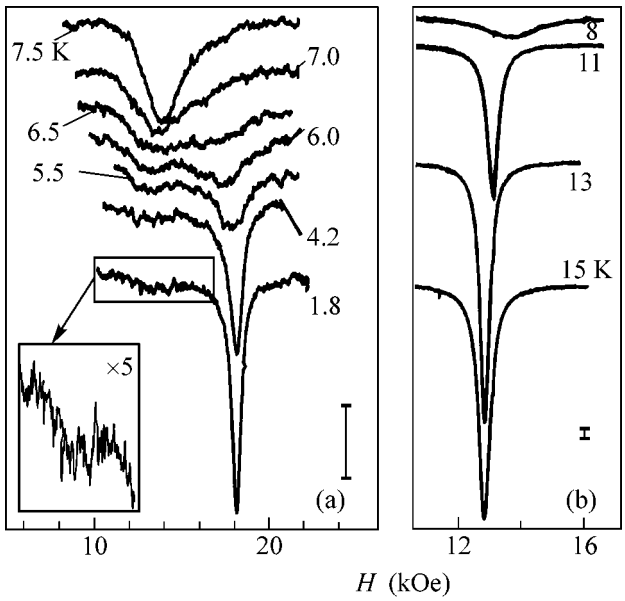

Fig. 2. Resonance absorption line shape of a $Cu_{0.998}Ni_{0.002}GeO_3$ sample at various temperatures [20], $f = 36$ GHz, **H** || *c*. Vertical intervals in (a) and (b) correspond to the same absorption.

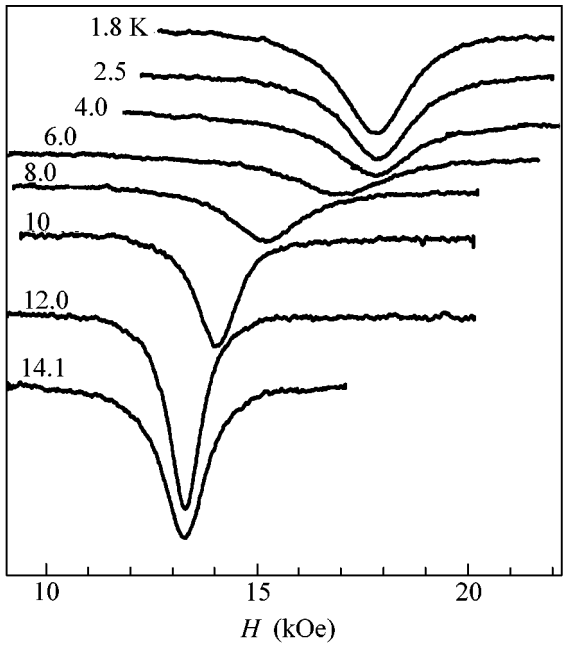

Fig. 3. Same as in Fig. 2, but for a $Cu_{0.992}Ni_{0.008}GeO_3$ sample.

onance frequency of spin clusters. Smooth variation in the resonance field means that the indicated spin oscillation modes affect each other due to the exchange interaction between the excitations and clusters. In a sample with low impurity concentration, the EPR line is split into two components corresponding to the residual triplet excitations and the resonance of individual clusters.

The magnetic resonance frequencies in the presence of the exchange interaction between two spin subsystems can be described in the theory of the EPR line exchange narrowing [21]. In the presence of the exchange interaction between two spin systems, one can observe either two resonance lines or a single common line (if the exchange-hopping frequency is, respectively, lower or higher than the difference in the frequencies of spin precession in the two subsystems). The resonance line frequencies and widths depend on the strength of exchange interaction between the subsystems and their susceptibilities. In particular, the center of gravity of the magnetic-resonance spectrum (and resonance frequency if exchange is fast) is determined by the resonance frequencies of each subsystem, which are taken with weights proportional to susceptibility. In our case, there are xN_A clusters per one mole of the substance, and their susceptibility, without regard for the interaction with triplets, obeys the Curie law. The number and susceptibility of triplet excitations are calculated using values known for a pure crystal, with allowance made for the fact that excitations can be located in chain areas free of clusters; i.e., the sample volume fraction accessible to them is $(1 - xL/a)$, where L is the cluster effective size. The susceptibilities of triplets and clusters, with allowance for interaction between them, are determined in molecular-field theory. The model involves three parameters determined by fitting the $g_\alpha(T)$ functions to the experimental curves. These parameters are the effective exchange integral of cluster–triplet interaction $J_{\text{eff}} = 13 \pm 1$ K, the cluster size $L = (32 \pm 2)a$, and the effective exchange frequency $\Omega_e = (2.2 \pm 0.3) \times 10^{12}$ s^{-1}. Figure 4 shows the results of fitting. To test the model, the temperature dependence of the line width is calculated by using these three parameters (see Fig. 5). For concentration $x = 0.2\%$, the calculations agree well with experimental data. For higher concentrations, there is a qualitative agreement, and small discrepancy is attributed to the interaction between clusters. The Ω_e parameter is of the same origin as J_{eff} and determines the frequency of exchange hopping in the presence of triplet excitation at the lattice site nearest to the cluster. The relation $\hbar\Omega_e \sim J_{\text{eff}}$ between these parameters agrees with this circumstance.

Thus, the observation of cluster magnetic resonance gives an estimate of $30a$ for the size of a spin cluster. The study of magnetic resonance in a temperature range where a sufficient number of triplet excitations exist allows the conclusion to be drawn that a unified collective spin resonance mode is formed in the presence of interaction with clusters. Such a behavior indicates that the propagating triplet excitations do not destroy the cluster structure upon collisions with the ends of broken chains (otherwise, their spin-precession

mode would disappear). The cluster size can be estimated more roughly by using the differences between the EPR line widths and positions in samples with x = 0.002 and 0.008. It is reasonable to attribute these differences to the interaction between clusters, which occurs due to the overlap of cluster wings. Clusters contact each other in chain fragments with a length on the order of L (we suppose that the number of cluster spins on each side of a nickel atom is $L/2a$). The fraction of such chains is approximately equal to xL/a. Thus, we conclude that the edges of an appreciable fraction of clusters in the case x = 0.01 contact each other at $L \approx 50a$.

2. Magnetic resonance in a Haldane magnet with defects. The problem of the effective spin arising due to the breakage of a chain is of considerable interest for a Haldane magnet. There is a hypothesis that the $S = 1/2$ effective spin arises near the break of the chain [22]. This hypothesis is clearly illustrated and corroborated by numerical simulation [12] (Fig. 1). Nonzero average spin projections in a fragment of the $S = 1$ spin chain are concentrated near the ends of the fragment, and the spin projections near the end are virtually independent of the state of the other end of the fragment (for a sufficiently long chain). The sum of spin projections near the fragment end is equal to 1/2. Far from the fragment ends, the average spin projection is zero. The exact diagonalization of Hamiltonian (1) for an $S = 1$ spin chain [23] shows that sufficiently long fragments of spin chains have two closely spaced energy levels, one of which is singlet and the other is triplet. These levels are exponentially close to each other in the parameter ξ/l, where l is the fragment length. Thus, a long fragment of the $S = 1$ spin chain is equivalent to two degrees of freedom with spin $S = 1/2$, regarding both the magnetic moment and the degeneracy order. The magnetic resonance spectrum depends substantially on the effective spin of a magnetic object, because the crystal field splits energy levels for $S = 1$ and does not split levels for $S = 1/2$ (see, e.g., [24]). Therefore, the observation of magnetic resonance for the free ends of Haldane chains is of considerable interest for determining the effective spin of the chain end. Magnetic resonance of the ends of broken Haldane chains was first observed for a weak substitution of Cu^{2+} ions for the Ni^{2+} ions in the $[Ni(C_2H_8N_2)_2(NO_2)]ClO_4$ organic compound (NENP) [22]. The measured spectra were interpreted using the model of three coupled spins: two spins at the chain ends and the impurity-ion spin. The magnetic resonance study of a diamagnetically diluted Haldane magnet $PbNi_2V_2O_8$ [25] allows one to observe a signal from the free ends of spin chains and reveal the effects of interaction between the chain ends in the concentration dependence of line shape. Figure 6 shows the magnetic resonance lines for a ceramic sample of the Haldane magnet $PbNi_2V_2O_8$, where some magnetic Ni^{2+} ions are replaced by nonmagnetic Mg^{2+} ions. As is seen, doping with nonmagnetic ions increases the magnetic resonance intensity.

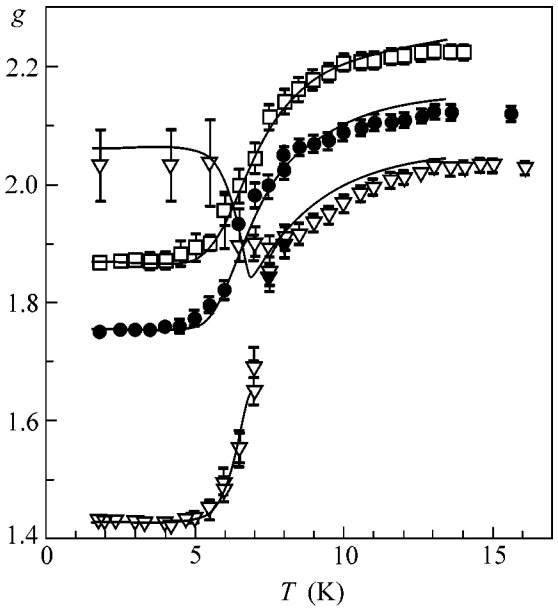

Fig. 4. Temperature dependence of the g factor for a $Cu_{0.998}Ni_{0.002}GeO_3$ sample [20]. Circles, squares, and triangles are for $\mathbf{H} \parallel a$, $\mathbf{H} \parallel b$, and $\mathbf{H} \parallel c$, respectively. Lines are calculations in the exchange-narrowing model.

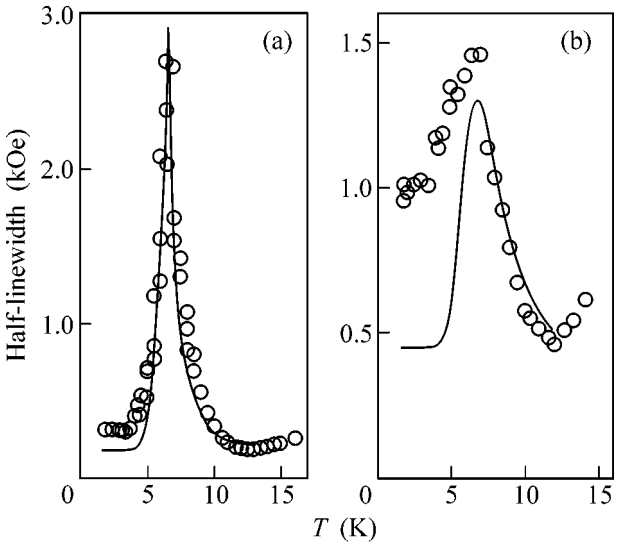

Fig. 5. Temperature dependence of the EPR line width for $CuGeO_3$ samples for x = (a) 0.2 and (b) 0.8%. Lines are for the calculations in [20].

The magnetic-field dependence of the EPR frequency can be obtained by measuring such spectra in the 9–110 GHz frequency range. This dependence is shown by closed points in Fig. 7. Within a high accuracy, the resonance frequency is a linear function of the

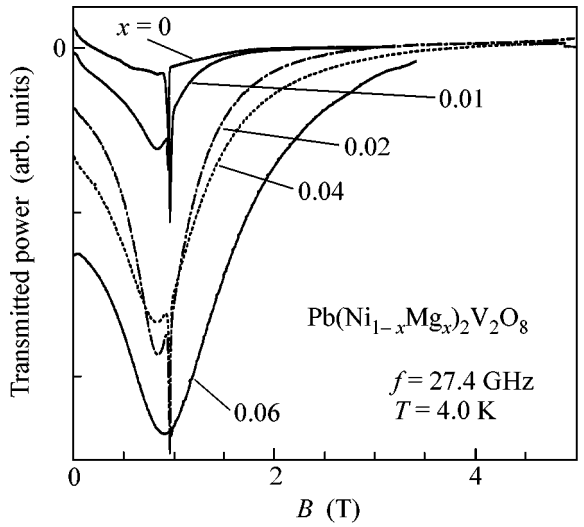

Fig. 6. Unit-mass-normalized magnetic resonance lines for a diluted Haldane magnet [25]. The narrow line for B = 0.98 T is the reference point from the diphenyl-picryl-hydrazine: g = 2.0.

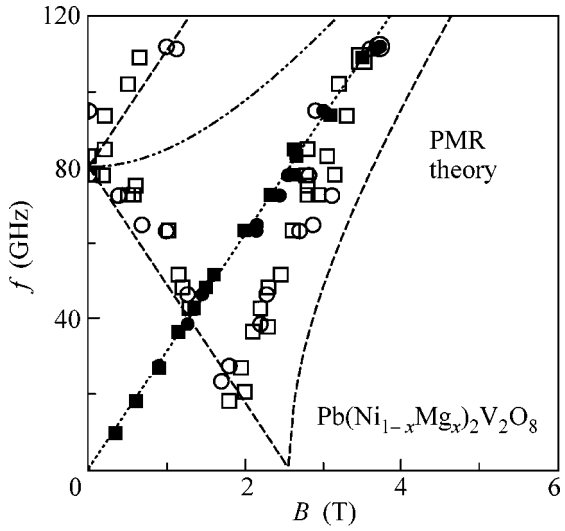

Fig. 7. Resonance frequency vs. magnetic field in $Pb(Ni_{(1-x)}Mg_x)_2V_2O_8$ ceramic samples in the (T = 5 K, closed points) paramagnetic phase and (T = 1.3 K, open points) ordered phase [25]. Circles and squares correspond to x = 0.04 and 0.06, respectively.

field. This function passes through the coordinate origin. Thus, these data testify to the absence of splitting wider than 0.5 GHz. In the presence of crystal-field splitting, resonance lines of a ceramic sample would transform into the extended absorption bands. The crystal-field splitting of the EPR spectrum of an individual spin S = 1 is determined by the spin-Hamiltonian term $D(S_i^z)^2$, where D is the single-ion anisotropy constant. The splitting width can be estimated by using the value D = –0.23 meV, determined from the spectrum of magnetic excitations measured in neutron scattering experiments [26]. The above single-ion anisotropy constant corresponds to the 56-GHz splitting of paramagnetic resonance. In the presence of such spitting, an exceedingly broad absorption band would be observed in the ceramic sample, which is inconsistent with the observed resonance lines shown in Fig. 6. Thus, the EPR spectrum suggests that the effective S = 1/2 spins appear at the ends of broken spin chains in $PbNi_2V_2O_8$. These data also testify to the significant broadening of the line with increasing concentration of defects; the line for x = 0.02 is 0.5 T broader than for x = 0.01. Such a significant line broadening cannot be attributed to the dipole–dipole interaction (the corresponding local fields are on the order of 0.01 T). Taking into account that magnetic defects involve many spins, this line broadening can be attributed to a contact between clusters, as was described in Section 1. However, we take into account that, in the case of nonmagnetic doping, independent clusters are located on different sides of an impurity atom and that clusters contact each other in $2L$-long fragments. Therefore, the size of a cluster in $Pb(Ni_{(1-x)}Mg_x)_2V_2O_8$ is estimated at $L \sim 10a$. This estimate agrees well with the theoretical value of spin–spin correlation length ξ in a Haldane magnet.

3. Defect-induced magnetic order. With lowering temperature, the doped samples undergo transition to the antiferromagnetic state. Since the ordering is due to the overlap of the cluster wings, the order parameter is strongly inhomogeneous. To characterize this exotic state, it is necessary to determine the average value and the modulation depth of the order parameter.

On cooling the $Pb(Ni_{(1-x)}Mg_x)_2V_2O_8$ samples below the Néel temperature T_N ($T_{N_{max}}$ = 3.4 K for x = 0.04), the magnetic resonance absorption line transforms to an absorption band that is characteristic of a powder antiferromagnetic sample (variation in the line shape for various frequencies was given in [25]). The edges of this band correspond to the AFMR frequencies for rational directions of a magnetic field. From the magnetic fields, for which the absorption band edges were observed, the AFMR frequency spectrum was determined for various magnetic-field directions about the crystallographic axes. The magnetic-field dependence of the AFMR frequencies is shown in Fig. 7. It qualitatively corresponds to the spectrum of resonance frequencies for an antiferromagnet with easy-axis anisotropy. In particular, these data enable one to determine the gap in the magnetic resonance spectrum $\omega_0/2\pi$ = 80 GHz. In the molecular-field approximation, the gap is determined by the average order parameter $\overline{|\langle S_i^z \rangle|}$

(averaging over time and lattice sites) and the anisotropy and exchange constants:

$$\hbar\omega_0 = 4\sqrt{|D|J}\overline{|\langle S_i^z\rangle|}. \quad (2)$$

Using the values J = 9 meV and D = –0.23 meV obtained in the inelastic neutron scattering experiments [26], we obtain the estimate $|\langle S_i^z\rangle| \simeq 0.06$. This value corresponds to the maximum value of the average order parameter, which is reached at $x = 0.04$.

4. Microscopic separation of phases in the presence of impurity-induced antiferromagnetic ordering. When the phase transition to the antiferromagnetic state occurs, the magnetic resonance signal usually transforms from the EPR signal to the AFMR signal. The EPR frequency is determined by the properties of individual magnetic ions, and the AFMR frequency is determined by the oscillations of the order parameter. Thus, the phase transition to an ordered state is accompanied by the rearrangement of magnetic resonance spectrum. The observation of this rearrangement makes it possible to determine the transition temperature and other characteristics of the phase transition. In the above-described experiments with a sufficiently high impurity concentration (above 3%), impurity ions are closely spaced, at distances on the order of the correlation length ξ. For such concentrations, the transition to the antiferromagnetic state is similar to the phase transition in ordinary three-dimensional antiferromagnets. Of particular interest are low concentrations, for which the spacing between impurity atoms in chains exceeds the length ξ, and spin clusters are separated by the residuals of singlet matrix. For $Pb(Ni_{(1-x)}Mg_x)_2V_2O_8$ samples with $x < 0.03$, the EPR line is retained down to low temperatures, in contrast to samples with $x > 0.03$. Thus, magnetic resonances of two types coexist at low temperatures.

This coexistence of two resonances can be studied more comprehensively with $Cu_{(1-x)}Mg_xGeO_3$ single-crystal samples, where the uniform impurity distribution over the sample and the impurity content were specially controlled. The impurity density distribution over a sample is uniform within an accuracy of 10^{-3}. Figure 8 shows the variation of the magnetic resonance spectrum upon the transition through the Néel point in a doped spin-Peierls magnet $Cu_{(1-x)}Mg_xGeO_3$ with x = 0.017. As is seen, the EPR line is split into two lines with a decrease in temperature. One component corresponds to the paramagnetic resonance; i.e., the resonance field is independent of temperature and coincides with the resonance field of the paramagnetic phase. The position of the second spectral component depends on temperature, and the field dependence of the frequency (see [27]) corresponds to the spectrum of a double-axis antiferromagnet. There is a wide temperature range where two lines—AFMR and EPR—are simultaneously observed. The uniform impurity distribution over the sample and the narrow temperature range of transition (0.1 K) rule out the explanation of the coexistence of two magnetic resonance lines by the macroscopic inhomogeneity of the sample. The coexistence of two resonance modes in the sample cannot be interpreted in the framework of a single phase, because order parameter oscillations in the antiferromagnetic phase exclude the paramagnetic resonance mode, while the paramagnetic phase does not allow the line splitting. The coexistence of two resonance modes can possibly be explained by a microscopic phase separation of the sample into paramagnetic and antiferromagnetic areas. Indeed, let us consider spin clusters that are formed around the impurity atoms and suppose that the coherent antiferromagnetic order exists in an area of size L^* satisfying the relation

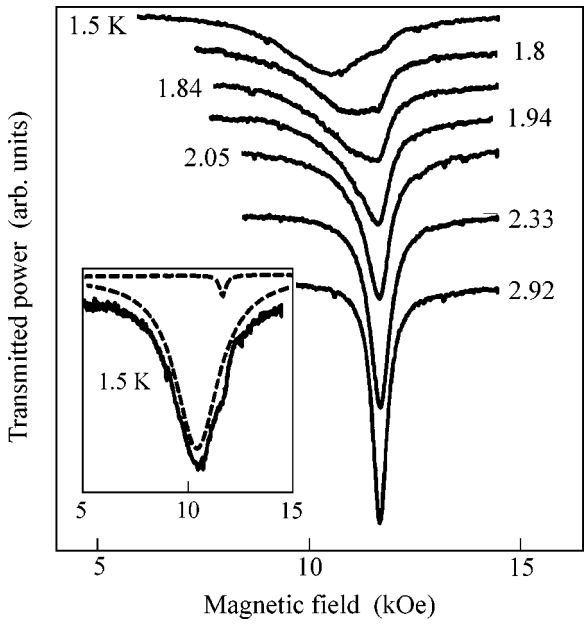

Fig. 8. Magnetic resonance line shape near the Néel point in a $Cu_{0.983}Mg_{0.017}GeO_3$ single crystal [27] for **H** ∥ *b*, f = 36 GHz, and T_N = 2.25 K.

$$k_BT = JS^2\exp\{-2L^*/\xi\}. \quad (3)$$

At distances larger than L^*, antiferromagnetic correlations are destroyed by thermal fluctuations. In the transverse directions, antiferromagnetic correlations propagate to distances that are determined by the exchange integrals in the corresponding directions. Thus, we arrive at a simplified model [27], where an elliptic antiferromagnetic area exists near each impurity center. The ellipse length along the chains is determined by Eq. (3). The transverse length decreases according to the ratio of exchange integrals. For high temperature, the areas of local antiferromagnetic order are small and do not contact each other, the order parameters in them do not correlate, and the long-range order is absent. In this case, each cluster contributes to

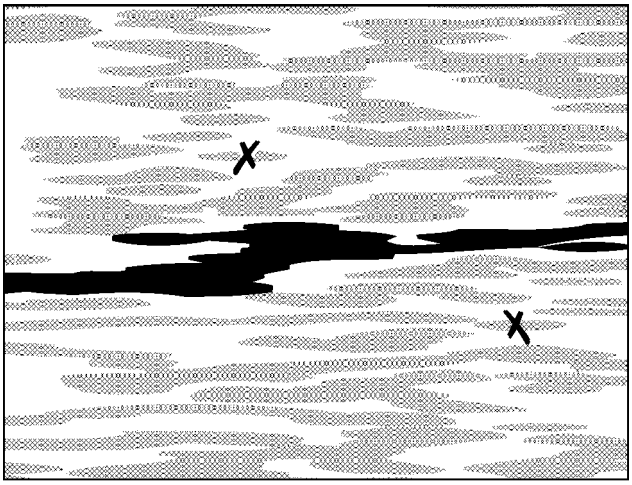

Fig. 9. Simplified simulation of the structure of impurity-induced ordered phase [27]; areas with local antiferromagnetic order are gray (the largest area is black), disordered areas are white, and crosses are for two individual clusters.

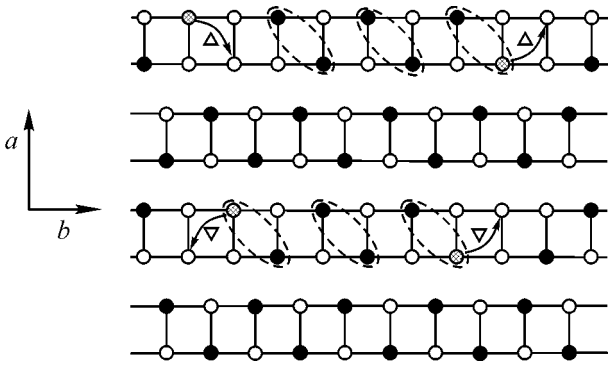

Fig. 10. Zigzag spin chains in ladders of exchange-coupled vanadium ions in the V–O layers of NaV_2O_5 crystals [32]. Solid lines are exchange interactions between vanadium ions, closed circles are V^{4+} magnetic ions, open circles are nonmagnetic V^{5+} ions, gray circles are vanadium ions with hopping electrons, triangles are sodium vacancies (above or below the V–O layer). Arrows indicate the possible electron jumps changing the parity of fragments. The dashed ovals denote dimerization (alternation) of chains.

the sample susceptibility and magnetic resonance signal, in accordance with the total magnetic moment of the cluster. Therefore, the susceptibility and magnetic resonance spectrum have a paramagnetic character. As the temperature decreases, clusters grow, and some of them begin to contact each other and form more extended areas with a coherent antiferromagnetic order covering several impurity atoms. Finally, an area of antiferromagnetic order "percolating" through the whole sample arises, as shown in Fig. 9. The appearance of such an area corresponds to the percolation threshold in the percolation problem for interpenetrating spheres [28]. At this L^* value and in its vicinity, there are single clusters in the sample (see Fig. 9), which have nonzero magnetic moments and are isolated from large antiferromagnetic areas by a weakly perturbed singlet matrix. The free spins of these clusters continue to give EPR signals, as also above the transition point. Thus, there are three types of areas below the Néel point: (i) sufficiently large areas with local antiferromagnetic order that are responsible for the AFMR signals, (ii) singlet-matrix areas that show no magnetic response, and (iii) single clusters separated from the antiferromagnetic areas by the singlet matrix.

This picture of microscopic phase separation is consistent with the two-dimensional numerical Monte Carlo simulation for the ground state of spin-Peierls and doped Haldane systems [29]. In that work, a weak interaction between chains was taken into account and it was shown that antiferromagnetically correlated nonzero spin projections (peaks of local order parameter) exist near the spin vacancies, and the space between the peaks is filled with a slightly perturbed singlet matrix. It is substantial that simulation [29] demonstrated a strong (almost 100%) modulation of the order parameter. Assuming that the vanishingly small order parameter in the areas between impurities is destroyed by thermal fluctuations at nonzero temperatures, we conclude that the structure obtained in [29] is equivalent to the structure suggested above on the basis of the two coexisting magnetic resonance signals.

5. Hopping defects in NaV_2O_5 crystals. Magnetic moments in the NaV_2O_5 compound are carried by vanadium ions, whose chains are arranged along the *b* axis of the orthorhombic structure. As is seen from the valence counting, one *d* electron is shared by two vanadium ions. Detailed structural studies show that the structure, in which all vanadium ions have the same average charge of +4.5 and *d* electrons (and spins) are located at the V–O–V molecular orbitals, is realized in the high-temperature phase ($T > 35$ K) [30, 31]. In other words, one electron is equally shared by two vanadium ions from neighboring chains and is localized at a "step" of the ladder structure consisting of vanadium-ion chains. The spins of these electrons form one-dimensional spin chains. At a temperature of 35 K, the charge ordering occurs; electrons are partially localized at the ends of ladder steps and form zigzag chains [31], as is shown in Fig. 10. The electron-density redistribution results in the exchange alternation and appearance of a spin gap $\Delta(0) = 90$ K. Due to the electron deficiency in the V–O layers of $Na_{1-x}V_2O_5$ crystals, some of the ladder steps are empty (see Fig. 10). These empty steps represent breaks of the dimerized $S = 1/2$ spin chains and are responsible for a strong increase in magnetic susceptibility in the temperature range where stoichiometric crystals are virtually nonmagnetic because of the opening of the spin gap. However, this case dif-

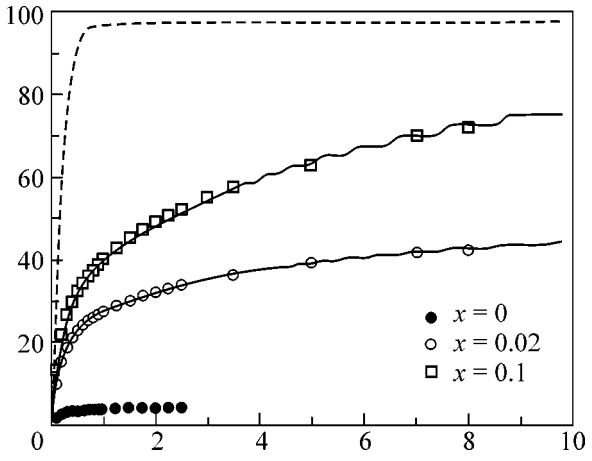

Fig. 11. Magnetization curves for $Na_{1-x}V_2O_5$ samples at a temperature of 77 mK [32]. The dashed line is the paramagnetic saturation curve for a sample with the free-spin concentration $x/2$ (half fragments are odd) for $x = 0.02$. The solid lines are calculations including the change in the parity of fragments in the presence of a magnetic field.

fers from the ordinary breaks described above, because electrons near the sodium vacancy can change their positions and be located either to the right or to the left of the defect.

We believe that this hopping degree of freedom is responsible for the unusual magnetization curves obtained at low temperature [32]. Figure 11 demonstrates that the magnetic moment associated with the defects in the spin-gap system is not saturated in fields up to 8 T, while the paramagnetic saturation field for $S = 1/2$ spins is equal to 0.5 T at the experimental temperature of 77 mK. Such a behavior of magnetization can be explained by taking into account the balance of the exchange and Zeeman energies. Analysis of the exchange energy of an $S = 1/2$ spin-chain fragment [33] shows that energy per one spin for fragments including an even number of spins is lower than for the fragments with an odd number of spins. One-step hopping of an electron change the parity of the number of spins in the chain fragment. Therefore, electron hopping in a sample with sodium deficiency in the low-temperature phase must lead to the prevalence of "even" chain fragments, despite the fact that sodium vacancies are distributed chaotically. The state of even fragments is singlet, and they do not contribute to magnetization. However, in a strong magnetic field, owing to the gain in Zeeman energy in odd fragments, electron hopping will lead to a predominance of the odd fragments. Thus, the magnetization process depends on a change in the number of even fragments. The magnetization curves calculated in the model [32], which takes into account the difference between the exchange energies of even and odd fragments and the random potential providing a feeding concentration of odd fragments, are also shown in Fig. 11.

We are grateful to L.N. Dem'yanets and A.Ya. Shapiro for the preparation of $Pb(Ni_{(1-x)}Mg_x)_2V_2O_8$ samples; H.-A. Krug von Nidda for numerous discussions; T. Masuda and K. Uchinokura, who placed $Cu_{1-x}Mg_xGeO_3$ samples at our disposal and discussed the results; M. Isobe and Y. Ueda for placing $Na_{(1-x)}V_2O_5$ samples at our disposal; G. Dhalenne and A. Revcolevschi for placing $Cu_{1-x}Ni_xGeO_3$ samples at our disposal; and C. Paulsen for magnetic measurements at ultralow temperatures. This work was supported by the Russian Foundation for Basic Research (project no. 00-02-17317), Deutsche Forschungsgemeinschaft (joint grant with RFBR no. 01-02-40007), the U.S. Civilian Research and Development Foundation for the Independent States of the Former Soviet Union (grant no. RP1-2097), and INTAS (grant no. 99-0155).

REFERENCES

1. H. Bethe, Z. Phys. **71**, 205 (1931).
2. J. des Cloizeaux and J. J. Pearson, Phys. Rev. **128**, 2131 (1962).
3. F. D. M. Haldane, Phys. Rev. Lett. **50**, 1153 (1983).
4. S. V. Meshkov, Phys. Rev. B **48**, 6167 (1993).
5. L. N. Bulaevskiĭ, Fiz. Tverd. Tela (Leningrad) **11**, 1132 (1969) [Sov. Phys. Solid State **11**, 921 (1969)].
6. A. W. Garrett, S. E. Nagler, D. A. Tennant, *et al.*, Phys. Rev. Lett. **79**, 745 (1997).
7. M. Hase, I. Terasaki, and K. Uchinokura, Phys. Rev. Lett. **70**, 3651 (1993).
8. E. Pytte, Phys. Rev. B **10**, 4637 (1974).
9. E. Dagotto and T. M. Rice, Science **271**, 618 (1996).
10. H. Kageyama, K. Yoshimura, R. Stern, *et al.*, Phys. Rev. Lett. **82**, 3168 (1999).
11. H. Fukuyama, T. Tanimoto, and M. Saito, J. Phys. Soc. Jpn. **65**, 1182 (1996).
12. S. Miyashita and S. Yamamoto, Phys. Rev. B **48**, 913 (1993).
13. E. F. Shender and S. A. Kivelson, Phys. Rev. Lett. **66**, 2384 (1991).
14. L. P. Regnault, J. P. Renard, G. Dhalenne, and A. Revcolevschi, Europhys. Lett. **32**, 579 (1995).
15. Y. Uchiyama, Y. Sasago, I. Tsukada, *et al.*, Phys. Rev. Lett. **83**, 632 (1999).
16. A. Oosawa, T. Ono, and H. Tanaka, Phys. Rev. B **66**, 020405 (2002).
17. M. Honda, T. Shibata, K. Kindo, *et al.*, J. Phys. Soc. Jpn. **65**, 691 (1996).
18. V. N. Glazkov, A. I. Smirnov, O. A. Petrenko, *et al.*, J. Phys.: Condens. Matter **10**, 7879 (1998).
19. M. I. Belinskiĭ, B. S. Tsukerblat, and A. V. Ablov, Fiz. Tverd. Tela (Leningrad) **16**, 989 (1974) [Sov. Phys. Solid State **16**, 639 (1974)].
20. V. N. Glazkov, R. M. Eremina, A. I. Smirnov, *et al.*, Zh. Éksp. Teor. Fiz. **120**, 164 (2001) [JETP **93**, 143 (2001)].

21. P. W. Anderson, J. Phys. Soc. Jpn. **9**, 316 (1954).
22. M. Hagiwara, K. Katsumata, I. Affleck, *et al.*, Phys. Rev. Lett. **65**, 3181 (1990).
23. T. Kennedy, J. Phys.: Condens. Matter **2**, 5737 (1990).
24. S. A. Altshuler and B. M. Kozyrev, *Electron Paramagnetic Resonance in Compounds of Transition Elements* (Nauka, Moscow, 1972; Halsted, New York, 1975).
25. A. I. Smirnov, V. N. Glazkov, H.-A. Krug von Nidda, *et al.*, Phys. Rev. B **65**, 174422 (2002).
26. A. Zheludev, T. Masuda, I. Tsukada, *et al.*, Phys. Rev. B **62**, 8921 (2000).
27. V. N. Glazkov, A. I. Smirnov, K. Uchinokura, and T. Masuda, Phys. Rev. B **65**, 144427 (2002).
28. V. K. S. Shante and S. Kirkpatrick, Adv. Phys. **20**, 325 (1971).
29. C. Yasuda, S. Todo, M. Matsumoto, and H. Takayama, Phys. Rev. B **64**, 092405 (2001).
30. M. V. Mostovoy and D. I. Khomsky, Solid State Commun. **113**, 159 (2000).
31. S. Grenier, A. Toader, J. E. Lorenzo, *et al.*, Phys. Rev. B **65**, 180101(R) (2002).
32. A. I. Smirnov, S. S. Sosin, R. Calemczuk, *et al.*, Phys. Rev. B **63**, 014412 (2001).
33. J. Bonner and M. Fisher, Phys. Rev. A **135**, 640 (1964).

Translated by R. Tyapaev